2009

Hydrogen Storage and Electronic Characterization of Magnesium-Based Intermetallics: Exploratory Flux Synthesis for Advanced Materials

Jeffrey B. (Jeffrey Brian) Whalen

FLORIDA STATE UNIVERSITY

COLLEGE OF ARTS AND SCIENCES

HYDROGEN STORAGE AND ELECTRONIC CHARACTERIZATION OF MAGNESIUM-BASED INTERMETALLICS: EXPLORATORY FLUX SYNTHESIS FOR ADVANCED MATERIALS

By

JEFFREY B. WHALEN

A Dissertation submitted to the
Department of Chemistry and Biochemistry
in partial fulfillment of the
requirements for the degree of
Doctor of Philosophy

Degree Awarded:
Summer Semester, 2009

The members of the committee approve the dissertation of Jeffrey B. Whalen defended on June 30, 2009.

_____
Susan E. Latturner
Professor Directing Dissertation

_____
Anjaneyulu Krothapalli
Outside Committee Member

_____
Albert E. Stiegman
Committee Member

_____
Oliver Steinbock
Committee Member

Approved:

_____
Joseph B. Schlenoff, Chair, Department of Chemistry and Biochemistry

The Graduate School has verified and approved the above-named committee members.

TABLE OF CONTENTS

LIST OF TABLES

LIST OF FIGURES

Chapter 1

Chapter 2

Chapter 4

Chapter 5

Chapter 6

ABSTRACT

The impetus of this research was the synthesis and characterization of new Mg-based hydrogen storage materials. Synthetic methods included metal fluxes, distillations and traditional stoichiometric melts. Pure Mg or Mg-X (X=element other than Mg) eutectic fluxes were useful in synthesizing intermetallic single crystals. Distillations of Mg containing materials were used to modify the structure and properties of a material and to grow large dendrites of nearly pure Mg crystals. Synthesized materials were characterized by X-ray diffraction, electron microscopy and thermogravimetric methods. Analyses for magnetic, transport and hydrogen storage properties were conducted.

To address the need for a method of screening newly synthesized products for hydrogen storage properties, a Sievert's-type volumetric system was built to activate and hydrogenate samples. The computer controlled system can hydrogenate samples at 0-2500 PSIG and 25-700 °C while collecting temperature and pressure data at 0.5 second intervals. Automatic absorption and desorption programs were also designed in LabView to allow for volumetric measurements. Samples activated and hydrogenated in the system could also be analyzed for subsequent desorption in a TGA.

Stoichiometric melts of Mg-Ca-Si led to the formation of composites containing the controversial phase, Ca_2Mg_3Si; these were analyzed for phase composition and dehydrogenation properties. Exploration of transition metal doping led to composites of $Ca_2Mg_3Si/Mg_2Si/CaMgSi$, Ca_2Mg_3Si/Mg_2Co and Ca_2Mg_3Si/Fe_3Si with reversible hydrogen storage capacities up to 4 weight percent. Slight doping of Si on the Mg site in a Mg_2Ca matrix produced a single phase material, $Ca_2Mg_{4-x}Si_x$ (x = ~0.3), which displayed a maximum hydrogen capacity of 1.9 weight percent.

A second phase in the Mg-Ca-Si system, CaMgSi, was synthesized in the form of large single crystals from a molten Mg-Al flux mixture. CaMgSi undergoes an electronic phase transition from metallic to semiconductor at 50 K. This metal to insulator transition was evident from both resistivity and magnetic susceptibility data. It is accompanied by a structural phase transition observable by low temperature powder X-ray diffraction. The hydrogen storage capacity of CaMgSi was expectedly negligible.

Additional reactions in the Mg-Al eutectic flux indicate it is a useful tool for exploratory synthesis of Mg-based or Al-based materials. Rare earth metals readily dissolve and react to form complex silicide phases such as $Eu_8Mg_{18}Si_{13}$ and $Yb_6Mg_{11}Fe_2Si_5$. Mixed fluxes of Mg-Al-X (X = Ga, In, Sn) improved the reactivity of the flux and created optimal crystal growth conditions for the compounds CaMgSi, CaMgGe and CaMgSn. The mixed fluxes also improve the solubility and reactivity of the lightweight elements Li, B, C and Si; these are desirable elements for incorporation into potential hydrogen storage materials. Further reactions have been conducted and stockpiled to create an organized crystal bank which can be extensively characterized in future work.

CHAPTER 1

INTRODUCTION

Research Directives

Mg-based intermetallics were synthesized and characterized for structure, magnetic, transport and hydrogen storage properties. Products were synthesized primarily by means of metal flux mixtures. Flux techniques were used in conjunction with other methods such as distillations and traditional stoichiometric solid state synthesis. The use of multiple synthetic methods was conducive to discovery of new materials by providing alternative routes toward target compounds, while avoiding products resulting from thermodynamically favored phases. During exploratory synthesis experiments, efforts were directed towards incorporation of Mg into the final products which resulted in the production of new hydrogen storage and electronic transport materials. A lab-built gas controlling and measurement system was developed for assessment of hydrogen storage capacities of the newly synthesized materials. Several new materials with interesting electronic properties were synthesized using a Mg-Al flux, which proved extremely effective at creating large, high quality crystals of intermetallics and Zintl phases containing Mg and/or Al. Reactions targeting electronic transport materials had an expanded element palette that included heavier elements and lanthanides. These reactants were not best suited for hydrogen storage, but capable of introducing desirable electronic effects to the products. The goal of this work was to yield new materials that contribute to the development of the hydrogen economy as a viable source of alternative energy.

Hydrogen Storage

The use of hydrogen as an energy carrier can resolve the pressing issues surrounding the near exclusive use of fossil fuels in the modern world. Advancements in energy technology and policy for a hydrogen economy in the U.S. will have global repercussions. In order to make a hydrogen economy favorable, a safe way to store it must be found. Possible methods for hydrogen storage include intermetallics and alloys, complex metal hydrides, metal-organic frameworks (MOF's), carbon nanotubes, liquefied cryogenic containers and pressurized gas cylinders.[1-4] Each method of storage has specific operational requirements and relies on different materials. Among these materials which can be used for hydrogen storage, solid state storage offers unique benefits to the overall energy storage efficiencies of fully integrated hydrogen power systems.

Pressurized gaseous hydrogen has poor volumetric capacity and, for transportation based applications, requires storage containers that are too large (occupy large internal vehicle volume) for most applications. Also, pressurized hydrogen poses explosion hazards which limit public acceptance and feasible, safe commercialization. Despite these drawbacks, hydrogen cylinders are the most common form of stored hydrogen and are currently in use in many hydrogen power applications. Liquefying hydrogen (1 atm H_2 gas liquifies at 20.28 K)[5] is very cost prohibitive, consuming more energy than can be harvested.

The use of graphitic carbon for hydrogen storage has been hindered due to inconsistent results and the limited interactions of hydrogen with the graphene matrix.[6-9] In these systems, hydrogen can only be physisorbed to the surface which can limit the maximum hydrogen capacity compared to other solid materials that can chemisorb hydrogen (3 dimensional saturation of hydrogen in the bulk solid). It is worth noting the immensely large surface areas created by certain nanostructured graphene could increase these materials' total physisorptive capacity. MOF materials are currently intensely researched for hydrogen storage applications. These materials have the ability to physisorb significant amounts of hydrogen due to massive surface areas created by the extremely high porosity of the materials and reactive metal centers which catalyze hydrogen surface adsorption.[10,11]

Complex metal hydride materials are able to obtain high theoretical gravimetric storage capacities due to the lightweight of the constituent elements of the material (usually containing one or more of elements Li, B, N, Na, and Al). The corrosive or reducing nature of the common slurry solutions created to solvate and stabilize complex metal hydrides has unique challenges when implemented into a power generation systems.[12] Despite the high weight percent of hydrogen in molecular hydrides such as CH_4 (25.2 wt% hydrogen), chemically bonded hydrogen is nearly impossible to extract from these molecules without combustion and decomposition to H_2O and CO_2, which bypasses the creation of H_2 completely.

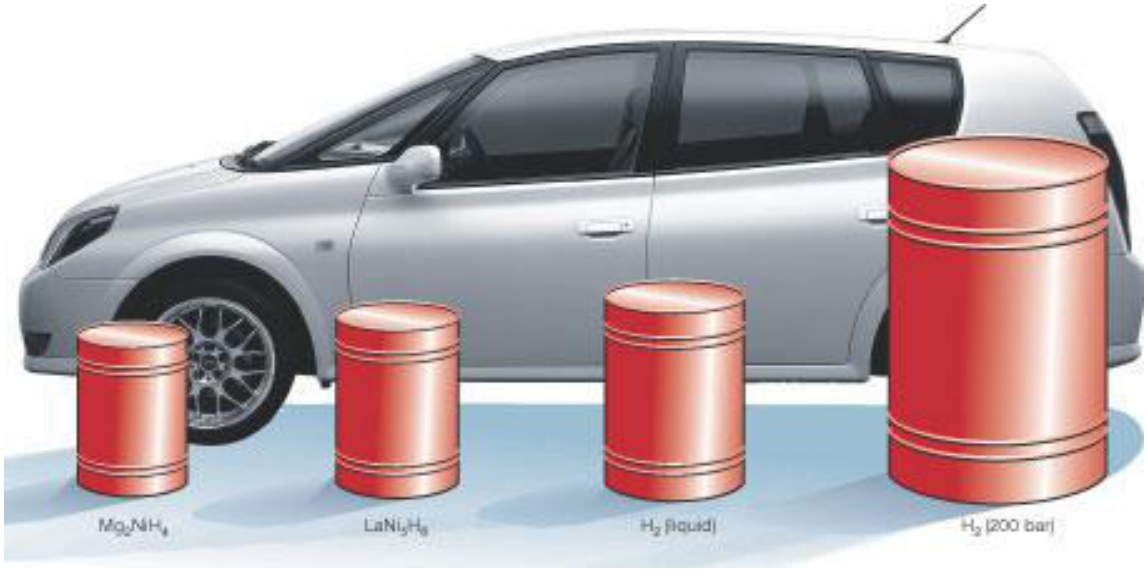

Figure 1.1 Volumetric comparison of several current methods of storing 5 kg of hydrogen, an amount suitable for use in a personal vehicle.[13]

Storing hydrogen as a gas can only be accomplished in accordance with kinetic molecular theory which governs the minimum distance that can be established between individual gas molecules at a given temperature and pressure.[14] Compression of gaseous hydrogen is opposed by repulsion resulting from collisions of high kinetic energy molecules with each other and the walls of the container. When hydrogen is stored within a host material, the laws governing the minimum distances between hydrogen molecules will be related to the hydrogen-host material interactions instead of kinetic molecular theory of gases. The ability of some solid materials to

allow hydrogen densities higher than that of liquid hydrogen is an example of this effect (see Figure 1.1). For instance, 1 mol of H_2 in $LaNi_5H_6$ (57.044 mol H_2/L) occupies 0.01753 L; 1 mol of liquid H_2 (35.213 mol H_2/L) has a volume of 0.02840 L.[5]

Solid state intermetallics and alloys, on the other hand, have relatively high volumetric and gravimetric capacities while controllably maintaining the flow of hydrogen bound within in an inert host matrix. These materials are often in the form of powders, which eliminate the corrosive effects of solvated elements like Li and Mg. Preferred intermetallic hydrides are composed of elements with low cost and mass that can be reversibly cycled in extended hydrogen absorption-desorption lifetimes. The most desirable solid state hydrogen storage materials can desorb within a delivery pressure range of 0-200 PSIG using a comparable amount of heat to that which is created as waste by a PEM fuel cell (working temperatures of ~102 °C) to drive the endothermic dehydrogenation of the host matrix.[12] A material that could perform within these parameters would be potentially applicable to hydrogen storage systems in fuel cell or internal combustion power generation systems.

The common ways of reporting hydrogen storage capacity is by the gravimetric or volumetric efficiency. The difference between these two efficiencies is the way in which they are calculated; gravimetric capacity refers to ratio of the mass of hydrogen stored to the mass of the host material, while volumetric capacity is the ratio of the volume of hydrogen stored to the volume of the host material. If the gravimetric capacity is high, the mass of hydrogen stored in the material is large relative to the mass of the host material, but this does not take into account the volume that the host material will take up. Likewise, a large volumetric capacity does not indicate how heavy the material is. For instance, the gravimetric capacities of intermetallic hydrides are the limiting factor because these materials are usually small, occupying little 3D space, so volumetric capacity is usually not reported. Conversely, for complex metal hydrides the gravimetric capacities are much larger (the materials are lightweight) than the volumetric capacities because these materials are liquids and the solvents that dissolve the metal hydrides require large volumes relative to the amount of metal hydride dissolved. In the case of complex metal hydrides, the volumetric capacity the main consideration since it is usually much lower than the gravimetric capacity. For any hydrogen storage material, volumetric and gravimetric capacities can be calculated and both should be considered when the material is applied into a system.

Interactions of Hydrogen with Intermetallics and Alloys

The unique interaction of hydrogen gas with intermetallics has several mechanistic aspects to consider. Firstly, when gaseous hydrogen molecules come in contact with the reactive surface area of the solid, the hydrogen molecules are bound to the surface of the material. Catalytic interaction between the metal atoms on the surface of the intermetallic and the H_2 molecules results in breaking of the covalent H-H bonds to produce two H atoms with a weak metallic bond to the surface of the solid material. This process effectively creates a propagating surface layer of hydrogen that spreads out away from the first nucleation site. Once the surface layer has been formed, the H atoms are incorporated into the actual solid through solid state diffusion. This diffusion of hydrogen into the metal lattice is the rate limiting step and is referred to as chemisorption-absorption of a gas into the solid in three dimensions, similar to the absorption of water by a dry sponge. The kinetics and thermodynamics of this step define the critical transitional properties of the material and are determined by the composition and structure of the intermetallic. Finally, the H atoms will occupy minimal energy positions within the metal lattice thus forming the stable intermetallic hydride phase. This hydride phase can be either structural or interstitial depending on the location of hydrogen in the structure and diagrams of both cases are shown in Figure 1.2. For structural hydrides, the H atoms form metal-hydrogen bonds and occupy a crystallographic site, which usually results in a different structure for the hydride phase than that of the non-hydride phase. In the case of interstitial hydrides, the H atoms reside in the free space holes between the normal atomic crystallographic sites and a resulting expansion of the unit cell parameters can be observed.

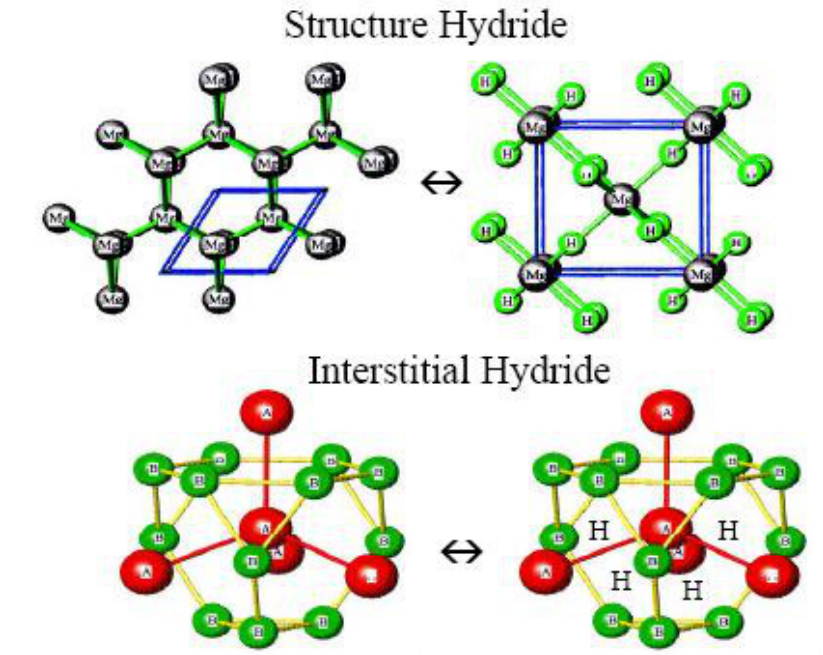

Figure 1.2 Diagrams of structural and interstitial hydrides.[15]

An understanding of the energetically favorable sites in the lattice for hydrogen occupation can aid in designing intermetallics likely to absorb hydrogen. All metal elements can be classified as either "A" type, which form a stable hydride phase(s) or as "B" type, which do not form a stable hydride phase. The ratio of A/B elements in an intermetallic will dictate the nature of absorption and desorption for that material. A high A/B ratio will result in materials that hydrogenate very easily, but retain the hydrogen with strong binding forces which necessitate very high temperatures for full desorption and can lead to disproportionation reactions upon cycling. The high ratio of A element in the structure will cause the hydride phase of A to be formed upon hydrogenation; upon dehydrogenation, the stoichiometric amounts of elemental A (and B) will be re-created but the intermetallic structure of the original material is completely lost. A low A/B ratio material will have negligible hydrogen absorption at reasonable temperatures and pressures; due to the low concentration of A atoms, the attractive forces are weak or non-existent. Figure 1.3 shows three possible tetrahedral arrangements of A and B atoms with the most desirable arrangement having two corners occupied by A atoms and other two corners occupied by B atoms. This allows hydrogen to reside in a location that keeps it in contact with an A and B atom simultaneously. This dual contact results in reversible

hydrogen storage at moderate temperatures and pressures. Also shown in Figure 1.3d is a diagram showing compositional A/B ratio vs. bond order ratio and the narrow band associated with a balance of these ratios that results in materials which can reversibly store hydrogen. The bond order ratio was calculated from literature values of enthalpies of certain binary compounds and applied in the displayed equation to the intermetallics in the diagram.

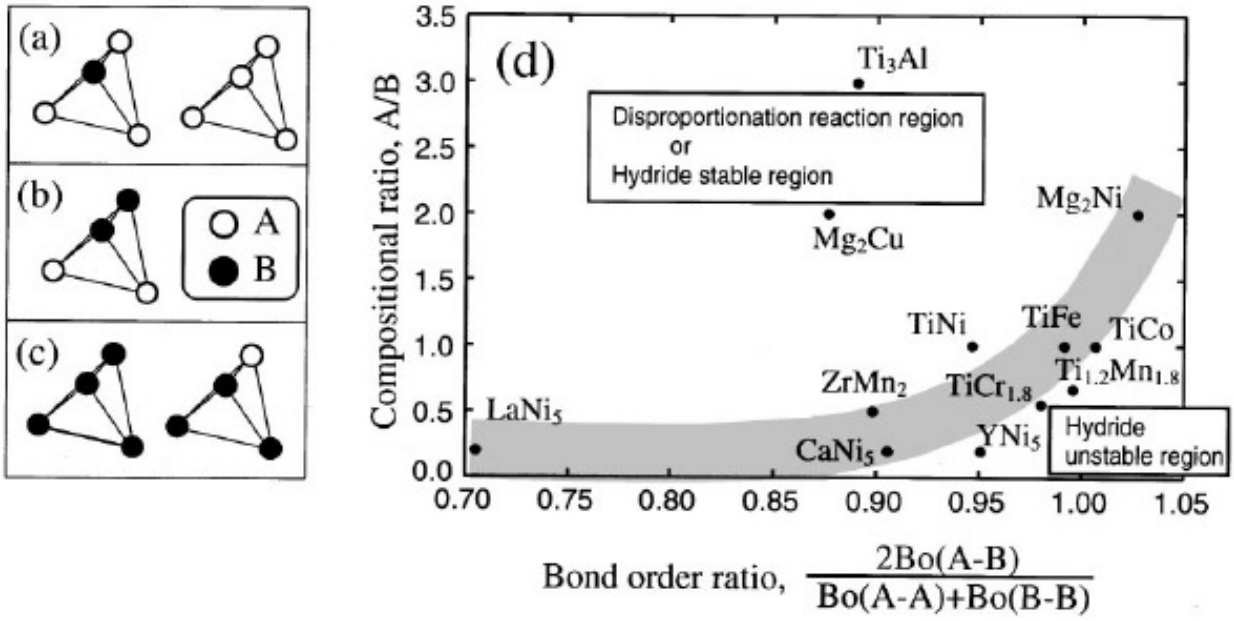

Figure 1.3 Three types of tetrahedral coordination environments to host interstitial hydrogen atoms having ratios of: (a) high A/B, (b) moderate A/B (most favorable), and (c) low A/B. Also shown in (d) is the relationship of compositional ratio to bond order ratio for several current intermetallic hydrogen storage materials.[16]

Current Hydrogen Storage Intermetallics

The current state of the art materials for solid state hydrogen storage include $LaNi_5$, TiFe and Mg_2Ni (see Figure 1.4). Many other compounds exist that absorb an appreciable amount of hydrogen, but none have come to the forefront of application like the previously mentioned compounds. Most solid state hydrogen storage materials can be classified into one of the following groups based on composition and designation of the "A" and "B" elements in the compounds: A_2B, AB, A_6B_{23}, A_2B_7, AB_3, AB_2, AB_5. Due to the different compositions and

structures of these materials, they have different kinetics and critical operating temperatures and pressures.

The use of the AB_5 phase, $LaNi_5$, has been widespread, but this material is both heavy and expensive when compared to other competitive non-La hydrogen storage materials. $LaNi_5$ can be 90-95% reversibly hydrogenated to $LaNi_5H_6$ at about 25 °C and 2 atm in just minutes. The mass of hydrogen stored in $LaNi_5H_6$ is 40% higher per unit volume than liquid hydrogen.[17] $LaNi_5$ has hexagonal $CaCu_5$ structure type (*P6/mmm* (#191), a = 5.0228 Å and c = 3.9826 Å) The glaring issues inhibiting the full scale global use of $LaNi_5$ to store hydrogen is the expense of the elements in the material, especially La, and the low gravimetric hydrogen capacity of this compound (1.8 weight percent). Several other alloys have been developed that have cheaper and lighter elements, but inherently, have other drawbacks.

The AB phase, TiFe, offers interesting capabilities as a hydrogen storage material because the elements in the material are abundant, lightweight and inexpensive. In addition, TiFe has a hydrogen capacity comparable to that of $LaNi_5$ (1.8 weight percent). The drawbacks to TiFe are mainly due to difficult activation of the material and susceptibility to O_2, H_2O and CO surface poisoning. Activation of TiFe requires increasing of the reactive surface area by grinding or milling to produce a fine or ultrafine (microscale or nanoscale, respectively) powder.[18,19] TiFe has the CsCl cubic structure type (*Pm-3m* (#221), a = 2.9789 Å) and several methods of preparation include mechanochemical reactions, deposition and stoichiometric high temperature melting. Energy efficient routes towards the production of materials like TiFe, that are comprised of high melting point elements and have a very stable lattice, will increase the viability for large scale implementation. As with $LaNi_5$, TiFe fails to reach a high enough gravimetric hydrogen capacity to feasibly be integrated into hydrogen power systems such as fuel cell vehicles.

Lastly, the third common solid state material used for hydrogen storage is Mg_2Ni. The high hydrogen capacity of its hydride, Mg_2NiH_4 (3.6 weight percent), has inspired great interest in this, and similar compounds, as hydrogen storage materials. Mg_2Ni has several different structures it can adopt, with the most common having the hexagonal C36 Laves phase, which classifies as an AB_2 type material (*P6$_3$/mmc* (#194), $a = b$ = 4.824 Å, c = 15.826 Å) . This material has different characteristics than $LaNi_5$ and TiFe due to the formation of $[NiH4]^{2-}$ anionic units in the hydride phase. When Mg_2Ni is converted to the hydride phase, covalent

character is exhibited between Mg^{2+} ions and $[NiH_4]^{4-}$ polyhedrons and this leads to a very strong affinity of the lattice for hydrogen. Resulting effects of this affinity are the exothermic nature of hydrogenation from Mg_2Ni to Mg_2NiH_4 (-32.3 kJ/mol H) and high desorption temperatures (520-570 K). In order to perform as a hydrogen storage material, Mg_2Ni must be formed into a powder as a bulk crystalline sample does not absorb hydrogen even up to 623 K. This alludes to the fact that the rate limiting step of the hydrogenation process is the diffusion of hydrogen into the lattice. By forming a powder, the distance hydrogen atoms must migrate through a lattice is minimized and the number of available sites for surface hydrogen molecule dissociation is maximized.[20-22]

There have been extensive studies on the effects of doping and substitution in hydrogen storage alloys. Although these techniques are effective for fine-tuning of hydrogen storage properties, they usually do not result in significant changes in the behavior of the material when it interacts with H_2 gas. For example, variation of both the electropositive and electronegative atoms has been explored for $LaNi_5$, yet the maximum hydrogen capacity has never been improved to above 3 weight percent. As with $LaNi_5$, TiFe has been studied as a pure material and in a variety of mixed states with other materials. More drastic advances come from the creation of entirely new materials: exploratory synthesis is a necessity in this field. As with any solid state hydrogen storage material, the key factors in the performance of new materials are activation temperature, equilibrium hydrogen delivery pressure, reversibility and maximum hydrogen capacity.

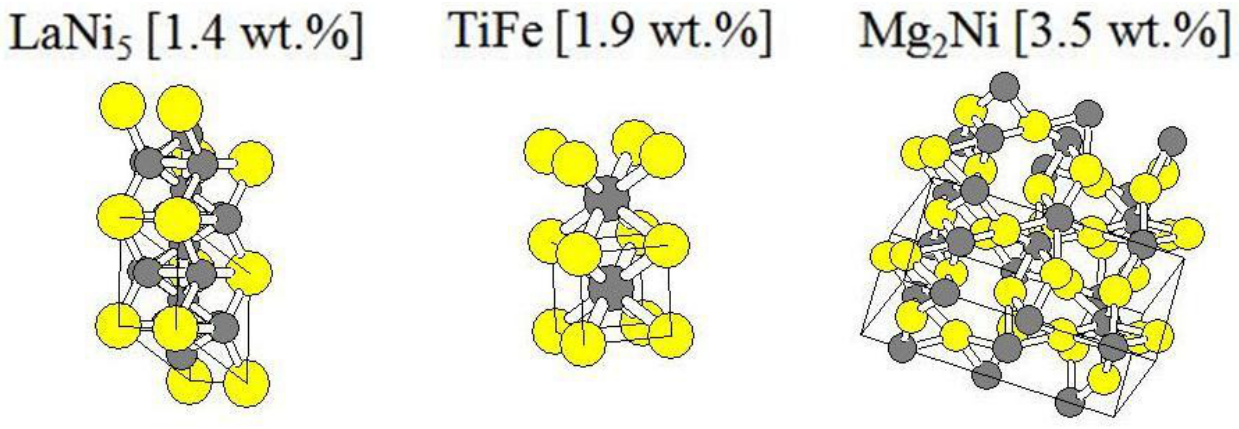

Figure 1.4 Structures and hydrogen storage capacities of common state of the art materials.[70,74]

Challenges and Goals

Despite the excitement surrounding hydrogen technologies, several critical challenges remain to be addressed before hydrogen systems can be commercialized. Hydrogen production by photocatalyzed electrolysis of water, higher efficiency photovoltaic cells, fuel cell optimization and high density hydrogen storage represent the main obstacles to implementation of a hydrogen economy. Among these obstacles, hydrogen storage is the most pivotal area of development and improvements in this field would create feasible solutions to the ominous energy crisis. The success of a hydrogen economy is dependant on the role of new hydrogen storage materials yet to be discovered. The US Department of Energy has set forth several goals for the development of hydrogen storage systems, shown in Figure 1.5. Notable among them are the desired gravimetric capacities of 6 weight percent hydrogen achieved in a fully integrated storage system by the year 2010 and 9 wt. % by 2015. It is important to note that this gravimetric goal is for an entire system, including the container, and not just the hydrogen storage material itself. The DOE goals also define system costs and refueling times as important factors in a feasible hydrogen storage system. The goals are defined for 5 kg of stored hydrogen because this would provide about as much energy as a full tank of gas in a normal personal vehicle, based on current PEM fuel cell efficiencies.

The US DOE goals provide guidance for research and development, but depend on scientific breakthroughs to become reality. Exploratory synthesis in hydrogen storage can lead to materials that will satisfy the DOE goals without the drawbacks of current state of the art materials. New solid state synthesis methods that can provide routes to materials that can not be produced by any other methods are crucial in the discovery of new hydrogen storage materials. Flux synthesis has great benefits as an exploratory tool because of the unique crystal growth environments that can be created and thus produce metastable and non-thermodynamically favored phases.

Storage Parameter	2005	2010	2015
Gravimetric Capacity (Specific energy)	1.5 kWh/kg 0.045 kg H_2/kg	2.0 kWh/kg 0.060 kg H_2/kg	3.0 kWh/kg 0.090 kg H_2/kg
System Weight:	***111 Kg***	***83 Kg***	***55.6 Kg***
Volumetric Capacity (Energy density)	1.2 kWh/L 0.036 kg H_2/L	1.5 kWh/L 0.045 kg H_2/L	2.7 kWh/L 0.081 kg H_2/L
System Volume:	***139 L***	***111 L***	***62 L***
Storage system cost	$6 /kWh	$4 /kWh	$2 /kWh
System Cost:	***$1000***	***$666***	***$333***
Refueling rate	.5 Kg H_2/min	1.5 Kg H_2/min	2.0 Kg H_2/min
Refueling Time:	***10 min***	***3.3 min***	***2.5 min***

Targets assume a 5-kg H2 storage system

Figure 1.5 The US DOE goals for 2010 and 2015 based on weight, volume, cost and refueling time.[24]

Flux Growth of Intermetallics

The use of a molten metal solvent (flux) can alleviate issues with traditional solid state synthesis and produce single crystals that would not form without the solvation and environment created in the flux during heating. Solid state materials conventionally require high temperatures (≥1000 °C) for synthesis and chemical modification in order to create enough atomic diffusion to drive a reaction. Traditionally, elements are ground together, pressed and heated, then this process is repeated to purify and isolate the desired phase. This type of synthesis methodology is thermodynamically limited and energetically costly (electrical power and materials costs) and additionally, most phases are produced in the form of powders, which limits the characterization of structural properties or anisotropic transport and magnetic effects. For most characterization methods, single crystal samples are more easily analyzed. Incongruent melting, high vapor pressures or high melting temperatures can inhibit the growth of pure phases from traditional melts, even if the proper ratio of elements was supplied for a target phase. This type of high

temperature synthesis favors thermodynamic sinks in the form of very stable phases which will form within a melt, leaving excess reactants to form secondary phases or remain un-reacted in the melt. This creates multi-phase products and, in certain cases, the isolation of one phase from a mixture of phases can be impossible. By employing the molten metal flux methodology, new intermetallic phases can be grown and isolated for further characterization without encountering many of the difficulties associated with traditional solid state synthesis.

Technique

In order to conduct metal flux synthesis, a reaction must contain an excess of flux element(s) which act as a solvent for the reactants. Above the melting point of the flux, a metal liquid pool is created which solvates and transports the other reactants present within the melt. At this point, nucleation and crystallization of phases can occur within the molten pool. Once the crystals have formed, the flux must be removed. This can be carried out using a variety of methods; the most common forms of flux removal are by etching or mechanical removal (inversion of reaction vessel followed by centrifugation). The vessel used to contain the flux reaction consists of a crucible (made of appropriate material for the reaction being considered, see Table 1.1) inside a vacuum sealed quartz ampoule. In some cases a filter is necessary, but for most reactions the product crystals remain stuck to the crucible walls during centrifugation. Figure 1.6 shows a common set-up for Mg-based flux reactions and Table 1.1 lists some common crucible materials that can be used for different types of fluxes.

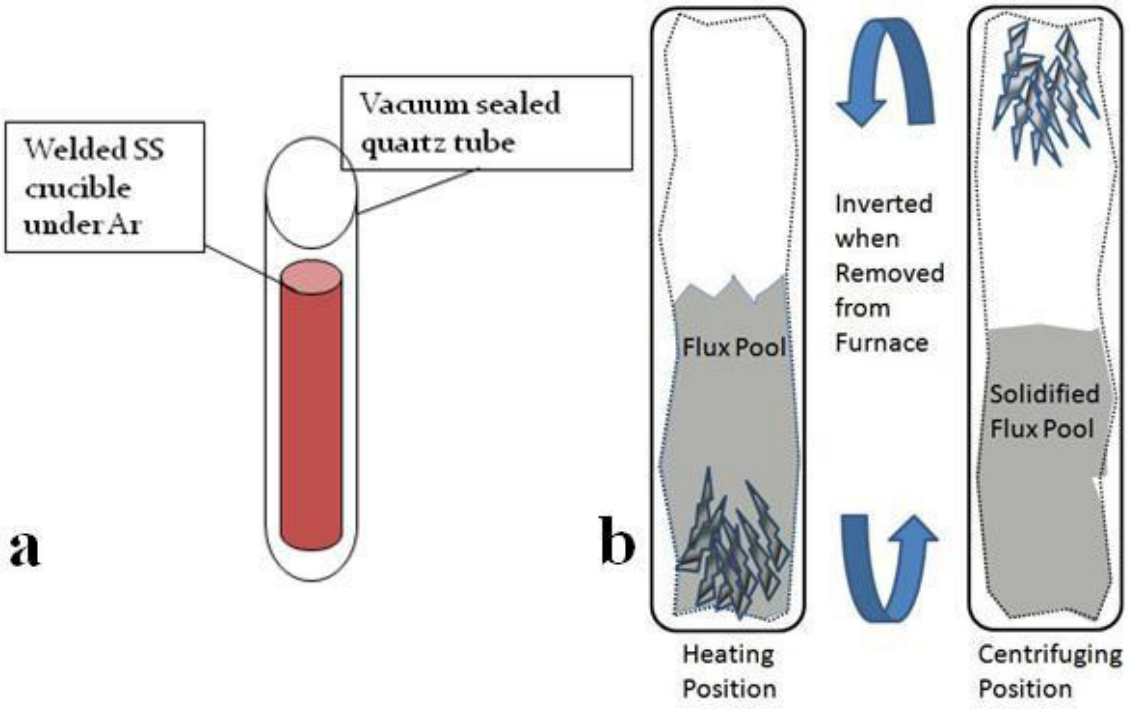

Figure 1.6 Diagram of a reaction vessel (a) (consisting of welded stainless steel, or niobium crucible inside a vacuum sealed quartz ampoule) and the inversion-centrifugation process which separates the flux from the crystals stuck to the crucible walls (b).

Table 1.1 Acceptable crucible materials for different types of flux reactions.[25]

Metal	Container
alkali metals	Ta, steel
alkaline earth metals	Ta, graphite for Ba, steel
Al, Ga	Al_2O_3, MgO, BeO
Mg	MgO, Ta, graphite or steel
Mu	Al_2O_3
Cu, Ag, Au	graphite, MgO, Al_2O_3, Ta
Fe, Co, Ni	Al_2O_3, ZrO_2, ThO_2
Zn, Cd, Hg	Al_2O_3
In	Al_2O_3, Ta
rare earths	Ta, Mo, W, BeO
Bi, Sn	Al_2O_3, SiO_2, graphite
Sb	SiO_2, graphite

Flux Methodologies

Flux crystal growth is a solvent-assisted chemical reaction in which the flux is the solvent and the added reactants are the solutes. In many cases, the phases formed by flux growth are impossible to synthesize by any other method. The flux method produces unique and dynamic crystal growth environments while also facilitating isolation of product crystals from the excess flux. Both solubility and diffusion play crucial roles in determining the outcome of reactions. Fluxes must be tailored to dissolve the reactants and must not form simple binary phases near the centrifugation temperature. Many experimental factors can be varied when using flux synthesis, but simplifying the reactions and using organized, systematic variations allow for better control of the reactions and less uncertainty about the crystal formation mechanisms. Fluxes can either be single or multi-component (eutectic mixtures) as well as reactive or unreactive (incorporated or not incorporated into the final products).

By using eutectic mixtures of elements, lower melting points can be obtained than for either of the constituent elements. This allows for the reaction of elements at temperatures which would normally not be accessible. Synthesis of intermetallics at reduced temperatures decreases thermal strain and defects in the final products. Another benefit of eutectic mixture fluxes is the dual solvent situation created by having two component elements, which enables tailoring of the reaction so that certain reactants will be dissolved by one component of the flux, while others will be dissolved by the other component. For instance, in a Mg / Al flux mixture, iron is insoluble in Mg, but will be dissolved in the Al flux component. Once it is thus brought into solution, it can react with elements dissolved by Mg. Also, flux components can be reactive or inert; it is possible to crystallize phases that contain all, some or none of the flux elements. The components may be required to create an appropriate reaction environment, but not necessarily incorporated into the product. This is a testament to the unique crystal growth environment created by employing flux methods. As an added benefit, in most cases, the products from flux reactions yield single crystals which can be reliably characterized by most solid state analysis methods.

Flux Choices and Examples of Flux Grown Intermetallics

For single component fluxes, choosing the flux is a simply a matter of desired centrifugation temperature, crucible material and reactant solubility. When considering possible multi-element eutectic fluxes for synthesis, it is important to consider what multinary compounds could be formed by the elements in the flux. Although previous works have explored the use of low-temperature melting fluxes like Ga, Al, In, Bi, Hg, Zn and Pb, much less effort has been directed toward higher melting point fluxes and mixed eutectic fluxes.[26-29] Eutectic mixtures that melt below 800 °C are well suited for flux synthesis, allowing mechanical separation of the flux by centrifugation after the reaction. Examples of some binary phase diagrams having useful eutectic regions are the Al-Mg and Ca-Mg systems shown in Figure 1.7 and Figure 1.8. In the Al-Mg diagram, the eutectic region actually spans a range of compositions and allows for flux mixtures that can vary from about 70 / 30 to 30 / 70 atomic percent Mg / Al while still melting at about 450 °C. The Mg-Al molten matrix is capable of accessing transport, diffusion, solubility and reactivity properties of both Mg and Al. For the Ca-Mg system, there exist two eutectic ratios at ratios of 10.5 / 89.5 and 73 / 27 atomic percent Mg / Ca which melt at 517 °C and 445 °C, respectively. The eutectic ratio will determine not only the melting point, but also the chemistry of the reaction and composition of the products. For example, of two eutectics found in the Mg-Ca phase diagram, one is Mg-rich while the other is Ca-rich. Choosing the Mg-rich eutectic will most likely lead to Mg-containing phases and the Ca-rich eutectic will lead to Ca-containing phases. If a eutectic is comprised of less than 10% of a second component, then it is best to consider it a pure flux of the first element with added reactants (second component). For example, a reaction of Fe / Ge / Mg at a mmol ratio of 0.5 / 0.115 / 8.85 should not be considered a Mg-Ge flux despite the eutectic located at 1.15%Ge / 98.95%Mg because the ratio of Mg is too large. Yet, a reaction of Fe / Ni / Mg at a mmol ratio of 0.5 / 1.13 / 8.87 can be considered a Mg-Ni flux reaction because the fraction of Ni in Mg is above 0.10 and a eutectic is located at 11.3%Ni / 88.7%Mg. The reason for this is the importance of having excess amounts of the flux in the reaction. Solubility and transport will be greatly hindered if there is not enough flux present to completely cover the reactants.

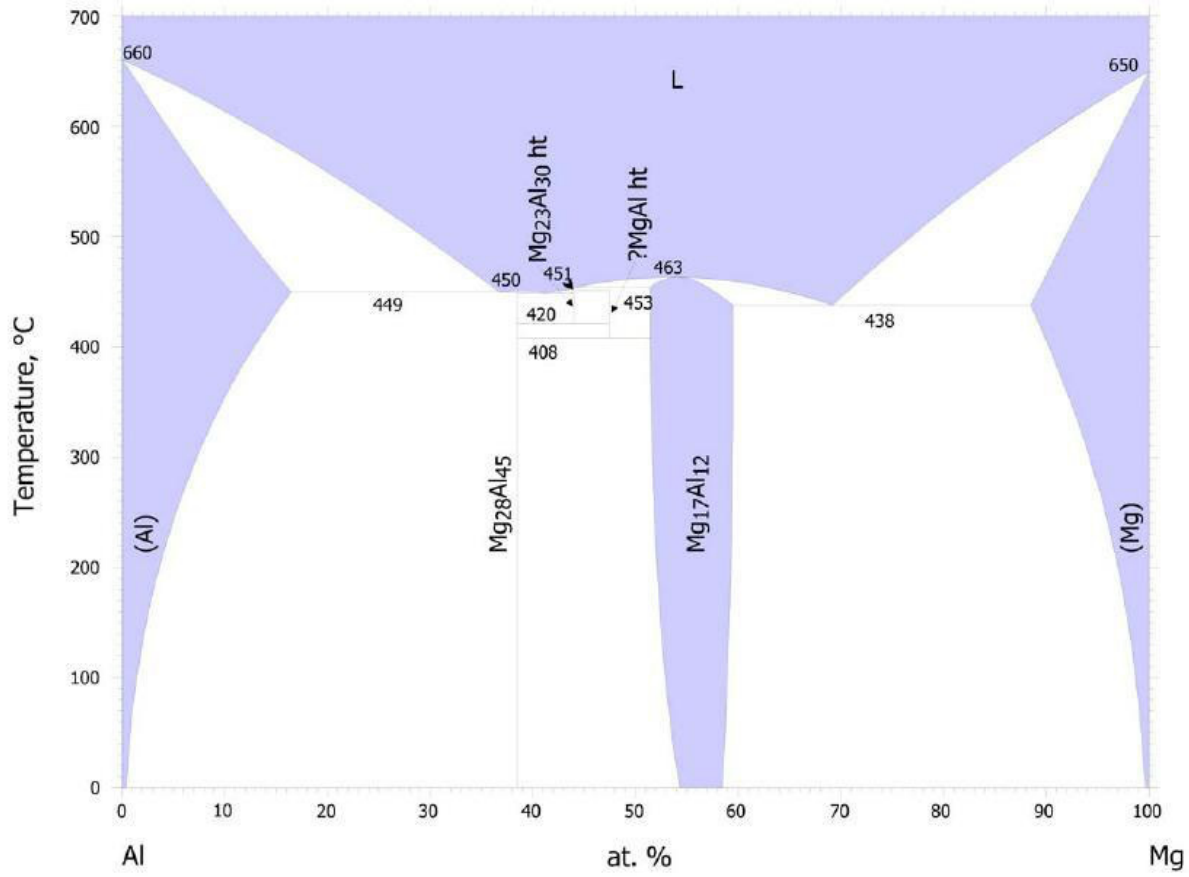

Figure 1.7 Binary phase diagram for the Al-Mg system.[30]

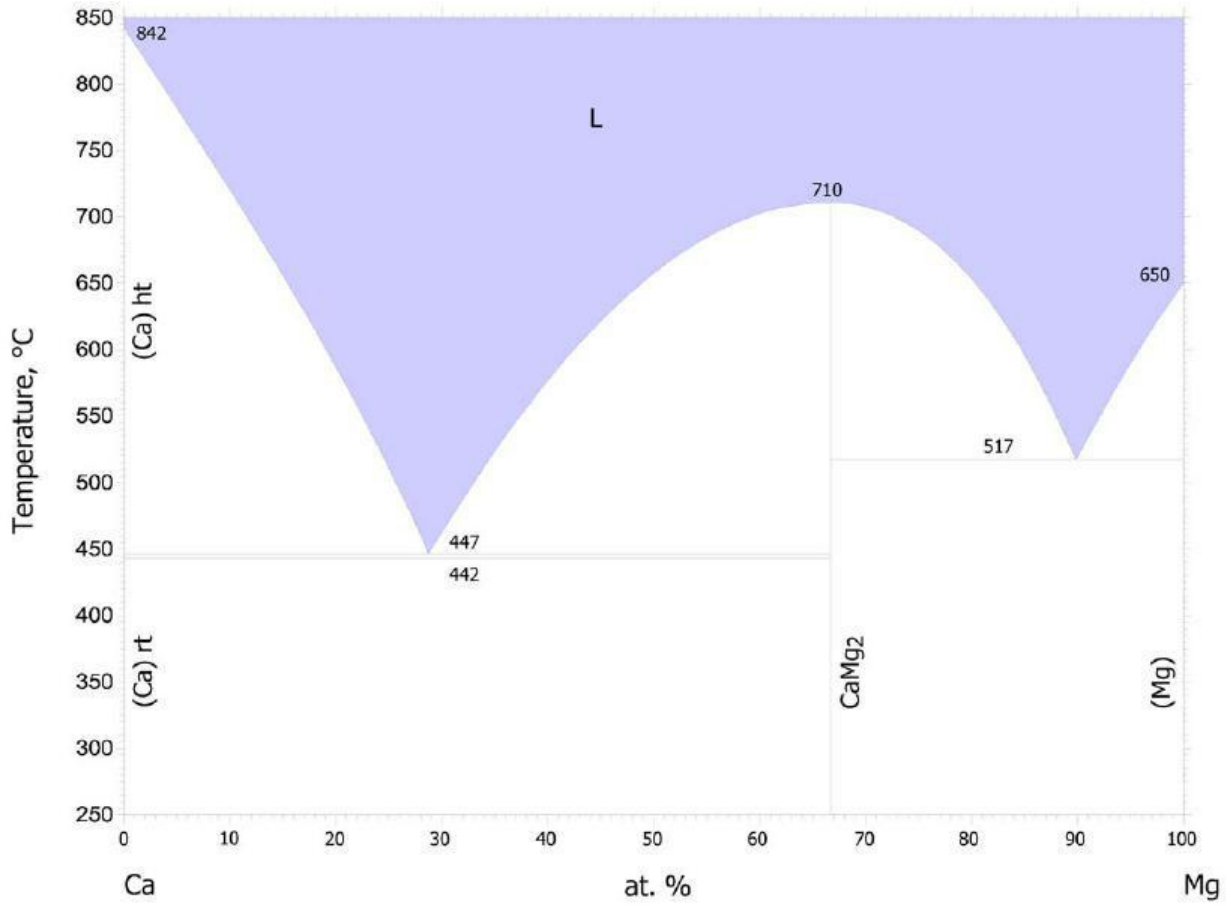

Figure 1.8 Binary phase diagram for the Ca-Mg system.[30]

Examples of flux grown single crystals can be found in current literature. The tin flux has proven useful for the synthesis of many binary, ternary and quaternary phosphide, boride and silicide phases including SiP, CrP_4, Re_3P_4, CoP_2, NiP_2, YB_{25}, $Er_8Si_{17}B_3$, V_3Si, Mn_5Si_3 and $ZnSiP_2$. Liquid Al and Ga flux have also been used to synthesize compounds such as V_2B_3, Lu_2AlB_6 and many rare earth containing phases.[26-29,31-40] As previously stated, the use of multi-component, high melting point fluxes is very limited despite the well established use of single component fluxes. Multi-component fluxes introduce experimental variables not present for single component fluxes and for this reason, it is plausible that new phases can be discovered and substitution control can be improved.

Materials Characterization Methods

Elemental Analysis

Characterization of hydrogen storage materials requires data about the crystal structure, elemental composition and physical/electronic/magnetic properties. Once new crystals have been synthesized, the elemental analysis technique serves to screen products to determine if they are worth further investigation, or if they are well-known thermodynamically favored binary phases. Scanning electron microscopy (SEM) involves the use of a high energy beam of electrons which can be directed at a sample which has been mounted on an Al puck using double sided carbon tape. The beam has several interactions with the sample which can occur including backscattered electrons (BSE), diffracted backscattered electrons, secondary electrons, and photons. The BSE's and secondary electrons are commonly used for visual representation (20X-30,000X magnification) of samples with details of morphology and contrasts between different phases. The secondary electrons are present due to the ejection of valence shell electrons from atoms in the sample.

The process of detecting elements in a sample begins with the beam of electrons from the SEM hitting the sample and ejecting core electrons from the atoms in the sample. The electrons in the higher energy levels fall down in energy to fill the voids created by the ejected core electrons. The electrons that fall down in energy give off emission of X-rays characteristic of the energy level spacing unique to each element. The resulting X-ray emissions are measured by hitting a liquid N_2 cooled detector that measures the radiation's energy. Figure 1.9 shows a generalized energy diagram that shows the electron excitation pathways (dotted arrows) to higher energy levels and the resulting emissions (solid arrows). K-alpha, K-beta, L-alpha and M-alpha energies represent the allowed transitions that change according to different atomic nuclei.[41,42]

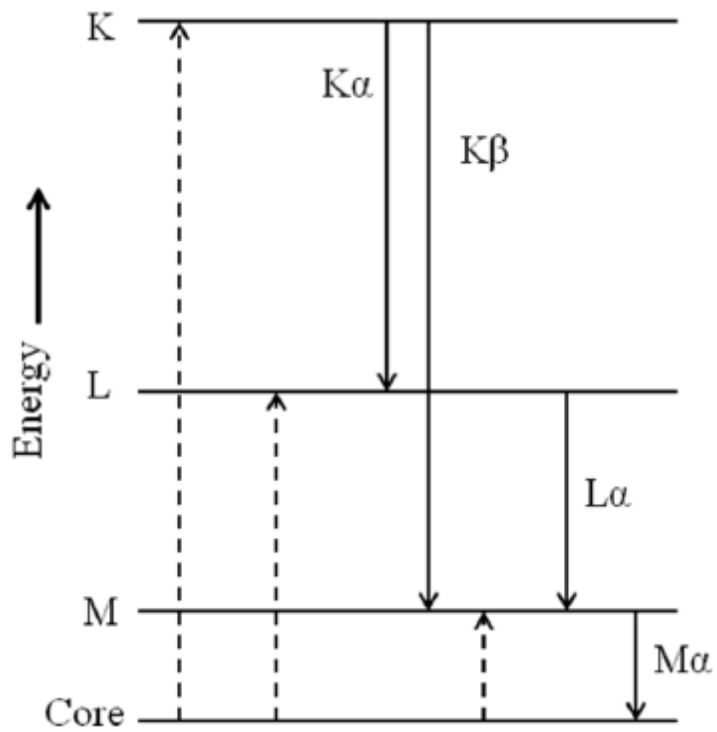

Figure 1.9 Energy level diagram showing electron transitions between energy levels. Dotted lines show excitation (absorption) while solid lines show relaxation (emission).[41,42]

SEM/EDS analysis was conducted on a JEOL 5900 SEM equipped with an energy dispersive spectrometer (EDS) detector. XRF software was used to analyze EDS data and collect spectra, analysis and images. Only semi-quantitative compositional data can be collected due to the inability of the EDS detector to observe photons from light elements ($Z \leq 11$), observe signals from trace or doped elements, and resolve energy levels well. However, SEM-EDS provides qualitative elemental ratios which can serve to identify known phases or be used in an X-ray structure solution, which enables more accurate determination of ratios.

Structural Determination

Two types of X-ray diffraction, single crystal (SCXRD) and powder (PXRD), were used to determine crystal structures of products. If products were synthesized in single crystal form from the flux method, single crystal X-ray diffraction was conducted; for powder or multi-phase products obtained from stoichiometric melts or ball milling, powder X-ray diffraction was used.

The benefit of SCXRD is high resolution data which allows for determination of accurate atomic positions, bond lengths, bond angles and environments. The effectiveness of this characterization method depends on the quality of the crystals being analyzed. Twinned crystals or multi-phase products can be impossible to analyze via SCXRD. PXRD is an effective means of confirming crystal structures determined by SCXRD and is still effective for determination of phase composition for multi-component products. When large single crystals were available, a small shard was broken from the center of a crystal for SCXRD analysis. Multi-phase products were hand ground in a small alumina mortar and pestle (if brittle enough) or ball milled to obtain uniform particle size in the powder prior to analysis by PXRD.

X-ray diffraction from a crystalline sample is described by Bragg's Law shown below.

$$n\lambda = 2d*\sin\theta;$$

where n = 1 for most cases (accounts for the repeating planes of the crystal lattice which will all diffract as multiples of a single reflection), λ = wavelength of the incidence X-rays (for instance, 1.5418 Å emitted by Cu), d = d-spacing (perpendicular distance between pairs of adjacent planes) and θ = Bragg angle (incidence angle of X-rays).[43,45] This equation relates the crystal lattice orientation with respect to the detector based on the perfect Bragg angle. For SCXRD, the repeating lattice planes in a crystal structure multiply the intensity and diffract X-rays toward a point location, a "spot", where the detector can be positioned to measure the spot location, intensity and shape. By moving the detector and rotating the crystal to vary the angles, a full 3D sphere can be collected for a crystal to record all reflections. Spots are integrated then indexed and then algorithmically fit to the expected set of reflections, which is specific for each space group. The SCXRD software outputs unit cell parameters and space group symmetry which is then combined with the EDS data to determine the unit cell stoichiometry. Refinements of the structure or corrections for twinning can then be applied with several programs such as Cell_Now, Structure Tidy and Platon.

In the case of PXRD, the powder products are randomly oriented on the sample holder and are simultaneously representing all of the Bragg angles as a set of discrete intensities. The powder is pressed into a flat surface on a non-diffracting sample holder (usually plastic wafer) so the detector can scan the angle range and record locations of high reflection intensities as peaks. For a particular structure, the angles that fulfill the Bragg angle will have a greater population of reflections which results in a "halo" on the detector. The halo locations are related to the phi

angle of the detector and the output from the PXRD shows peak location, intensities and shape as part of a XRD pattern.

In this work, two somewhat unusual X-ray diffraction techniques were used: powder diffraction on a SCXRD and low temperature traditional powder diffraction (down to10 K). The use of the single crystal diffractometer as a powder diffractometer has the benefits of very small sample amounts, protection from ambient air and quick collection times (full powder patterns in about 9 minutes). In order to operate the SCXRD to collect powder data, samples are ground to a powder then combined with paratone oil to make a slurry. This slurry can then be loaded into a cryo-loop and put on the goniometer head of the diffractometer under flowing nitrogen which freezes the paratone oil and immobilizes the slurry. The sample is then run on the diffractometer using a custom designed procedure that orients the detector to sweep the phi angles from the sample in the exact same manner as a standard PXRD. The only drawback to using the SCXRD for powder diffraction is the Mo K-alpha X-ray source used by the SCXRD which causes the location of the peaks in a pattern to be shifted toward lower 2-theta values. For certain compounds, this shifting of the peaks can cause undesireable peak overlap and for multi-component samples, the patterns can become very crowded. When analyzing structures, if this drawback became apparent, standard PXRD (with Cu K-alpha X-ray source) was conducted, but otherwise, all powder patterns were collected using the SCXRD.[45]

The low temperature PXRD (located at the National High Magnetic Field Laboratory) is a standard set-up that has been integrated with a He expansion cooling system. This allows for cooling of the samples to collect powder patterns down to 10 K. Along with Rietveld refinement, this system allows for in-depth structural characterization at a wide variety of temperatures. This can be especially useful for probing phase transitions that occur above 10 K.[43,44] This PXRD technique is particularly beneficial for structural studies at low temperatures because most SCXRD systems have only liquid N_2 attachments which limit their capabilities to temperatures above 77 K. The low temperature PXRD system has the advantage of helium cooling which enables it to reach the temperatures lower than 77 K.

Volumetric and Gravimetric Hydrogen Storage Assessments

In order to quantify the maximum hydrogen capacity and obtain thermodynamic data about the products, a lab-built, gas controlling and measurement machine was used in conjunction with simultaneous thermogravimetric analysis and differential scanning calorimetry (TGA/DSC). Details of construction and methodology for volumetric studies on the lab-built machine are covered in depth later in this dissertation. TGA/DSC enables the simultaneous collection of both weight and heat flow measurements during a predetermined temperature program. A SDT 2960 Simultaneous DSC-TGA model was used in this work (TA Instruments). The function of the TGA is relatively simple, yet the calibration and standardization of the extremely precise balance and scale measurement systems inside the apparatus are much more complicated. By measuring weight, the TGA can show what temperature the materials desorb hydrogen (or another sorbent) by observing the corresponding weight change. The DSC employs a thermocouple positioned at the sample which measures the heat flow changes in the sample holder resulting from phase transitions or other processes occurring for the sample. TGA data is commonly used to report desorption weight changes and critical desorption temperatures, but is usually limited by only being able to detect desorption processes. Absorption processes can be observed in specialty built, high pressure, commercially available TGA systems made specifically for hydrogen storage studies, but for this work, TGA data was only used for desorption work while all absorption processes, quantitative or qualitative, were carried out on the lab-built volumetric hydrogen storage measurement machine.[43,45]

Electronic and Magnetic Susceptibility Properties

For products with potentially interesting electronic or magnetic properties a physical properties measurement system (PPMS) and a magnetic properties measurement system (MPMS) with a superconducting quantum interference device (SQUID) were used. The PPMS and MPMS systems are available commercially from Quantum Design.[46] Samples are attached to a long probe rod which is inserted into the system and positioned properly to allow the samples to be subjected to the desired conditions (varying temperature and applied magnetic field) and observed properly by the detection devices.

The PPMS allows for several measurements to be collected, and in this work, was used to observe the resistivity (and sometimes heat capacity) of samples during cooling or in the presence of a magnetic field. Sample preparation for resistivity measurements using the PPMS can be very tedious and involves the positioning and securing of 4 leads to a crystal sample. The leads are 0.001 inch diameter Au wire and are fixed with Ag paint that has been thinned with octyl-acetate solvent. The leads can be arranged in several ways, but for the rod or cube shaped crystals commonly produced in this work, the lead arrangements are displayed in Figure 1.10. The 4 leads consist of 2 voltage and 2 current leads which are always positioned with the current leads farthest apart and the voltage leads set between the outer current leads. This creates a current across the maximum length and cross sectional area of the crystal while allowing the voltage leads to read the current passing across the interior of the crystal. Resulting data can be organized as resistivity vs. temperature plots. The PPMS outputs resistance, which is converted to resistivity by correcting for sample cross sectional area and the spacing between leads. The calculation is very simple and is accomplished by multiplying the resistance values by the quotient of cross sectional area and the spacing between the voltage leads. The equation for this correction is shown below:

$$\rho = R * (A/d);$$

where ρ = resistivity, R = absolute resistance measured by the PPMS, A = cross sectional area of the sample and d = the spacing between the inner voltage leads.

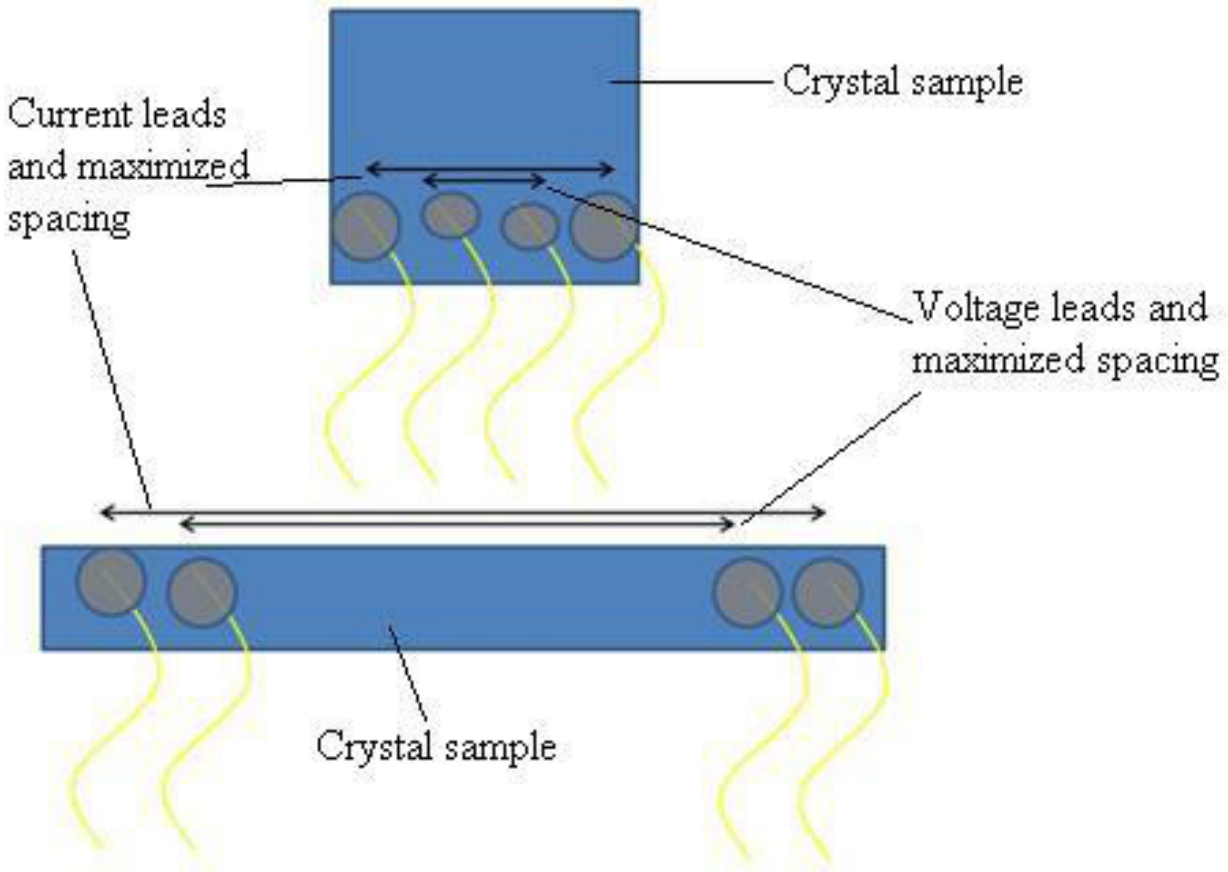

Figure 1.10 Two possible arrangements for connecting leads to a crystal sample for resistivity measurements. Arrows indicate the spacing between leads that should be maximized for collection of the most reliable data.

After samples have had leads connected, the other end of the wire is secured to its respective contact pad on the PPMS sample puck. The arrangement of the contacts on the puck can vary between systems, but for the ^{4}He system used in this work, the puck can accommodate up to 3 samples to run simultaneously. A properly prepared sample will have maximum spacing between the current leads (outermost), and then the voltage leads(innermost) can be positioned inside of the current leads and again, the spacing between the voltage leads must also be maximized. It is extremely important that none of the Ag paint overlap, as this would cause the voltage and current leads to short and obscure the collected data.

The MPMS is very similar to the PPMS in outer appearance, but functions very differently. The MPMS is equipped with a Superconducting Quantum Interference Device, or SQUID, which functions to measure the positive magnetic susceptibility of a sample that

contains magnetic atoms or Pauli paramagnetic electrons. The system can also detect diamagnetic signals which appear as negative susceptibilities. The SQUID consists of coils of superconducting material that are positioned such that the sample probe can be passed in and out of the coils. The changing magnetic flux caused by the sample motion affects the superconducting current in the coils; this is converted to an electronic signal. Sample temperature and applied magnetic field conditions can be varied, and the sample is passed through the SQUID coils at each condition. Sweeping the temperature or magnetic field yields χ (chi magnetic moment) vs. temperature and χ vs. B (applied field) plots, which can be used to characterize the magnetic properties of a sample. The MPMS is also useful to screen samples for phase transitions, superconductivity and magnetic impurities. Preparation for samples to be used in the MPMS is usually very simple and relatively quick. If single crystals are to be used, they are held between two pieces of kapton tape (usually about 6 centimeters long). The crystal, inside the kapton, is then positioned in a plastic straw and wedges of kapton are used to ensure the setup does not shift or move when it is cooled in the MPMS. Crystals that have an observable long axis, or crystals that have been oriented (with XRD or Laue system), can be positioned on the kapton tape such that the magnetic field will be parallel or perpendicular to desired orientation of the sample thus allowing for observation of anisotropic phenomena.

CHAPTER 2

DESIGN, CONSTRUCTION AND CALIBRATION OF A HYDROGEN GAS CONTROLLING AND VOLUMETRIC MEASUREMENT SYSTEM

Introduction

The emergence of a hydrogen economy will be dependant on safe and reliable methods of hydrogen storage that will include solid state storage in metal hydrides. Research and development of new materials for this purpose necessitates a unique set of tools in the laboratory. After synthesis, new or modified materials must be activated and analyzed for hydrogen absorption/desorption capacity, sorption kinetics and cycle ability.[47-49] A laboratory system that is capable of creating desired temperature and pressure conditions in a sample chamber and measuring pressure-composition isotherm (PCI) data can be utilized for hydrogenating samples and for conducting volumetric absorption/desorption analysis. Hydrogenated samples can be transferred, under protective argon, to a simultaneous DSC/TGA system for collections of thermodynamic data (for determination of the enthalpy of desorption) and gravimetric data (for calculation of the weight percent hydrogen desorbed). Gas controlling systems have been developed to enable researchers to monitor the thermodynamics and/or kinetics of reactions while creating desired conditions for samples through either manual and/or computer automated control.[50-56] Volumetric measurement systems for hydrogen storage research are commercially available, or can be built to suit in the laboratory.[57,58] The primary difference between a gas controlling system and a volumetric measurement system is the intensive calibrations involved with the latter. Due to the ideal gas law relationships of the pressure changes to the volumes of the sample chamber, an exact calibrated value for the sample chamber volume is extremely important to the accuracy of the final results. Additionally, for volumetric systems, careful

consideration must be given to temperature gradients in the tubing, non-ideality of gases at high temperatures and pressures, gas purity, system volume to sample size ratio, thermal transpiration effects, the compressibility of hydrogen, accumulative errors and leaks.[59,60] Laboratory constructed systems have the advantage of being customized to the situational requirements.

The accepted form of displaying hydrogen storage data for a metal hydride is with the use of PCI curve and its resulting Van't Hoff plot. Figure 2.2 shows a generalized PCI curve and Van't Hoff plot for a representative metal hydride sample. For the PCI curve (on the left side of Figure 2.2), the x-axis is hydrogen storage capacity (usually weight percent hydrogen or H/M, hydrogen to metal, ratio) and the y-axis is the absolute pressure used to hydrogenate the sample. The α-phase (left of the T_c curve) is the non-hydride phase and the β-phase (right of the T_c curve) is the hydride phase, while the plateau region (inside the T_c curve) indicates coexistence of both α and β phases. A longer pleateau region denotes more hydrogen is stored in the sample. At higher temperatures, less hydrogen will be stored in the sample due to the exothermic nature of hydrogenations of metals and intermetallics.

The PCI curve can be correlated graphically in the form of a Van't Hoff diagram (left side of Figure 2.2) which is used to observe the enthalpy and entropy for the non-hydride to hydride state change. The slope of the Van't Hoff plot is the enthalpy of formation and the intercept of the plot is the entropy of formation for the hydride phase (both need to be divided by the gas constant to obtain absolute values). The Van't Hoff equation used to convert the PCI data is shown in Figure 2.1. Once the PCI curve and Van't Hoff plots have been constructed, a metal hydride sample can be assessed for maximum hydrogen storage capacity and absorption/desorption thermodynamic properties.

$$\ln\left(\frac{p_{eq}}{p^0_{eq}}\right) = \frac{\Delta H}{R}\cdot\frac{1}{T} - \frac{\Delta S}{R}$$

Figure 2.1 The Van't Hoff equation used to relate pressure isotherm data to enthalpy and entropy of metal hydride formation. P_{eq} = resulting pressure after absorption, P^0_{eq} = applied pressure, ΔH = enthalpy of formation of hydride, ΔS = entropy of formation of hydride, R = universal gas constant and T = isotherm temperature.[1]

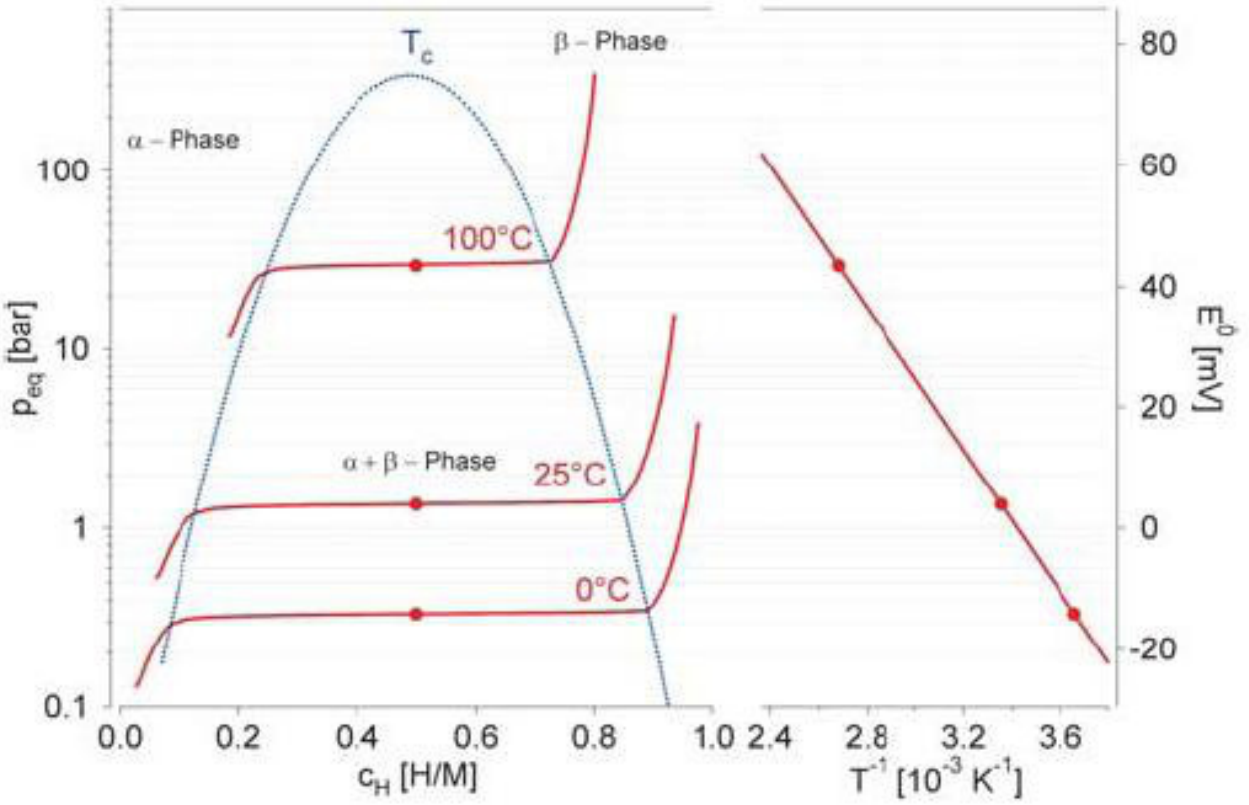

Figure 2.2 A pressure-composition isotherm (PCI) curve (*on left side)* and a resulting Van't Hoff plot (*on right side*).[1]

This work describes the design, construction, calibration and testing of a computer controlled hydrogen gas controlling and measurement closed-system device which was built to fulfill the purpose of screening newly synthesized solid state materials for hydrogen storage properties. The system was built to be capable of dynamic vacuum and 0-170 atm (0-2500 PSIG) at 25-700 °C working range. Valve actuation and data collection/conditioning are computer controlled via a desktop PC and the apparatus rests in a metal cabinet on casters, creating an easily movable system. The primary tasks performed by the system are hydrogen absorption/desorption cycles and measurement of pressure and temperature in a closed sample chamber with continuous control of the conditions. In addition to controlling hydrogen gas, the system is also capable of working with other gases such as CO_2 (for example, to measure sorption in zeolites).

Materials and Physical Construction

A built-in steel bar grid matrix was attached on the front face of the metal cabinet housing the instrumentation. To ensure a robust machine that could withstand pressure, corrosion and many duty cycles, 300 series stainless steel was used for construction of all the tubing, fittings and valves in the system. The valves and other components were bolted to the cabinet in the desired positions through the mounting brackets on the valves or by attaching a clamp to the steel bar matrix. A schematic of valve and component placement is shown in Figure 2.1. The valves are electronically actuated, Viton® o-ring ball valves with ¼" tube compression fittings (SwageLok 49 Series w/ actuator). A lift check valve (SwageLok) was installed as the first component downstream from the H_2 gas cyclinder hand valve to protect against backflow.

A 300 mL SS double ended cylinder (SwageLok) was installed to serve as system ballast dead space and this cylinder was wrapped with a 4 foot Variac controlled Samox coated resistance heating tape (range 25–700 °C). The ballast cylinder was directly connected through separate pathways to both the vacuum as well as the sample chamber. Several adapters and a 1/8" bored-through compression fitting were used to insert a 1/8" stainless steel sheathed thermocouple (k-type, Omegadyne, Inc.) into the ballast cylinder. The same fitting method was used to install the thermocouple in the sample chamber. Figure 2.3 shows how the thermocouples were installed on the sample chamber using the bored-through compression fittings. Another heating tape is wrapped around the sample chamber. The 3/8" to 1/4" compression fitting adapter was opened to fill the sample chamber then closed and tightened inside the glovebox. Standard tube compression fittings were used for the adapters and to connect the severe duty valve. Upstream from the severe duty valve, the sample chamber connects to the system with a VCR face seal fitting which was used with a fresh nickel gasket each time.

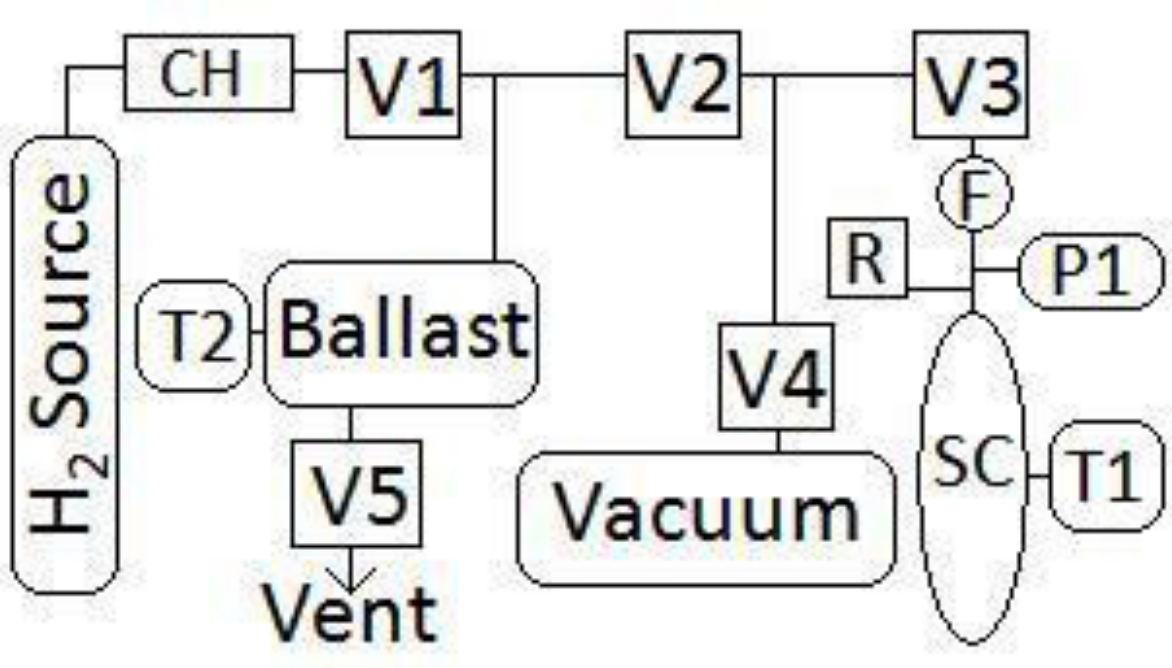

Figure 2.3 Mechanical schematic showing valves 1-5 (V1,V2,V3,V4,V5), pressure transducer (P1), thermocouples (T1, T2), one-way check valve (CH), relief valve (R), tee filter (F) and sample chamber (SC).

To protect the valves and transducer, a 2 micron filter (SwageLok) was installed as the first component upstream of the VCR fitting on the sample chamber. Just upstream of the filter, a relief valve set to ~100 atm (SwageLok) was installed to protect the system in case of overpressures. Two restriction orifices (SwageLok) were put into the system with VCR fittings, one located just downstream of the ballast cylinder (0.085 inch diameter opening), and the other located just upstream of the particulate filter (0.017 inch diameter opening). These restriction orifices slow the flow of the vacuum and the pressurized gas when it reaches the sample chamber to avoid causing the powdered samples to fly into the system which could compromise the o-ring seals of the valves. Sections of stainless steel tubing (McMaster-Carr, ¼" OD x 0.049" WT) were used to connect the valves and other components. Several tee and union tube compression fittings were used to connect the system in situations when multiple tubes are coupled or the tubing cannot be bent. A 220 V RV-3 rotary vane vacuum pump (BOC Edwards) was attached onto the system with two KF25 flanged (36" length, SwageLok) flexible stainless steel vacuum tubing sections installed with Viton® o-rings on either side of a u-shaped trap. This trap leading to the vacuum pump served to provide even more ballast dead space for efficient evacuation of

the system. On the back side of the cabinet, electronic components were mounted on a G-6 insulated polymer board which was then attached to the cabinet by means of four hex bolts with insulating grommets.

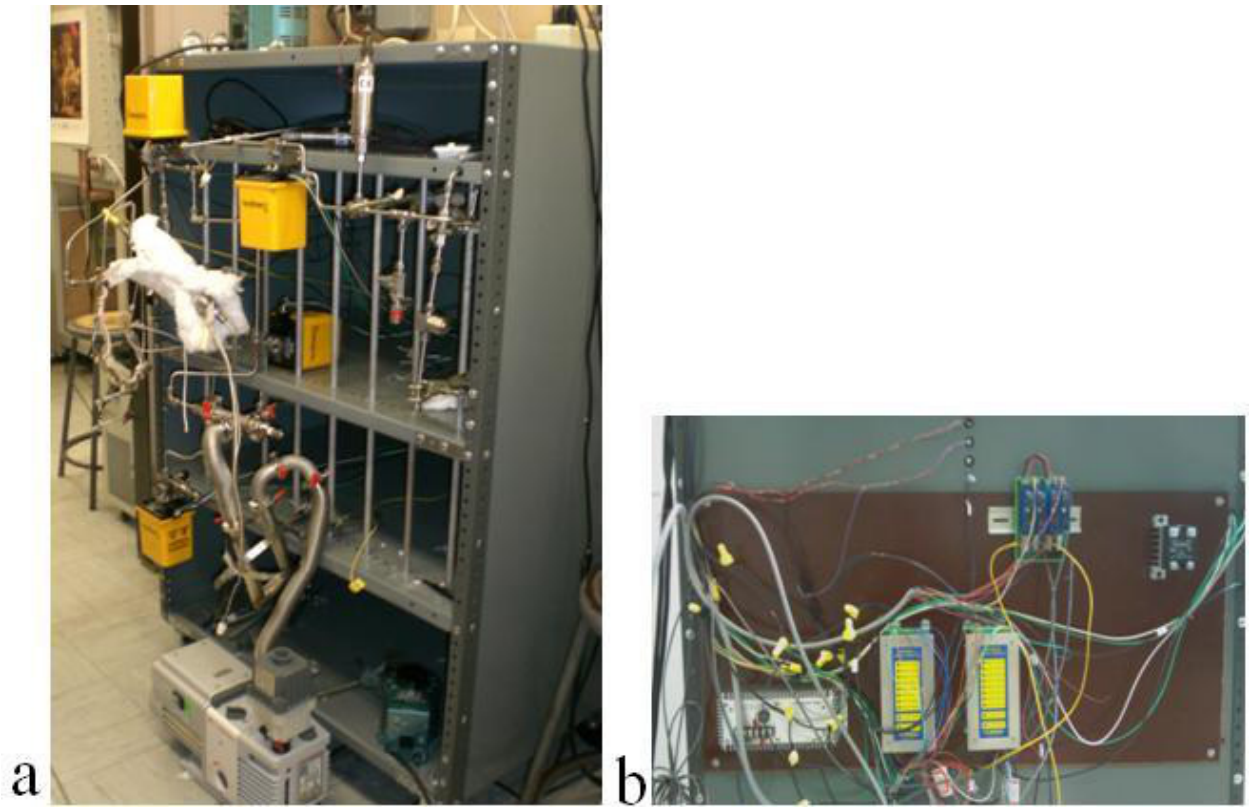

Figure 2.4 Photographs of the front of the system showing valves, transducer, filter, relief valve, vacuum pump and ballast dead space volume (a) and the back of the system with relay modules, power supplies and signal conditioning equipment (b).

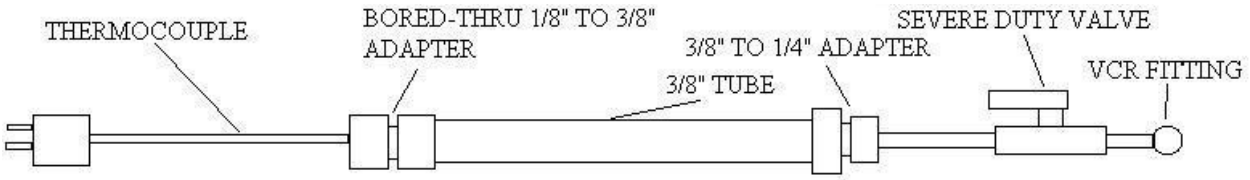

Figure 2.5 The set up for the bored-through thermocouple attachment and connections for the system.

Electrical Components and Programming

A desktop computer (Dell) was used to program data collection and control valves. The electronics board mounted on the back of the cabinet holds the transducer power supply, signal conditioning equipment and relay modules (National Instruments). Output wiring of the thermocouples connects to the signal conditioning equipment which was then wired to communicate and be powered by the DAQ card. A PCI card (National Instruments) was installed into the computer which was connected to the terminal block with the appropriate cable. Bundled 24 G wiring served two purposes: to connect the analog input signals from the data conditioning equipment and connect the output signals to the terminal blocks on valve actuators. This bundle serves as the I/O cable from the system to the computer. Both pressure transducer wiring harnesses and thermocouples were directly wired to the signal conditioning equipment with the either 24 G wire or thermocouple wire, respectively. The matching power supply was connected to the wire harnesses on the pressure transducers with 24 G wire, while the power supply terminals on the valve actuators were daisy-chain wired with 12 G to the relay modules. The relay modules were then wired to standard outlet plugs with 12 G wire. Each output wire in the I/O bundle corresponds to a port on the DAQ card so each valve can be assigned a port according to Table 2.1. This allows for each valve to be kept open or closed for any amount of desired time and in the event that a relay is damaged, it can be isolated and quickly replaced.

Table 2.1 Data acquisition card port assignments of open and closed positions for each of the 6 valves.

Valve	Port	Valve	Port
1-open	0.0	5-closed	0.7
1-closed	0.1	6-open	1.0
2-open	0.2	6-closed	1.1
2-closed	0.3		
3-open	0.8		
3-closed	0.9		
4-open	0.4		
4-closed	0.5		
5-open	0.6		

LabView test panel was used to test valves after initial construction while an integrated set of virtual instruments (VI) were used to run the processes. Once the system was physically constructed, programming in LabView (National Instruments) was established to run the system in one of two modes: automatic or manual. In automatic mode, the program was designed to accept cycle number and delay time parameters from the user. The cycle number will be the number of times the sample chamber will be pressurized or depressurized at the desired pressure. The delay time will be the amount of time the sample is exposed to the pressure conditions of the upstream system. For example, if a user desired to pressurize a sample to 500 PSIG for 25 cycles with 10 minutes for each cycle, then the regulator would be set to 500 PSIG, and the user would input 25 and 10 into the program. The advantage of using the automatic mode is that the user does not have to monitor the system, which is especially convenient when long pressurizations or many cycles are required for a sample. The manual mode offers real-time full customizability of the system's function. Valves can be individually opened and closed at any desired time by clicking icons in the program. For either operating mode, the computer will collect temperature and pressure data at 0.5 second intervals and write the data to an ASCII file whose filename and location have been entered by the user via a computer prompt (which is part of the programming).

Calibrations

The pressure transducers were calibrated using a custom designed LabView program in conjunction with a secondary lab-built system consisting of a 1 L stainless steel bottle and several hand valves, which allows the user to employ a pressure standard to be used for calibration. For initial calibrations, an analog dial test gauge (Omega) that has 5 psi subdivisions, grade 3A accuracy 0.25% (range 0-1500 PSIG) was used. Hysteresis and deviation from linearity can be corrected and once done, the measurement data was collected using the calibration plot previously determined by the virtual instrument program. Through the program, the user can connect any reliable external pressure standard to the system and introduce pressure from the main gas bottle. The program will prompt for the pressure as read off the pressure

standard and automatically correct this to the reading given from the pressure transducer being calibrated. In the event that a transducer is suspected to be out of proper calibration, it can simply to re-calibrated using the program and the analog dial test gauge or another pressure standard.

Calibrations of the sample chamber volume were not needed for activation and hydrogenation processes, but will be necessary for future use of the system to collect volumetric absorption and desorption data. This volume consists of the free space from valve 3 (the first valve upstream from the sample chamber) to the sample chamber, and includes the volume of the severe-duty valve, filter, relief valve, restriction orifice and all fittings. Since this includes many complex and small volumes, determination of this free space was impossible to obtain by water displacement. A simple solution was to decompose a pre-weighed sample of pure, commercially obtained MgH_2 into the system and measure the resulting pressure increase. This change in pressure was related with the ideal gas law to the known number of moles of H_2 stored in the MgH_2 (from the mass) and the resulting volume was assessed. Initial calibrations using this method proved it viable, but exact determination will require many runs to determine the error and deviations in these measurements. Also, for accuracy using this calibration method, a vacuum gauge must be installed on the system (the current transducers measure only positive pressures). A compiled plot of four desorptions of MgH_2 is shown in Figure 2.6 and displays how larger sample sizes result in a higher final pressure in the system. The x-axis in the plot is time and the y-axis is the pressure in the system. The differences in the time the samples desorbed were irrelevant to the final total pressure and were caused by the system being run in manual mode. Valve 3 remained closed during the measurement so the pressure reading from the transducer represents the resulting pressure in the volume which needed to be determined. MgH_2 is very suited for these measurements because the system was designed to work with Mg and Mg-based intermetallics, but CaH_2 and TiH_2 (both commercially available) could also be used as standards for calibration.

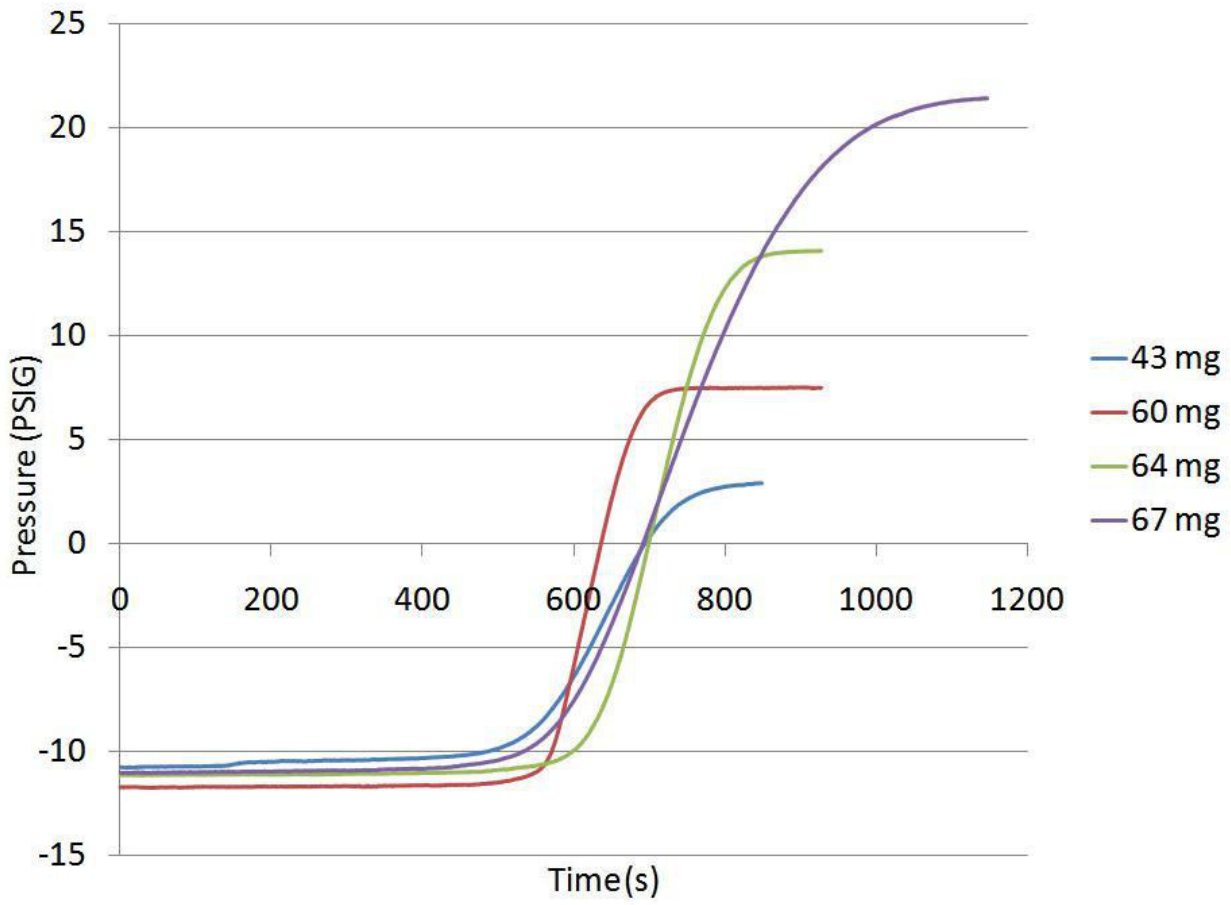

Figure 2.6 Desorptions of MgH_2 that were used to determine a rough estimate of the system volume downstream of the final valve to the sample chamber. The x-axis is time and y-axis is applied pressure in the system. The desorptions were time normalized.

To minimize the amount of thermocouple wire used (thereby preventing increased noise from long runs of thermocouple wire), the thermocouples were connected with the thermocouple wire directly to the signal conditioning equipment mounted on the back of the cabinet. Output of the signal conditioning equipment is 0-5 V, so normal stranded copper wire was used to connect it to the terminal block. The copper wire conducts with the least amount of added noise so that the conditioned output signals reflect the correct readings to be received by the computer.

Activation and Hydrogenation Procedure

The majority of samples which were run in the system were Mg-based solid state materials in powder form. Each sample had specific requirements for handling and preparation prior to insertion into the sample chamber and connection to the system. Usually, this involved ball milling the raw sample to obtain a fine powder (with maximized surface area) then loading this powder into the sample chamber (with severe duty valve closed) inside a drybox. Next, the sample chamber was connected to the machine via the VCR fitting. Heat was then applied to the sample chamber and the maximum temperature was determined by the melting/decomposition point of the sample (if this was known) and the constituent elements in the material. The sample chamber was evacuated and held at the maximum temperature for at least 30 minutes to drive off surface impurities. Gas was then introduced into the sample chamber at the desired pressure (usually near 500 PSIG) and the sample was allowed to reach equilibrium with the gas most often for at least 30 minutes. Depending on the sample, this step could take much longer if the kinetics of hydrogen diffusion into the lattice of the sample is very slow. Regardless, any length of time could be chosen for this step. For most activation and hydrogenation processes, the manual operating mode offers the most versatility and ease of use. After the desired time had passed, the heat was removed from the sample chamber and it was allowed to cool under the gas pressure. After cooling, the pressure was vented and the sample could be removed for immediate transfer to another instrument or a storage container.

In order to create a full PCI curve and Van't Hoff plot (see Figure 2.for a metal hydride, the sample must be tested for hydrogen storage capacity at a range of pressures using a constant temperature. In most cases, two or three isotherm temperatures are chosen and should differ by no more than 50 °C. The smaller the step size of the pressure variation, the more data points that will be created on the PCI curve. At each pressure, the sample is hydrogenated and then dehydrogenated to measure the amount of hydrogen stored and the data from these cycles can be plotted as pressure drops in the sample chamber. Figure 2.7 shows the plot of absorption from a composite of Ca-Mg-Si-Fe. As the pressure decreases due to absorption by sample, the system delays correcting the sample chamber pressure back to the desired applied pressure by an amount of time pre-set by the user. When valve 3 is opened, the sample chamber will re-equilibrate with

the set applied pressure. Closing valve 3 after 5 seconds allows the sample to absorb hydrogen and the resulting pressure drop can be recorded. As the applied pressure is re-equilibrated over the pre-set time delays, the pressure drop will decrease from the sample becoming saturated. The sample will continue to absorb more hydrogen until its maximum hydrogen storage capacity for the applied pressure is obtained. Since this process of measuring maximum hydrogen storage capacity must be repeated at all the desired pressure values, the automatic mode of the program saves time and user interaction requirements. The user will set the applied pressure and allow the system to run automatically until the measurement is done. Then the user will set the new pressure and allow the system to repeat the automatic measurement. Although reliable volumetric measurements have not been collected on the system yet, future work will be directed toward sample chamber volume calibrations enabling volumetric measurements to obtain PCI and Van't Hoff plots.

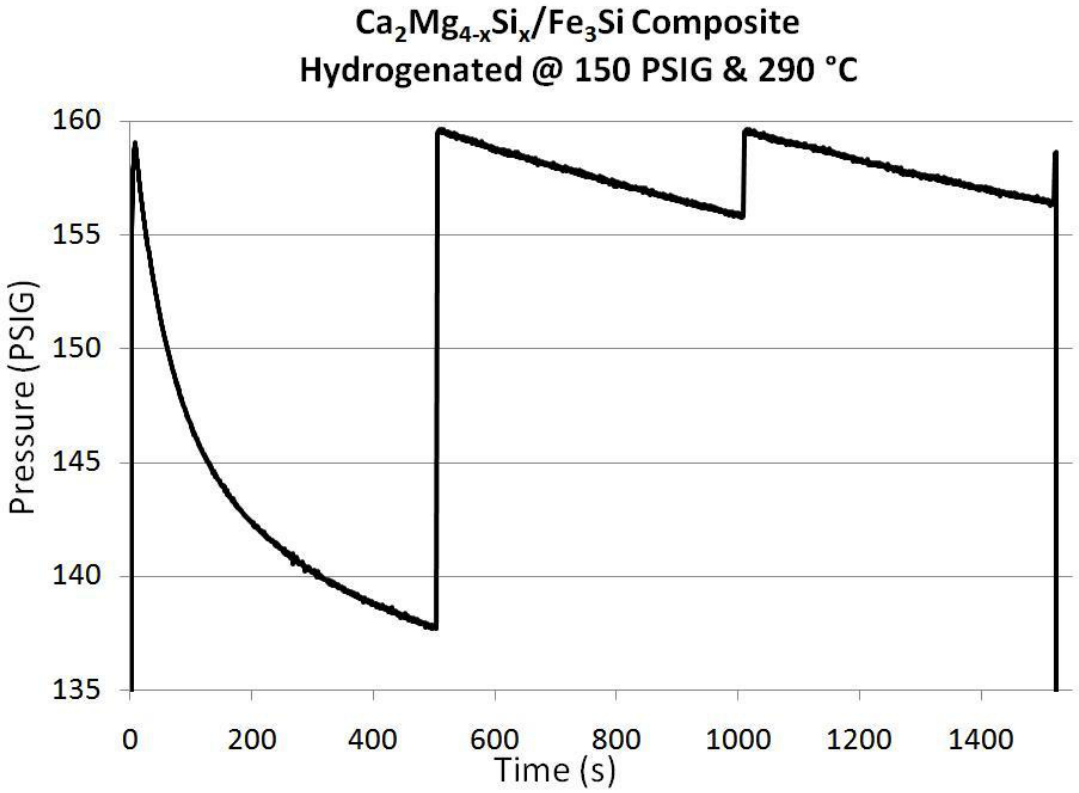

Figure 2.7 Absorption plot from a Ca-Mg-Si-Fe composite showing the absolute pressure of the sample chamber vs. time. The data was collected using the automatic mode program at the indicated conditions.

Final Discussion

The need for a system which can activate and hydrogenate materials was the motivation for construction of the gas controlling and measurement system. Creating desired temperature and pressure conditions is important to screening and initial assessment of potential hydrogen storage materials. The symbiosis of a hydrogen storage synthesis lab coupled with a gas controlling device and TGA/DSC allows for the production of new materials and their testing in the same laboratory. The ability to activate and hydrogenate samples then bring them to the DSC/TGA allows for characterization of hydrogen desorption properties. Future work will focus on volume calibration of the machine so that it will be capable of volumetric hydrogen storage determination of samples. This process will be intensive in terms of calibrations, error reduction and leak detection, but the robust construction of the machine will allow for future incorporation of more sophisticated components that will improve the overall function of the machine and enable new capabilities.

CHAPTER 3

SYNTHESIS METHODS FOR MAGNESIUM-BASED INTERMETALLICS AND ALLOYS

Molten Metal Fluxes

Magnesium rich phases are attractive as potential hydrogen storage compounds because of the low cost and mass of Mg. Materials comprised of lightweight metals are likely to have high weight percent hydrogen capacities. Mg-based materials with high gravimetric hydrogen capacity would be particularly desirable for transportation applications. The relative safety, low weight and cost combined with the high gravimetric and volumetric capacities of some Mg-based phases make these materials candidates for replacing existing large, heavy compressed H_2 gas tanks to provide fuel for fuel cells.

Mg-based intermetallics and the properties of their hydrides will borrow from the properties of their constituent elements in some way. For example, MgH_2 has high hydrogen capacity of 7.6 weight percent, but unfavorable desorption temperature of 450 °C due to the strong interactions of magnesium with hydrogen (Mg is a typical hydride forming, "A" type element). On the other hand, the intermetallic hydride Mg_2NiH_4 has a hydrogen capacity of only 1.7 weight percent, but shows significant lowering of the critical desorption temperature (T_c = 180 °C).[70] The lowered desorption temperature of $MgNiH_4$ compared to MgH_2 can be attributed to the non-hydride "B" type nature of Ni. Aside from A/B composition, the differing crystal structures and atom positions within a metallic crystal lattice can facilitate or hinder hydrogen interactions.[61,62] The packing of atoms in the structure determines the size of interstitial sites and the ability of atomic hydrogen to migrate through the lattice; this can be optimized through the substitution of elements with slightly different sizes into the structure.[63-69] Ideally, this substitution will not induce a structure change, instead yielding a solid solution. For instance, in a compound AB_5, element C can substitute for element B to form a solid solution $AB_{5-x}C_x$ if B

and C are similar enough in size, valence electron count (vec) and electronegativity. Large differences in size or electronegativity will limit the ability of these elements to form a solid solution (x will be low). These guidelines of substitution based on size, vec and electronegativity are commonly referred to as "Hume-Rothery Rules". Intermetallics with a large phase width can vary unit cell dimensions significantly to accommodate varying concentrations of differently sized dopant reactants. A good example of this substitution is the case of Mg_2Ni, which displays a moderate phase width and has been extensively tested for the effects of doping of Mn, Fe, Co, Cu on the Ni site and Zn or Li, Ca, Al and La on the Mg site. The compound $Mg_{1.92}Al_{0.8}Ni$ has a reported hydrogen storage capacity of 3.5 weight percent and T_c = 295 °C.[70]

Elemental Mg has the ability to form solid solution alloys with many other elements, such as Al and Li. Mg also has a tendency to behave outside the predicted reactivity based on periodic trends. In the case of elements that have good solubilities in Mg, alloys can be formed that retain the Mg structure type and substitute dopants into the lattice. Solid solution Mg-based alloys have the drawback of being particularly prone to disproportionation reactions which separate the Mg matrix from the dopants dissolved within it. This separation destroys the interactions of the dopants with the Mg matrix and reduces the effects of the presence of the dopants, thus reverting the the Mg-based alloy back to a material that behaves like pure Mg. This disproportionation effect makes reversible hydriding impossible for many Mg-based alloys.

Syntheses with Mg are hindered by the physical properties of the metal including its corrosive nature and high vapor pressure at temperatures above 650 °C. Traditional high temperature melts are particularly constrained by the vapor pressure of Mg, which increases with increasing temperature. Reactive ball milling offers some low temperature synthesis options, but this technique is most useful for preparation of previously synthesized hydrogen storage materials. The flux method used in this work has advantages when conducting reactions of Mg metal because it allows for lower reaction temperatures and containment of the Mg vapors. Normally, flux synthesis can be carried out in crucibles that are not sealed (see Figure 3.1), but in case of Mg containing reactions, sealed crucibles are necessary to contain the Mg vapors which are created when Mg metal is heated above its melting point of 650 °C. Mg flux reactions were initially carried out in alumina crucibles which were open to the vacuum inside the sealed quartz ampoule. Upon heating, the Mg would vaporize and react with the quartz to make it very brittle

and black in color. The side reaction of the Mg vapors with the silica consumed the Mg flux and this loss of the flux pool eliminated the crystal growth environment. In most cases the quartz became so brittle and cracked with hairline fractures that it would shatter upon centrifugation. There was never solidified flux found at the opposite end of the crucible which is the usual sign of successful flux removal. The use of alumina crucibles was clearly problematic and this part of the synthesis was modified quickly to improve and control the reaction conditions.

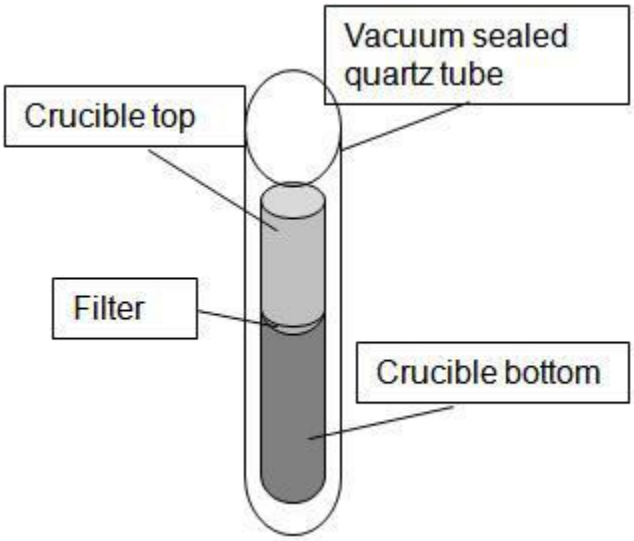

Figure 3.1 Initial set up for reactions that was insufficient to contain the Mg vapors and thus, caused degradation of the quartz ampoule.

Stainless steel was chosen for crucible material because it is inexpensive, commercially available in many diameters and is easily welded. Variations of stainless steel tubing diameter and wall thickness (with corresponding silica tubing) were tested in synthesis and the most easily handled was 13 mm OD silica tubing with 7.5 mm OD and 1.5 mm WT stainless steel tubing. In order to weld the tubing, a commercially available MIG/TIG welder (Miller Sychrowave 200) was installed in an Ar glovebox equipped with a water cooled Cu welding block. Tubing was measured and cut and one end was welded to form an open ended crucible. The reaction was then loaded into the crucible and the second end was welded shut. Welded crucibles made from cut sections of relatively inexpensive 304/304L stainless steel tubing were ideal for exploratory reactions of Mg due to the low reactivity of Fe-C steel alloys with Mg. The use of stainless steel

did introduce some Cr, Ni and Fe impurities into certain crystals. These impurities become highly problematic in compounds with interesting magnetic properties; even traces of Fe can obfuscate magnetic data. Therefore, when interesting phases were found, the reactions were repeated in niobium or tantalum crucibles to eliminate impurities and obtain pure phase products for detailed characterization and analysis. Niobium crucibles offer the utmost protection against impurity incorporations, but require more welding skill and are over twice as expensive as stainless steel reaction vessels.

The results presented in this chapter represent early work with Mg-flux that was mostly conducted in alumina crucibles before the development of the welded stainless steel techniques. This early work exposed many of the synthetic difficulties and challenges. In most of this early work, extensive characterization and analysis was not conducted due to irreproducibility issues and the inherent problems with the escaping Mg vapors. The synthesis methods that were developed to deal with Mg led to later reactions (described in later chapters) that were predictable and reproducible to allow for very in-depth work with the resulting crystals. There was enough control, though, in these early reactions to explore the substitution effects from varying starting reactions.

Initial Work on Mg-Ni, Mg-Zn and Mg-Cu Fluxes

In attempts to create compounds containing significant amounts of Mg and a transition metal, reactions were conducted with pure Mg flux and with Mg-(Ni, Cu, Zn) eutectic fluxes. These reactions yielded only Mg deficient phases due to the escaping Mg vapors. They also tended to create products that were not clean single crystals, but instead, polycrystalline materials as part of multi-phase products. With later improved synthetic methods in sealed metal crucibles, many of the Mg-(Ni, Cu, Zn) flux reactions were revisited and products obtained were stored in the crystal bank. Mg-late transition metal eutectic fluxes are attractive synthesis media due to the increased solubility of secondary reactants in transition metals, the high concentration of late transition metal that can be solvated by Mg and the catalytic activity of late transition metals towards gases like H_2. Only Ni, Cu and Zn have significant solubilities and eutectics with Mg, while the early 3d transition metals exhibit almost zero solubility and raise the melting point of a Mg-transition metal mixture even at low concentrations. Table 3.1 shows the melting

temperatures and corresponding ratios of the explored Mg- (Ni, Cu, Zn) eutectics. In particular, the Mg-Cu system offers three usable eutectic mixtures that become increasingly Cu rich, which enables reactions of certain elements which may be soluble in Cu, but not Mg. For example, the B is very insoluble in Mg, but has much better solubility in Cu.

Table 3.1 Eutectic mixtures of Mg-(Ni, Cu, Zn) that melt at feasible temperatures for flux removal by centrifugation.

Elements	Molar Ratio	M.P. (°C)
Mg-Ni	88.7 / 11.3	506
Mg-Cu	85.5 / 14.5	485
Mg-Cu	58.0 / 42.0	552
Mg-Cu	23.1 / 76.9	725
Mg-Zn	71.9 / 28.1	340
Mg-Zn	7.8 / 92.2	364

$Mg_6Ni_{16}Si_7$ The synthesis of $Mg_6Ni_{16}Si_7$ occurred as a result of escaping Mg vapors that lowered the concentration of Mg in the flux until it could no longer act a solvent for crystal growth. This phase has the Th_6Mn_{23} structure type, which is known to absorb hydrogen. The structure features one perfectly cubic Si coordination and another prismatic Si site which has much lower symmetry. The Mg atoms reside in cages with caps of Si-Ni polyhedrons and 4 Mg atoms bonded to make the bottom of the cage. The Mg-Ni, Mg-Si, Ni-Ni and Ni-Si bond lengths are 2.72 Å, 2.87 Å, 2.55 Å and 2.31 Å, respectively. Figure 3.2 shows the unit cell and local environments of the $Mg_6Ni_{16}Si_7$ structure, while Table 3.2 displays the crystallographic information. The maximum gravimetric hydrogen capacity of $Mg_6Ni_{16}Si_7$ will be very limited due to the large concentration of heavy Ni atoms in the compound.

Previous literature indicates this compound has a very large phase width for the concentration of Ni in the compound so that it could be written as $Mg_6Ni_{16+x}Si_{7-x}$ with $0 < x < 3$. This compound, along with other $R_6T_{16}X_7$ phases, belongs to a group of intermetallics that are ordered ternary variants of the R_6T_{23} structure, where X atoms occupy specific crystallographic sites. Variations of synthetic method lead to the different stoichiometries of the compound, all having the same structure. This structure type has been referred to as the G-phase, or η phase, of Th_6Mn_{23}. Normal metallic behavior has been reported, with some groups investigating for

possible superconductivity (this was not found). The compound has several analogs $M_6Ni_{16}Si_7$ (M = Mg, Sc, Ti, Nb, Ta). The $Mg_6Ni_{16}[Si_xP_{1-x}]_7$ compound has been explored as a solid solution.[140-142] Little work has been done on solid solutions of $Mg_6X_{16}Si_7$ (X = Ni, Cu) despite the fact that the fully substituted version, $Mg_6Cu_{16}Si_7$, being the first reported compound with that representative stoichiometry. The end members of the $Mg_6Ni_{16-x}Cu_xSi_7$ series, $Mg_6Ni_{16}Si_7$ and $Mg_6Cu_{16}Si_7$, have unit cell parameters of 11.3164(19) Å and 11.65(2) Å, respectively.[74]

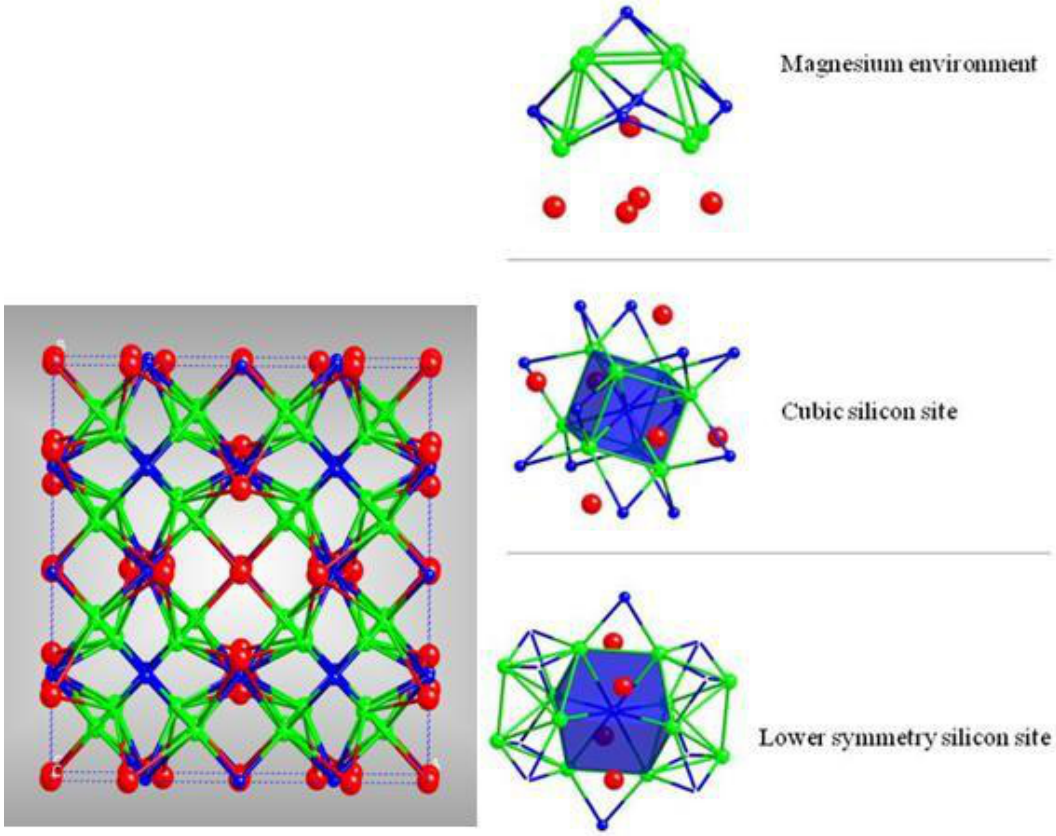

Figure 3.2 The unit cell of $Mg_6Ni_{16}Si_7$ and the local envoirnments for the Mg and Si atoms.

Mg flux synthesis was carried out to explore the Mg / Ni / Cu / Si systems. The $Mg_6Ni_{16-x}Cu_xSi_7$ compounds were synthesized in open stainless steel crucibles using fiberfrax filters. A mixture of Mg / Ni / Si was combined at a 9 / 1.8 / 1 ratio and heated to 950 °C. At this high temperature the Mg metal sublimates and reacts with the quartz glass tube. This removal of Mg from the reaction may actually facilitate the growth of $Mg_6Ni_{16}Si_7$, which is notably Mg-poor

and Ni-rich. After holding the reactions at 950 °C for 40 hours, the samples were cooled to 650 °C in 20 hours and centrifuged to ensure removal of any residual flux. The same synthesis procedure was used to make all the substituted analogs of $Mg_6Ni_{16-x}Cu_xSi_7$; see table 3.3.

Table 3.2 Crystallographic data for $Mg_6Ni_{16}Si_7$.

Space group	*Fm-3m*
Data collection temperature, K	298
Cell parameter, Å	a = 11.3111(4)
V, Å^3	1447.15(9)
Wyckoff Site and Atom Positions	96*k* Ni1 (0.38198(6), 0.11802(6), 0.11802(6)) 96*k* Ni2 (0.33170(6), 0.33170(6), 0.16830(6)) 24*e* Si1 (1/2, 0, 0) 24*d* Si2 (1/4, 0, 1/4) 96*j* Mg1 (1/2, 0, 0.2955(4))
Z	3
Density (calc.), g cm^{-3}	4.413
μ, mm^{-1}	15.813
Data collection range, deg.	3.12< θ < 28.25
Reflections collected	5031
Independent reflections	125 [R_{int} = 0.0306]
Parameters refined	15
R_1[a)], wR_2 [b)] [$F_o > 4\sigma F_o$]	0.0224, 0.0464
R_1, wR_2 (all data)	0.0226, 0.0464
Largest diff. peak and hole [e/Å^3]	0.765 and –0.818
Goodness-of-fit	1.499

[a)] $R_1 = \Sigma \| F_o | - | F_c \| / \Sigma | F_o \|$.

[b)] $wR_2 = [\Sigma w(F_o^2 - F_c^2)^2 / \Sigma w(F_o^2)^2]^{1/2}$, $w = [\sigma^2(F_o^2) + (A \cdot p)^2 + B \cdot p]^{-1}$; $p = (F_o^2 + 2F_c^2)/3$; A = 0.0067, B = 0.

Although the amount of substitution was not well controlled, the target phase was formed as long as the Mg, Si and transition metal were present. Products of each reaction had varying amounts of Ni / Cu substitution which indicates the solubility and mobility of the reactants in the flux may be too low to allow for proper mixing, even at high temperature.

Table 3.3 Reactions of Mg / Ni / Si / Cu at varied ratios. Cr and Fe impurities were leached from the stainless steel crucible material. Cu / Ni ratios deviated from expected concentrations based on starting reactions.

Reaction Name	Mg / Ni / Si / Cu Ratio	Mg (at%)	Cu (at%)	Ni (at%)	Si (at%)	Cr / Fe (at %)
Mix 1	9 / 1.6 / 1 / 0	2	0	4	32	14 / 47
Mix 2	9 / 1.6 / 1 / 0.3	10	10	46	30	0 / 0
Mix 3	9 / 1.6 / 1 / 0.7	6	50	22	18	0 / 5
Mix 4	9 / 1.6 / 1 / 1.1	11	21	46	24	0 / 0
Mix 5	9 / 1.6 / 1 / 1.5	12	33	36	18	0 / 0
Mix 6	9 / 1.1 / 1 / 1.5	10	45	30	17	0 / 2
Mix 7	9 / 0.7 / 1 / 1.5	11	18	53	15	0 / 4
Mix 8	9 / 0.3 / 1 / 1.5	21	47	18	15	0 / 2
Mix 9	9 / 0 / 1 / 1.5	12	80	1	6	0 / 4

SCXRD was used to obtain crystallographic data for end member $Mg_6Ni_{16}Si_7$, but PXRD provided better averaging of the substitution levels for the $Mg_6Ni_{16-x}Cu_xSi_7$ series. After the PXRD data was collected, plotting this data as unit cell parameter vs. composition led to non-linearity resulting from the poor solubility and diffusion in the reactions. The synthetic uncertainties made the unit cell parameters vary much more than expected based on starting reaction. The uncontrolled nature of the substitution in the products was evident in the widely varying EDS values shown in Table 3.3. The lack of control was partially due to the similar atomic radii of Ni and Cu of 1.35 Å and 1.28 Å, respectively. Isolated regions would have differing concentrations of Ni and Cu which could both substitute into the structure easily.[5]

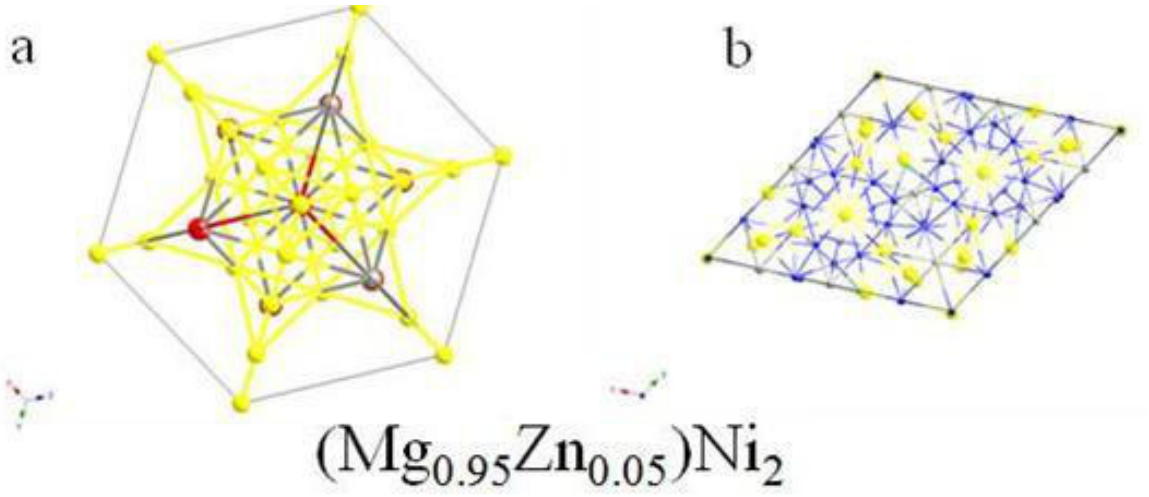

Figure 3.3 Unit cell (a) and expanded lattice (b) views of $(Mg_{0.95}Zn_{0.05})Ni_2$.

Further work with the $Mg_6(Ni/Cu)_{16}Si_7$ system was not conducted due to lack of reproducibility. Reactions of pure Mg flux and Mg-(Ni, Cu, Zn) eutectic fluxes did yield more compounds such as $(Mg_{0.95}Zn_{0.05})Ni_2$ (cubic *Fd*-3*m*, *a* = 7.1176(2), R = 0.0186). The unit cell and expanded view of this compound are shown in Figure 3.3. This was the first compound synthesized in this work with transition metal substitution onto a site normally occupied by Mg. Later work with the Mg-Ga flux resulted in compounds that exhibited similar substitution behavior. The interest in this substitution came from the possible higher activity of the Mg site during hydrogenation-dehydrogenation cycles. Other similar Laves phase compounds have shown small hydrogen storage capacity (<2.0 weight percent).[70] $(Mg_{0.95}Zn_{0.05})Ni_2$ is expected to be related to either Mg_2Ni (C36 Laves phase, $P6_322$ *a* = *b* = 5.205(1) Å, *c* = 13.236(2) Å) or $MgNi_2$ (C14 Laves phase, *P*63*/mmc a* = *b* = 4.824(2) Å, *c* = 15.82(3) Å).[74] Instead, even a small amount of substitution of Zn on the Mg site causes the compound to adopt a cubic symmetry like that of $MgCu_2$ (C15 Laves phase, *Fd*-3*m a* = *b* = *c* = 7.034(2)). In addition to $(Mg_{0.95}Zn_{0.05})Ni_2$, the products of the reactions would also contain the compounds Mg_2Ni, $MgZn_2$ and Mg_2Zn_{11}. Due to the multi-phase nature of the products, hydrogen storage measurements were not carried out, but previous studies have reported the hydrogen storage capacity of Zn-doped Mg_2Ni to actually be slightly worse than pure Mg_2Ni.[70]

Mg-Ga Flux

Use of Mg-Ga flux is complicated by the fact that gallium reacts with many metal crucible materials, and Mg vapors attack ceramics. For pure Ga flux reactions, alumina crucibles perform well and are not destroyed by the flux reaction, but stainless steel crucibles will react with liquid Ga. For Mg flux reactions, the alumina crucibles were unable to contain the Mg vapors, making welded stainless steel the best option as a crucible material. A mixed Mg-Ga flux reaction necessitates containment of the Mg vapors in a crucible not reactive with Ga. This led to a flux ratio choice that was rich in Ga and contained a smaller amount of Mg (8 / 2 for Ga / Mg), which was not conducive towards the growth of Mg-rich phases, but did allow for reactions to be carried out in alumina. The Ga rich flux was able to retain most of the Mg in the liquid phase.

Most of the phases synthesized from this flux were substituted binary phases that had two or three elements that could substitute on the same crystallographic site. In certain cases it was possible to dope Mg into transition metal sites, or vice versa. Since the products were substituted variants of known phases, the compounds were screened for composition and structure only. The crystals formed were not large enough to allow for extensive characterization and the relatively simple nature of these known compounds made the possibility for new interesting properties unlikely.

Samples were synthesized in alumina crucibles due to the flux ratio for Mg / Ga of 2 / 8 chosen for most reactions. This ratio does not correspond to a eutectic in the Mg-Ga system (see Figure 3.4). Due to the low melting point of Ga, centrifugation was possible at moderate temperatures (below 600 °C). Samples were combined and heated to 950 °C and cooled to the desired centrifugation temperature (usually 550 °C) in 40 hours. Mg vapor did escape the reaction vessel and this was evident by slight discoloration of the quartz glass tubing, but most of the Mg remained dissolved in the Ga flux.

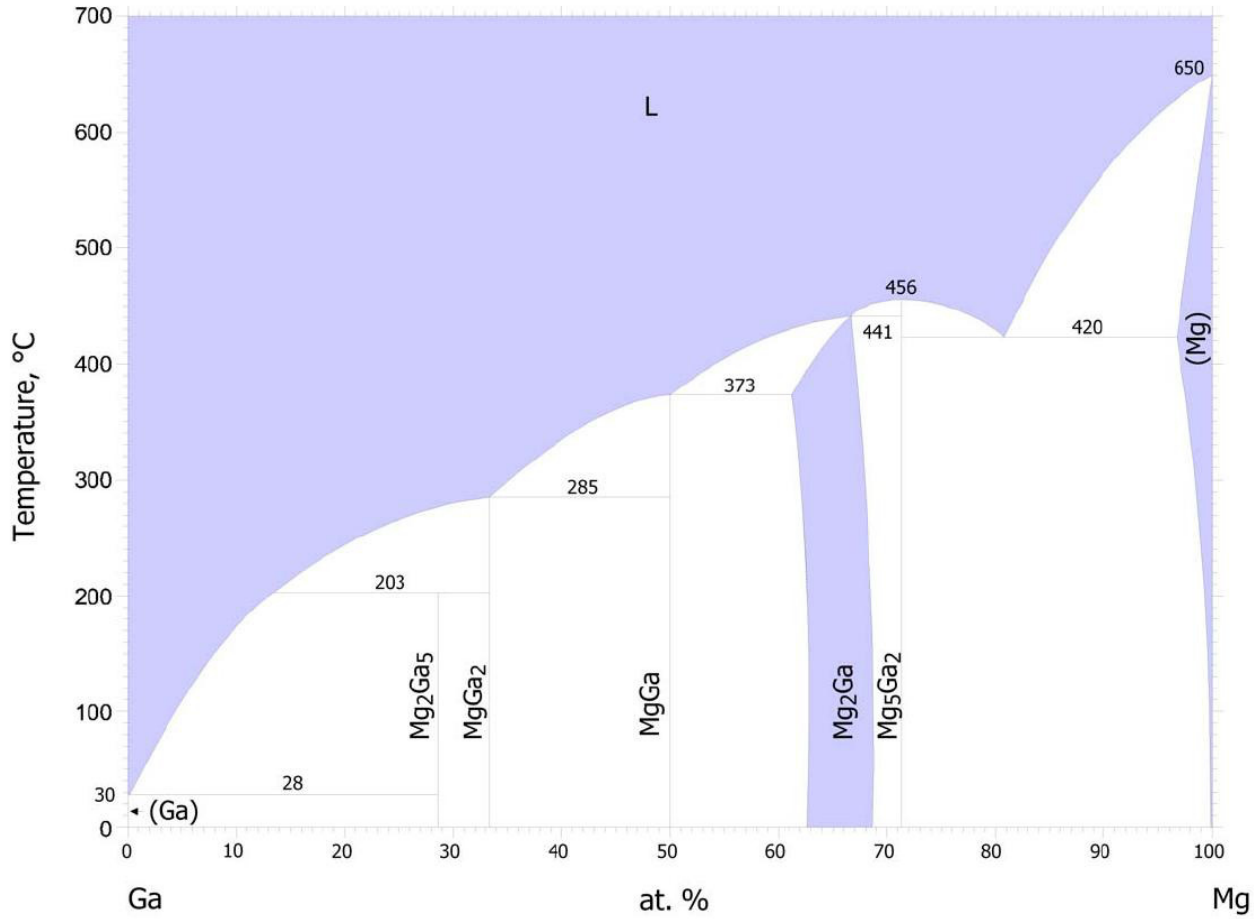

Figure 3.4 Phase diagram for the Mg-Ga binary system.[30]

Three simple binary phases were formed that exemplified the substitution of Mg for small amounts of transition metal. The first phase was synthesized with Cu on the Mg site in the structure shown in Figure 3.5. The compound had stoichiometry of $CaGa_2Mg_{1.86}Cu_{0.14}$ (tetragonal-I *I*4*/mmm*, $a = b = 4.3370(4)$ Å, $c = 11.6058(5)$ Å, R = 0.0133). The crystals of this phase did not form large single crystals, but instead a polycrystalline bulk product that had varying levels of substitution. Two other phases exhibited Ni substitution on the Mg site. The first (structure is shown in Figure 3.6) was $(Mg_{0.985}Ni_{0.015})Ga_2$ (hexagonal $P6_3mc$, $a = b = 5.0426(6)$ Å, $c = 7.9765(8)$ Å, R = 0.0317), which is structurally related to the parent compound $MgGa_2$ ($P6_3/mmc$ $a = b = 4.343$ Å, $c = 6.982$ Å). The second was trigonal $Mg_{2.65}Ni_{0.35}Ga_3$ (*R*-3, $a=b=5.0026(3)$ Å, $c = 11.132(1)$ Å, R = .0216) whose parent compound is MgGa ($I4_1/a$ $a = b = 10.53$ Å, $c = 5.53$ Å). Both products were simultaneously present in reactions of Mg / Ga / Ni

at 8 / 2 / 2 mmol ratio which was heated to 700 °C in 10 hours, held for 5 hours, cooled to 500 °C in 20 hours and then centrifuged. These two phases were formed in a similar manner. When the flux was removed, the products were found stuck to the bottom of the crucible as a solid layer of crystals. This made isolation of a single phase very difficult, and again, limited the ability to characterize these samples. For this reason, the crystals were screened and recorded, but not studied further.

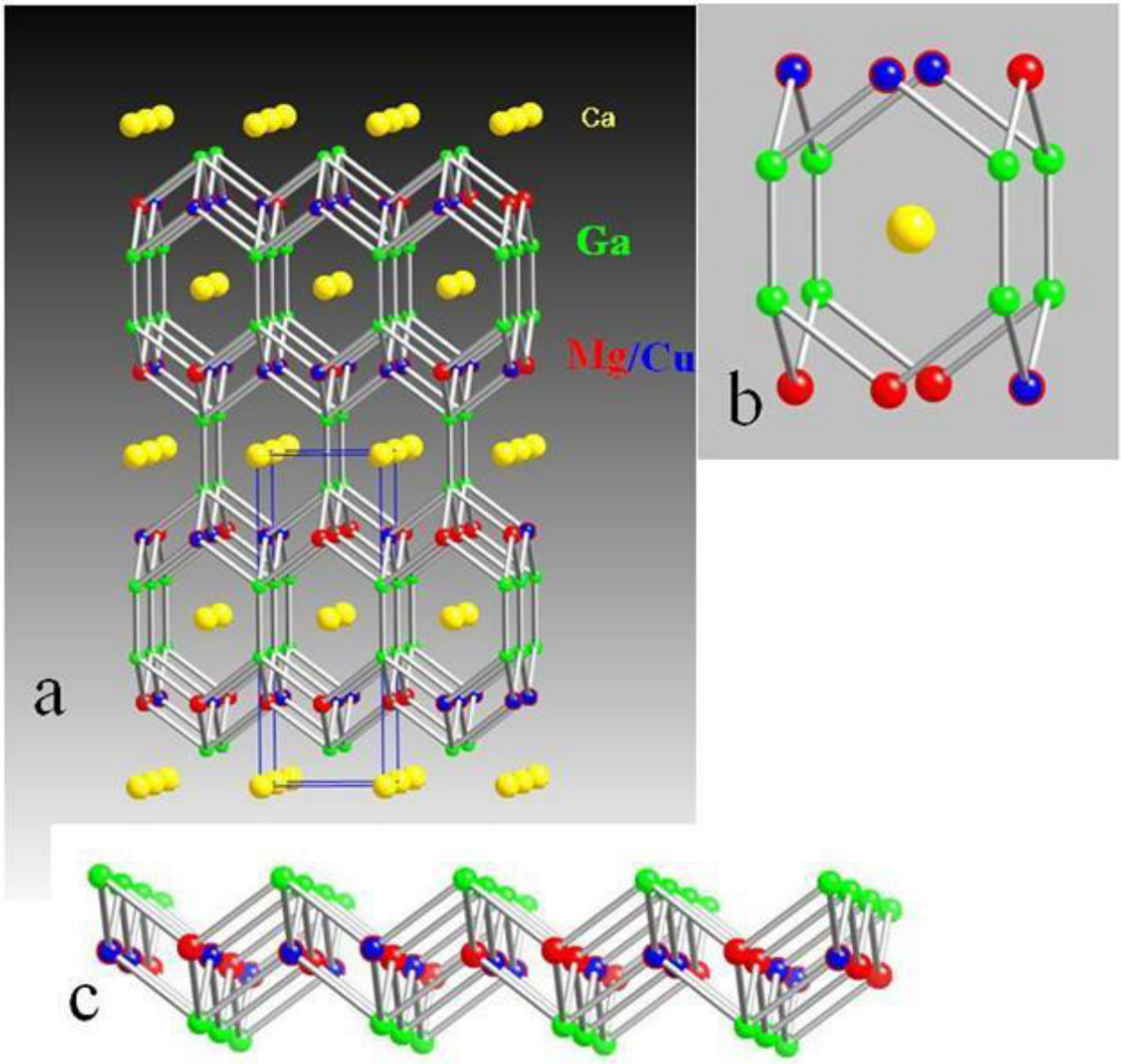

Figure 3.5 (a) The structure of $CaGa_2Mg_{1.86}Cu_{0.14}$ with the $ThCr_2Si_2$ structure type. (b) Local environment of calcium. (c) The Mg/Cu layer in the a-b plane.

Despite the Mg-Ga flux which was used, the compounds $CaGa_2$, $CaGa_4$ $CaZn_2$ and $CaZn_5$ (and substituted variants) were commonly observed in reactions that included Ca. They formed readily in the flux reactions and were stable even at high centrifugation temperatures. These products had a large phase width, exemplified by multiple reactions leading to products with the same structure type and differing levels of substituted elements. Al, Zn and Ga have a unique ability to substitute with ease in intermetallics of Ca. Two phases in particular were very stable through varying compositions of elements and shared the same $CeCu_2$ structure type; $Ca(Ga/Zn)_2$ (orthorhombic-I, *Imma* a=4.508 Å, b=7.758 Å , c=7.421 Å) and $Ca(Ga/Al)_2$ (orthorhombic-I, *Imma* a=4.538 Å , b=7.803 Å , c=7.437 Å). Error estimates and r value are not given because these samples were only initially screened. Multiple experiments led to these same compounds with simply varied substitution (confirmed by elemental analysis and single crystal X-ray occupancy refinements). It was immediately obvious that the substitution in these structures was difficult to control, and created uncertainties in results. A single ternary phase CuMg(Zn/Ga), (cubic-F *Fd*-3*m* a=7.1756 Å) was synthesized and initially screened, but like the binary phases previously shown, this phase had random substitution in the form of Zn/Ga substitution.

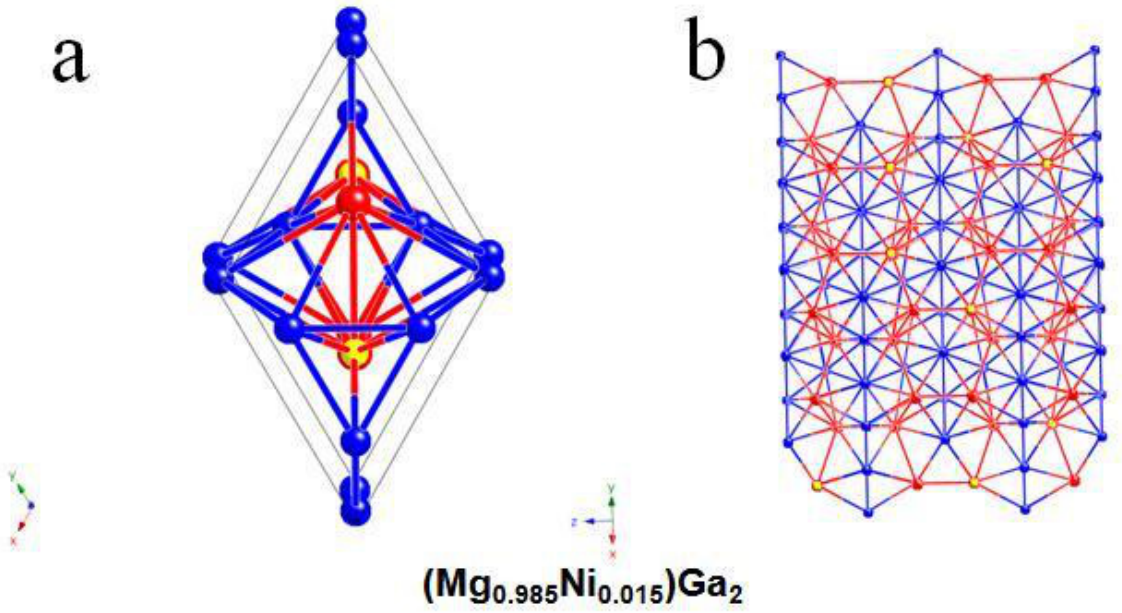

Figure 3.6 Unit cell (a) and expanded lattice (b) of $(Mg_{0.985}Ni_{0.015})Ga_2$.

Mg-X (X = Ni, Cu, Zn) Reactions with Lightweight and Inexpensive Reactants

Solubilities of B, C, Si, Ti, V, Cr, Mn, and Fe in liquid Mg are very low (<~1%) and this limits the reactivity and diffusion in Mg flux reactions involving these elements. These reactants are very appealing for synthesis of hydrogen storage materials due to their low cost and weight. Also, certain borides have superconducting properties (such as MgB_2 with T_c of 39 K), so there is great interest in isolating new boride phases. Unfortunately, it was impossible to use these elements in the Mg flux due to their low solubilities and high melting points. In order to increase the solubility of these reactants, mixed fluxes were explored that employed a flux of composition Mg-X (X = Ni, Cu, Zn) at ratios that varied according to 20 / (4-10) mmols and were put into welded stainless steel crucibles. The presence of the Ni, Cu or Zn can allow for solvation of the B, C, Si, Ti, V, Cr, Mn, and Fe. The use of Ni, Cu or Zn as a normal reactant did not have the same solvating power as the mixed Mg-X (X = Ni, Cu, Zn) flux. The concentration of the late transition metal must be high enough to significantly affect the environment inside the reaction vessel. Although many of these reactions have been run, the products remain in the crystal bank (detailed later in this dissertation) and have not been screened for structure, composition or properties as of yet.

Distillations

Vapor phase reactions were initially explored to attempt crystallization of intermetallics through co-deposition of two or more elements that had significant vapor pressure in a temperature gradient. Previous literature has shown that certain reactions can yield large single crystals of ionic compounds via vapor phase transport and deposition.[75] Investigations into vapor phase reactions to synthesize Mg-based intermetallics proved unsuccessful. However, vapor transport set-ups did prove useful in purifying flux grown products by allowing the distillation of excess Mg away from products. A standard distillation set-up is shown in Figure 3.7 and the locations of the expected materials are labeled. The setup utilizes a small tube furnace which can accommodate one end of a long sealed stainless steel tube (~9 inches)

containing the reaction or sample. One end of the tube is inserted into the furnace to create a hot source, while the other end of the tube is allowed to protrude from the furnace into room temperature air to create a cold sink. When the furnace was heated above 650 °C, excess Mg began to vaporize and was transported to the cold sink where it deposited as Mg dendrites. This setup could also be used to force a phase transition from the decomposition of a Mg-rich phase to a second phase containing less Mg.

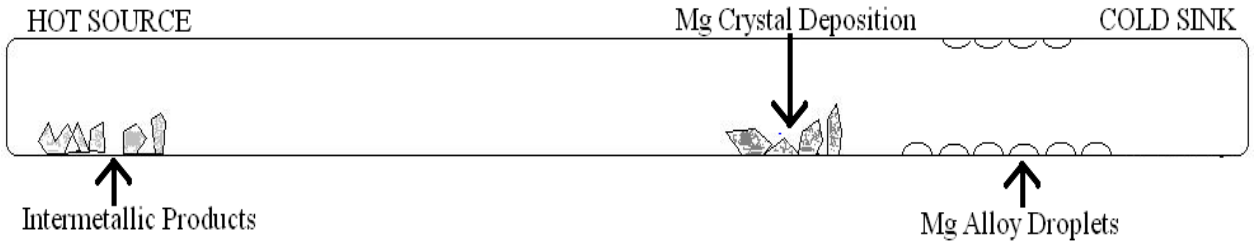

Figure 3.7 Diagram of thermal gradient tube set up for Mg distillations and relative locations of obtained products.

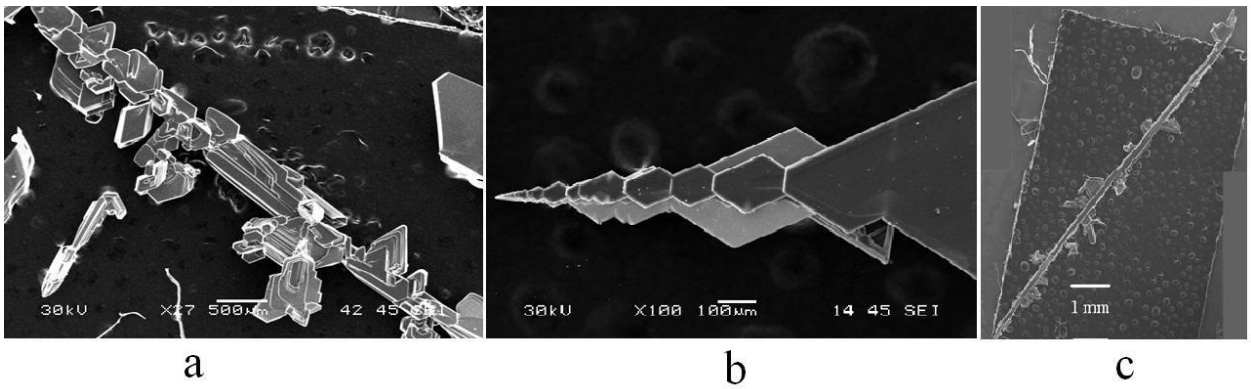

Figure 3.8 SEM images of Mg dendrites obtained from distillation experiments. (a) and (c) were obtained with vertical reaction tube orientation while (b) was obtained horizontally.

The distillation set-up was applicable to the treatment of certain Mg containing composite or polycrystalline products. For example, a mixed phase composite consisting of the Mg_6Ni phase within a pure Mg matrix could be distilled to remove a majority of the Mg matrix, leaving the Mg_6Ni phase as the major product and some residual Mg matrix.[76] The intermetallic product

was positioned in the hot sink of the setup and run in a desired heating process. Heating at 650 °C would produce significant distillation of the excess Mg in a product within a few hours. This was evident by the large dendritic crystals which would form at a "sweet spot" near the outlet of the tube furnace, and by the formation of Mg droplets in the far end of the cold sink. Figure 3.8 shows the intricate dendrites that form as a result of Mg vapors depositing as they migrated toward the cold sink of the distillation set-up. Figure 3.9 shows a Mg droplet which was formed in the extreme ends of a distillation set-up. SEM/EDS analysis of the droplets showed a varying Ni atomic concentration of 0-5%. Quantification of the Ni concentration dependant on temperature was difficult due to the inability to monitor the temperature inside the protruding end of the tube, but a correlation between Ni concentration and the location of the droplets was observed. Where the largest size and most number of droplets formed, the Ni concentration in the droplets was the highest. Despite some interest in furthering this aspect of the study, it was not pursued due to the uncertainties involved in temperature quantification.

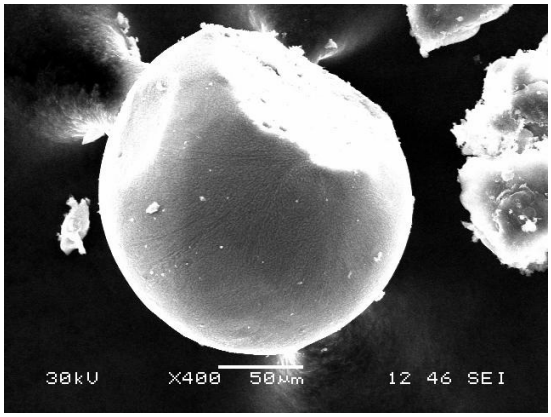

Figure 3.9 Mg droplet formed in cold sink of horizontal reaction tube.

Magnesium vapor crystallizes upon deposition with the common hexagonal form of elemental Mg in the $P6_3/mmc$ space group (#194) with unit cell parameters of a = 3.2094 Å, c = 5.2108 Å.[74] Due to the tube's orientation halfway outside the furnace, the Mg vapors are carried toward the cold sink and deposit, which occurred readily in a horizontal distillation set-up. The deposition occurs in the form of large, nearly perfect Mg crystals that propagate in the direction

of the hot sink. In attempts to maximize the size and length of these crystal dendrites, the distillation set up was rotated 90° to a vertical orientation. When the furnace and tubes were positioned vertically, as shown in Figure 3.10, the force of gravity acted against the temperature gradient and elongated the dendrites significantly. Modifications to the inside of the tube were made to observe the effects this would have on the dendrite propagation. In different experiments, tubes were crimped (to create ridges on the inside of wall of the tubing) and thin rods were inserted at the top of the tubes (to allow for dendrite growth on the rods). These modifications had a slight effect on the size and shape of the dendrites, but did not significantly change the morphology to validate further work.

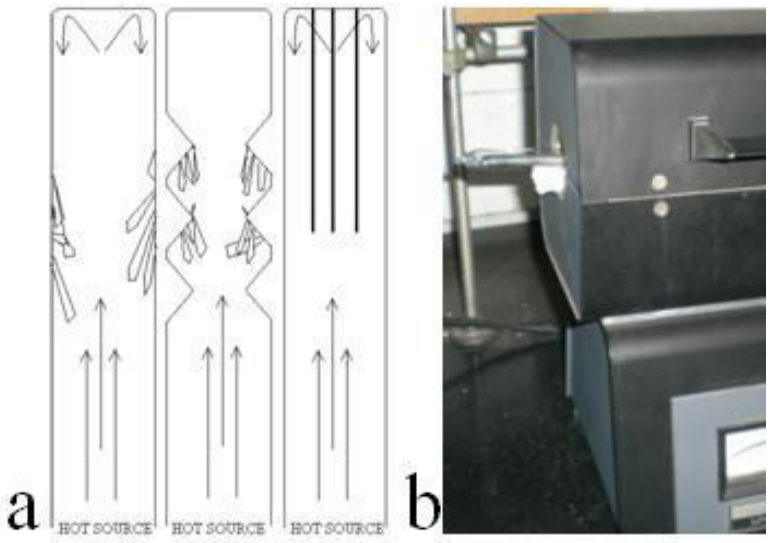

Figure 3.10 Vertical distillation variations (a) used to create better surfaces for Mg dendrite propagation and the standard horizontal setup (b) used for most distillations.

Although the use of the distillation set up had uses in growing dendrites and purifying products, there was little evidence to show that the dendritic crystals could be doped. Several metal halides were added ($NiBr_2$, $FeBr_2$, etc.), but this resulted only in the formation of large amounts of Mg halide crystals. The halides were put into the hot source end of the tube in several ratios, but the Mg halide crystals would form limited only by the amount of halide initially added to the tube. The Mg-halide crystals would form in a similar fashion to the Mg dendrites at a location in the tube near the outlet of the furnace. As a synthetic technique, there

were limitations to the distillation method that made it less appealing for exploratory synthesis than the use of a flux for reactions. Distillations remain a useful method of Mg removal from products which may be covered with Mg flux.

Ca-based Intermetallics

Ca fluxes were also of interest for synthesizing hydrogen storage materials because Ca is a very good "A" type hydride former (CaH_2, maximum hydrogen storage capacity of 4.8 weight percent) and can be used in a similar manner to Mg fluxes. The heavier weight of Ca does limit the maximum gravimetric hydrogen storage capacity of resulting Ca-based intermetallics. Unlike Mg, though, Ca does not have as high a vapor pressure and the resulting attack on the silica ampoules is not as pronounced. Reactions in pure Ca flux should not be carried out in alumina crucibles, as this will corrode the alumina material at high temperatures. Open stainless steel crucibles are suitable; Ca fluxes are far less likely to leach Fe, Ni or Cr impurities than Mg fluxes. Many of the products synthesized using Ca-based fluxes had large phase widths and could readily substitute similar elements in the structure.

Ca-Al Flux Reactions

The phase diagram for Ca-Al (Figure 3.11) shows two interesting eutectics with low melting points that can be used as solvents for flux reactions. Zn and Cu showed very high solubility and reactivity in the Ca-Al flux. The flux used for these reactions was composed of Al / Ca at a ratio of 3.5 / 6.5. Alumina crucibles can be used for this flux mixture. All products formed in either the orthorhombic $CaZn_2$ or hexagonal $CaAl_2$ structure types. Products were substituted binary phases that incorporated two or three elements onto one crystallographic site to form substituted compounds like $Ca(Zn/Al)_2$ and $Ca(Zn/Cu/Al)_2$. Depending on the starting reaction, product crystals contained Al, Ca, Zn and/or Cu. In a single reaction, the substitution levels of the crystals would vary from one single crystal to another. The uncertainties from the random substitution and the lack of control created characterization problems that stopped

further work with this system. No products incorporated any Mg, despite its inclusion as a low concentration reactant in some of the experiments.

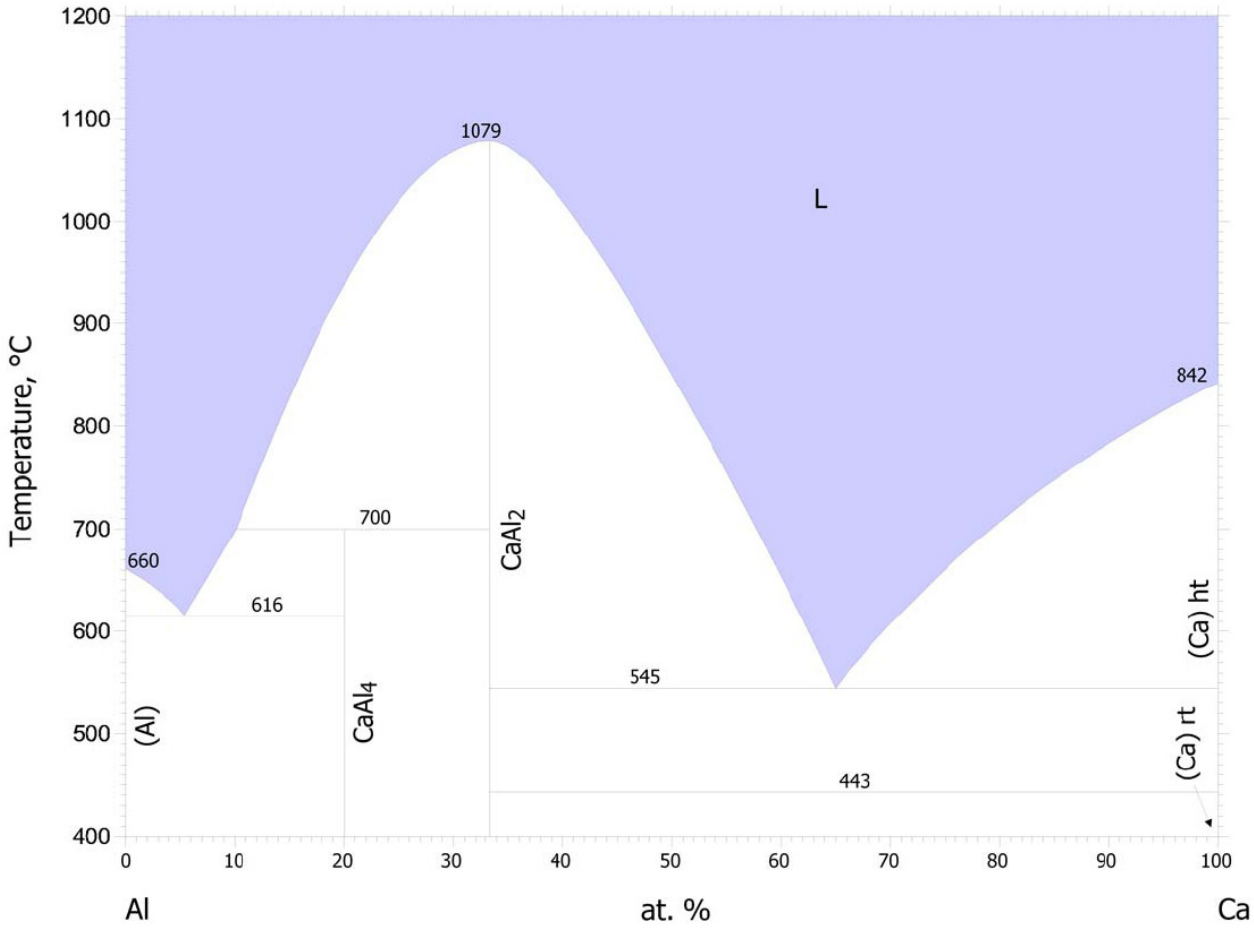

Figure 3.11 Phase diagram of the Al-Ca binary system.[30]

Controlled substitution in $CaGa_4$ grown from Ga/Zn flux In the case of the Ca / Ga / Zn flux reactions, good control of product crystal substitution levels was finally attained. Both Zn and Ga form stable compounds with Ca. By varying the starting reaction ratios for these experiments, a full series of reactions was created that varied the Ga / Zn ratio from the purely Ga containing phase, $CaGa_4$, to the purely Zn containing phase, $CaZn_5$. The compound $CaGa_4$ has a well known tetragonal structure ($BaAl_4$ type) with space group *I4/mmm* and unit cell parameters of a = b = 4.370 Å, c = 10.65 Å.[74] The crystals grown in this work had varying unit

cell parameters due to substitution, but retained this structure type until the Zn substitution became large enough that the hexagonal $CaZn_5$ structure type (*P6/mmm, a = b* = 5.3899 Å, *c* = 4.2456 Å[74]) was more stable.

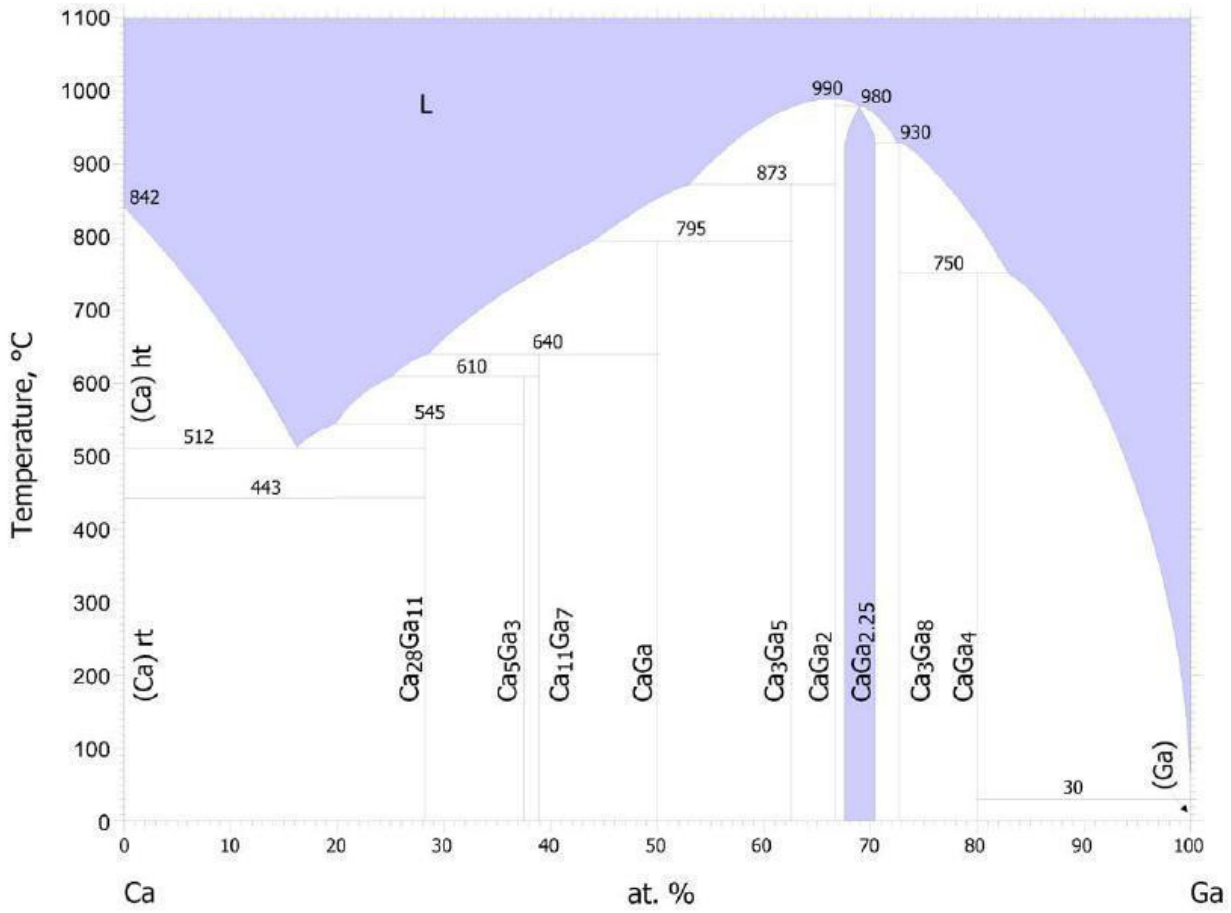

Figure 3.12 Phase diagram of the Ca-Ga binary system.[30]

Products were synthesized by combining the Ca / Ga / Zn in alumina crucibles with a steel filter. Table 3.4 shows how the starting reactions were varied in a systematic manner to create the series. The reaction vessels were heated to 950 °C in 5 hours then cooled to 650 °C in 50 hours, soaked at 650 °C for 20 hours then centrifuged. The use of a Ga and/or Zn rich flux facilitated the growth of the target crystals. Figures 3.12 and 3.13 show the phase diagrams for the Ca-Ga and Ca-Zn systems, respectively. Centrifugation at 650 °C ensures any liquid flux

will be removed and favors the formation of the target phases by using a 3 / (7-14) ratio of Ca / (Ga/Zn). The EDS values displayed in Table 3.4 confirm the $CaGa_4$ structure type and the switch to $CaZn_5$ from the more Zn-rich reactions. The atomic concentrations from the EDS are semi-quantitative, but serve as good estimates.

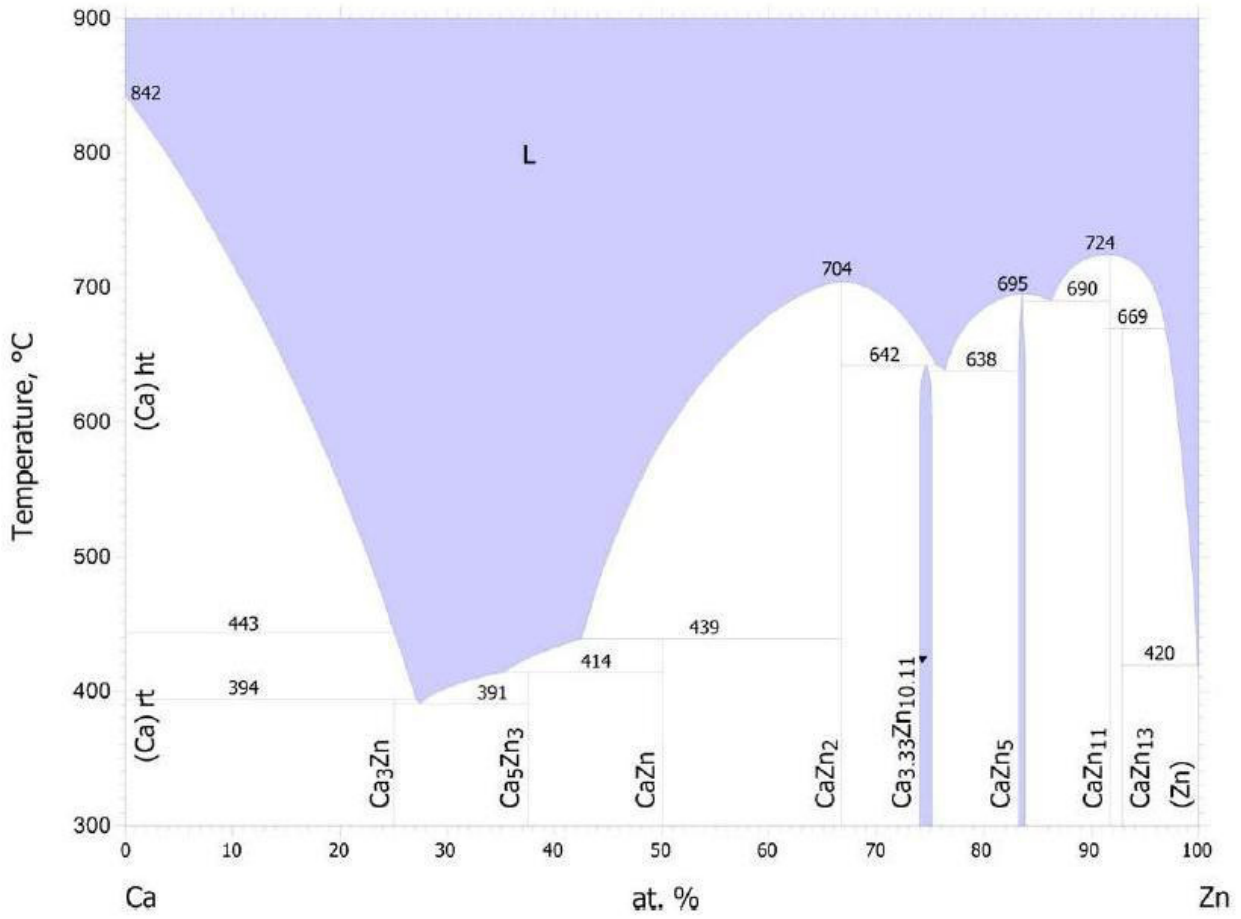

Figure 3.13 Phase diagram for the Ca-Zn binary system.[30]

The PXRD patterns for the varied reactions are shown in Figure 3.14. The $CaGa_4$ structure type was present until the Ga / Zn ratio is small enough to cause a shift to the $CaZn_5$ structure type. The $CaGa_4$ structure features substitution of Zn on the Ga site; this is evident in the PXRD data for the samples which show a shifting of the peaks in the pattern which indicates changing unit cell parameters. The peaks in the data are not marked, as these crystals were pure,

single phase and all peaks correspond to the $CaGa_4$ (*I*4/*mmm*) structure type. The PXRD data shows that in the mix 10 through mix 13 reactions the structure type changes drastically. These new peaks correspond to the $CaZn_5$ structure type and this represents the limit of substitution that can occur into $CaGa_4$ until the $CaZn_5$ structure type becomes a more stable option for arrangement of the atoms in the flux.

Table 3.4 Starting reaction ratios and corresponding EDS values for $Ca(Ga/Zn)_{4-5}$ products.

Reaction Name	**Ca / Ga / Zn Ratio**	**Calcium (at %)**	**Gallium (at %)**	**Zinc (at %)**
Mix 1	3 / 7 / 0	24	76	0
Mix 2	3 / 7 / 0.5	24	73	3
Mix 3	3 / 7 / 1	24	69	7
Mix 4	3 / 7 / 2	24	62	15
Mix 5	3 / 7 / 3	24	57	19
Mix 6	3 / 7 / 5	23	49	27
Mix 7	3 / 7 / 7	22	50	27
Mix 8	3 / 5 / 7	24	44	33
Mix 9	3 / 3 / 7	24	40	35
Mix 10	3 / 2 / 7	25	28	46
Mix 11	3 / 1 / 7	25	31	43
Mix 12	3 / 0.5 / 7	14	0	86
Mix 13	3 / 0 / 7	13	0	87

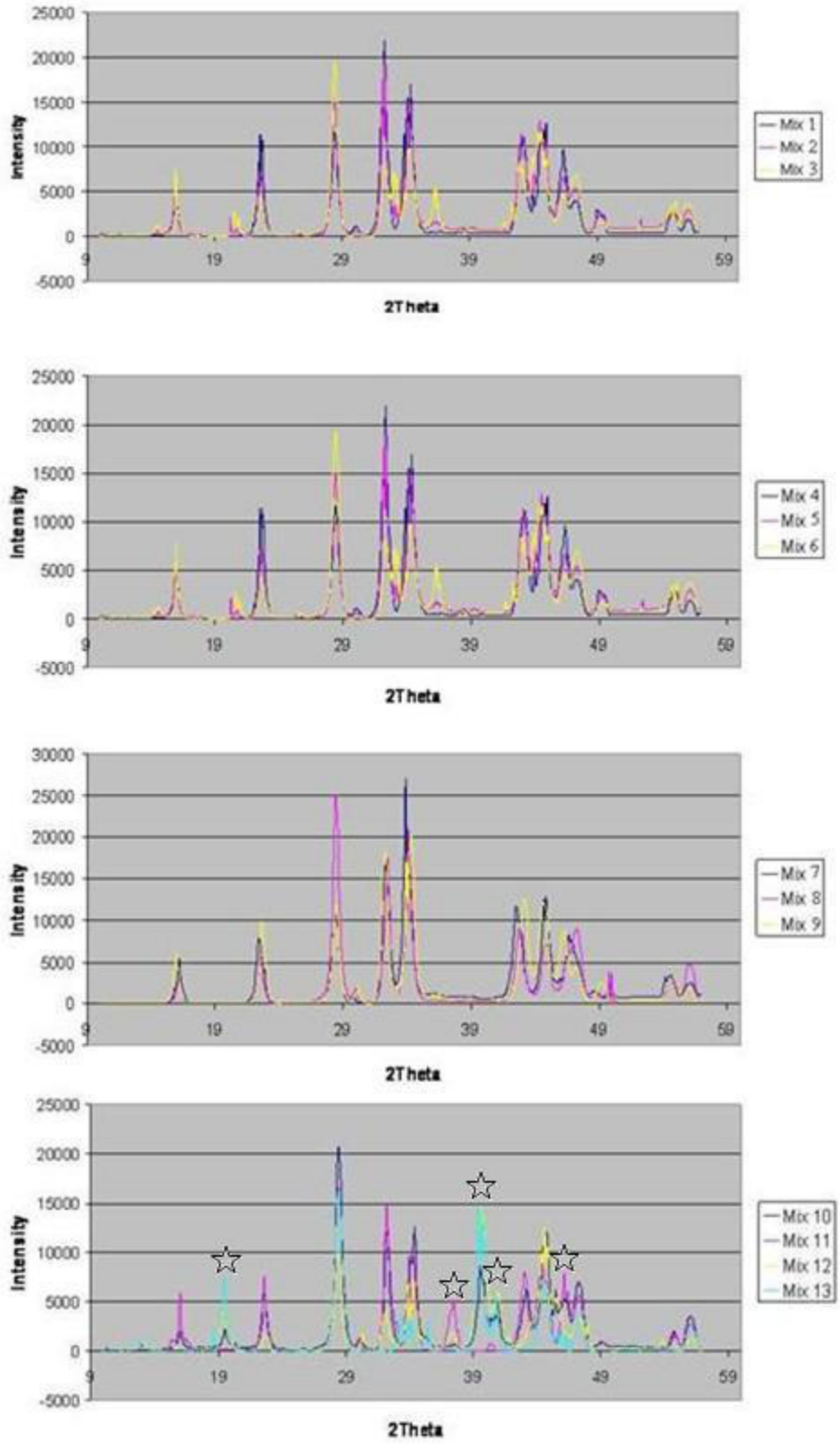

Figure 3.14 Powder XRD patterns for $Ca(Ga/Zn)_4$ products. The Zn-rich reactions caused a change in structure type to the hexagonal $CaZn_5$ structure (marked by stars).

As the unit cell was changing with substitution of Ga for Zn in $CaGa_4$ structure, a trend was observed most noticeably in the c-axis lattice parameter. Figure 3.15 displays the c-axis parameter vs. the percent of Ga. This change in unit cell size was subtle, but as the ratio of Zn increases, so does the size of the unit cell. This is expected as the size of Zn is slightly larger than Ga; the atomic radii Zn and Ga atoms are 1.35 Å and 1.30 Å, respectively.[5] There are some large deviations from linearity in the data and this can be attributed to the synthesis methods which did not have absolute control of substitution.

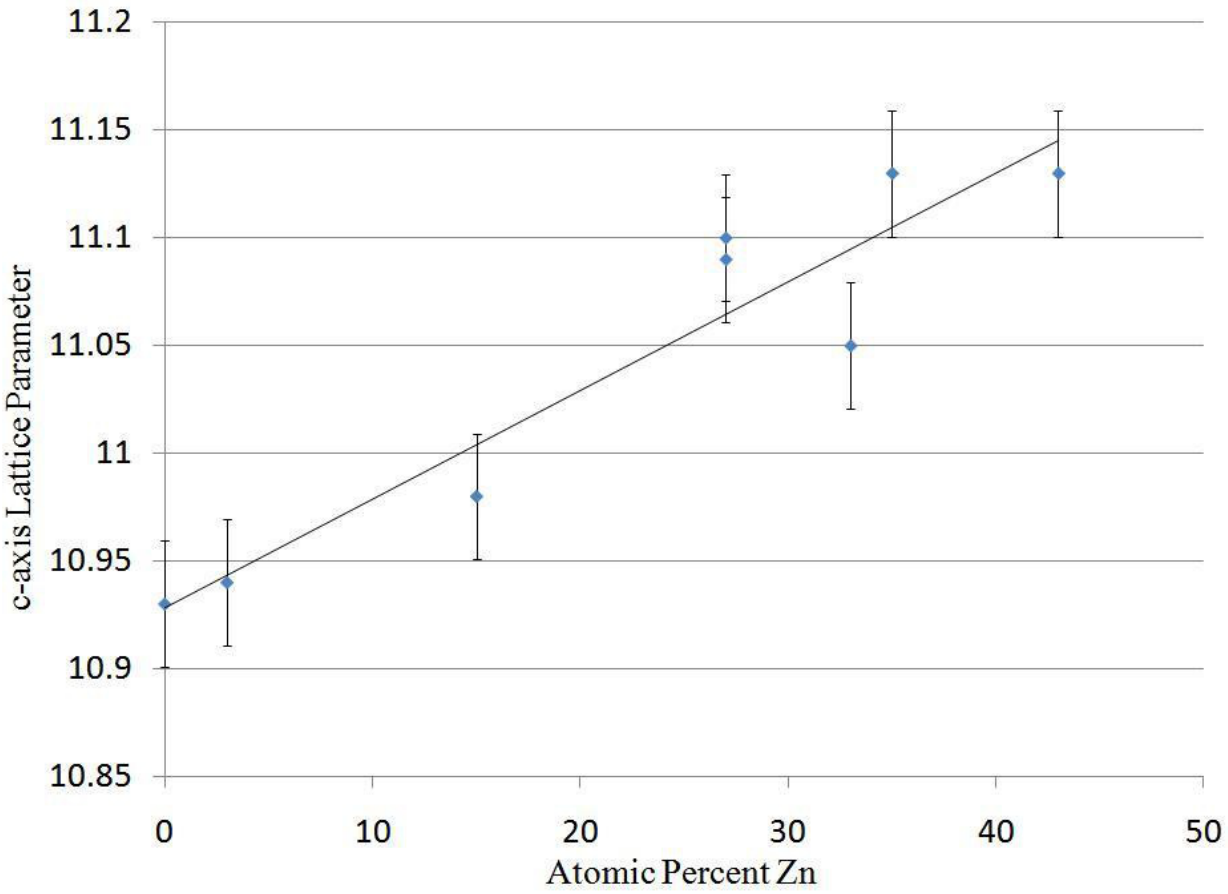

Figure 3.15 Unit cell dependence on substitution amount of Zn in $Ca(Ga/Zn)_4$.

The large concentration of Zn which can be introduced into the $CaGa_4$ structure shows the lattice was very stable before it was forced to switch to the $CaZn_5$ structure. Even at a starting reaction ratio for Ca / Ga / Zn of 3 / 1 / 7, the $CaZn_5$ structure was not formed, but

instead a highly substituted version $CaGa_{1.68}Zn_{2.32}$ was observed. Only when there was no Ga present in the reaction did the $CaZn_5$ structure form. This was due to the strong bonding interactions of Ca and Ga which dominated in the flux over the Ca-Zn or Ga-Zn interactions. No Ga incorporation is seen in the $CaZn_5$ structure. Due to the heavy weight of Ga and Zn, the hydrogen storage will be very limited in these compounds. After exploring the control of substitution through varying starting reactions, these compounds were not investigated any further.

CHAPTER 4

SYNTHESIS, CHARACTERIZATION AND HYDROGEN DESORPTION FROM ALKALINE EARTH SILICIDE COMPOSITES

Introduction

This study investigated the synthesis, structural characterization and gravimetric hydrogen desorption measurements of a Mg-based melt composite formed from a 2 / 1 / 1 mmol ratio of Mg / Ca / Si. The effect of transition metals was explored by making identical measurements on melt composites of 2 / 1 / 1 / 2 mmol equivalent mixtures of Mg / Ca / Si / M (M = Fe or Co). The elements present in these mixtures were chosen on the basis that Mg and Ca are A type elements, while Fe and Co are B type elements. Fe and Co are relatively lightweight transition metals which makes them more attractive for incorporation into hydrogen storage materials compared to more expensive and heavy transition metals such as Pt or Pd. Fe is a non-hydride forming element and no stable Mg-Fe phase is known, although the stable Mg_2FeH_6 phase shows a high volumetric hydrogen density of 150 kgH_2/m^3.[83] Mg and Co form the Laves phase compound $MgCo_2$ which has the hexagonal C14 structure type and forms the stable Mg-Co hydrides, Mg_2CoH_5 and $Mg_6Co_2H_{11}$.[84] Since Si is a non-metal, it does not fall into the A or B category, but it affects the structure and other physical characteristics of the product materials, including their hydrogen storage properties. Both A and B type elements were combined in order to create an environment for absorbed hydrogen atoms which allows them to be coordinated to both A (hydrogen absorbing) and B (non hydrogen absorbing) atoms. This may help avoid final products susceptible to disproportionation reactions from a high A/B ratio or to negligible hydrogen absorption due to a low A/B ratio.[16]

Instead of isolation and study of a pure compound, this work involved the synthesis of composites. In general, a composite is a material comprised of two or more different components that have been incorporated and are held together by non-intermolecular forces (no bonding). In other words, these materials are made from two or more different phases and the distribution of these phases in controlled by mechanical means rather than only by heat treatment.[71] Composites of Mg offer some interesting possibilities for the creation of materials with unique properties because composites exist without destroying the structure or properties of the components in the composite. Due to the negligible solubility of B, C, N and early 3d transition metals, composites offer a route toward materials development that does not rely on a reaction between Mg and these elements. Instead, the Mg encapsulates and completely covers the other components. Certain composite compositions can reduce the susceptibility of a material to undergo a disproportionation reaction. Inherently though, composites usually take on the general properties of the host matrix. In the case of Mg and its application to hydrogen storage, this is a glaring problem because of the undesirably high desorption temperature (>400 °C) and large, negative enthalpy of formation (ΔH = -75 kJ/mol) for the hydride phase.[72,73]

Experimental Procedure

Synthesis

Products were synthesized using Mg metal slugs (3.175mm x 3.175mm, 99.95%), Ca shot (1cm and down, 99.5%) and Co powder (-100+325 mesh, 99.8%) from Alfa Aesar. Fe powder (99+%) and Si powder (99+%) were from Strem Chemicals. For the synthesis of the ternary control product, the reactants were combined in 20/10/10 mmol ratio (0.486g Mg, 0.401g Ca, and 0.281g Si, respectively). To synthesize the transition metal containing products, 1.179g of Co or 1.117g of Fe was added to the above reaction (for Mg / Ca / Si / M (M=Fe, Co) mmol ratio of 20 / 10 / 10 / 20). A stoichiometric synthesis of Ca_2Mg_3Si was also attempted using masses of 0.365 g, 0.401 g and 0.140 g, respectively. Pure elements were handled in air, at room temperature, during the weighing process.

The above reaction mixtures were loaded under argon into crucibles made from 3/8" OD niobium tubing. The open end of the crucibles were then welded shut, yielding gas tight reaction vessels sealed under ~1 atm Ar. The reaction vessels were put into silica tubes, evacuated on a vacuum line and sealed. Before being placed into a furnace, each reaction vessel was gently shaken several times to aid in diffusion and mixing. The reactions were heated from room temperature to 950 ºC in 5 hours, held at 950 ºC for 10 hours, cooled to 600 ºC in 1 hour, and held at 600 ºC for 1 hour at which point the reaction tubes were inverted in the furnace to further mix the contents. The reactions were heated again to 950 ºC in 1 hour, held at 950 ºC for 10 hours, and cooled to room temperature in 5 hours.

Hydrogenation

The tubes were cut open in a glove box and the products removed from the crucible under argon. For each reaction, two small portions of raw product (~0.1 g) were separated; one for single crystal XRD was left in its ingot state, the other, for powder XRD, was hand ground using an alumina mortar and pestle for ~5 minutes. The rest of the bulk raw product was prepared for hydriding by ball milling in a Spex SamplePrep Spex5000 installed in the drybox. Products are milled for 1 hour with a ball to powder mass ratio of 5:1. Hydrogenation of all products was conducted on a previously described system (Chapter 2). 0.5 g amounts were used for hydrogenation studies. The products were activated by heating for 1 hour at 400 ºC under dynamic vacuum and were then allowed to cool to room temperature. The hydrogenation was carried out by pressurizing to 13.6 atm H_2 in the sample chamber of the apparatus, then heating at 400 ºC for 1 hour under pressure; the product was allowed to cool and the sample chamber pressure was lowered to ~1 atm H_2. All products were subjected to both the activation and hydrogenation steps, and were then stored in the drybox.

Elemental and Thermal Analysis

Bulk composites and pre-selected single crystals were mounted on Al pucks with carbon tape inside the drybox. Elemental compositions were assessed using a JEOL 5900 scanning electron microscope equipped with PGT Prism energy dispersion spectroscopy software.

Ca_2Mg_3Si crystals separated from the bulk composite contained (atomic percents) Mg[43(4)], Ca[36(2)], Si[20(4)]. The Fe containing composite had an average of Mg[45(4)], Ca[23(3)], Si[13(4)], Fe[18(5)]; while the Co containing composite had an average of Mg[40(5)], Ca[22(3)], Si[11(5)], Co[28(5)]. There were no impurities above 0.5 atomic percent detected. Elemental composition homogeneity was observed for all samples before and after hydrogenation. Hydrogen desorption properties were quantified using simultaneous differential scanning calorimetry and thermogravimetric analysis (DSC/TGA) on a TA Instruments SDT 2960 Simultaneous DSC-TGA. MgH_2 from Alfa Aesar was used in DSC/TGA measurements as a standard hydride comparison.

Structural Studies

Powder X-ray diffraction studies were carried out using a Rigaku Ultima III (Cu source) diffractometer equipped with a CCD detector. Products were mixed with a Si internal standard. Powder patterns were collected under ambient atmosphere, temperature and pressure using this method. Oxide formation was observed on the surface of the material after continued exposure to air, so these products were not used for subsequent studies.

Single crystal and powder X-ray diffraction data were collected under nitrogen on a Bruker APEX2 single crystal X-ray diffractometer (Mo source) to avoid oxidation of products. For collection of powder diffraction data from ball milled products on the single crystal diffractometer, a slurry was created by mixing the product powder with a small amount of Si internal standard into paratone oil inside a dry box under argon. A small amount of the slurry was loaded into a 0.2 um cryoloop and then hardened at 200 K in the N_2 stream on the diffractometer. Data for the ball milled powder products was collected using a custom experimental strategy of Phi scans with conditions of 15.0 cm detector distance and 180 second exposure time. XRD^2 Pilot software integrated the diffraction rings into powder patterns, and MDI Jade software was used for background correction and peak identification.

Single crystals from the raw products were obtained by fracturing shards from the bulk ingot. These products were loaded into 0.2 um cryoloops using paratone oil, which was then hardened at 200 K. After collecting and indexing a small number of reflections to determine crystallinity, a full sphere of data was collected under flowing nitrogen. The data was integrated

by SAINT, and structural refinements were carried out by XPREP and SHELXTL.[85,86] During refinement, occupancies were allowed to vary independently, but each atomic position was fully occupied. Crystallographic data and collection parameters are shown in Table 4.1.

Results and Discussion

Synthesis of Mg-based intermetallics is often complicated by the volatility and corrosiveness of elemental Mg. Use of welded niobium reaction vessels allows for the containment of the Mg vapors enabling the Mg to react to form intermetallics. Mg forms stable compounds with both Si and Ca. Mg_2Si has the cubic C14 Laves phase structure (*Fm3m* (#225), a = 6.35 Å)[74]; this is the most well known stable binary phase of exclusively Mg and Si. Mg_5Si_6 and $Mg_6Si_{3.3}$ are lesser known phases.[87] The Mg_2Si structure was readily formed in this synthesis when the proper ratio of Mg / Si (2 / 1) was attained in isolated regions of inadequately mixed melts. The inclusion of Ca in the reaction hinders the formation of Mg_2Si by consuming elemental Mg to form Mg_2Ca. Mg_2Ca has the $MgZn_2$ structure type ($P6_3/mmc$ (#194) a = 6.225 Å, c = 10.81 Å).[74] This creates a competitive situation for the formation of the two differently structured compounds, Mg_2Si and Mg_2Ca.

Table 4.1 Crystallographic data and collection parameters for Ca_2Mg_3Si.

	Ca_2Mg_3Si at 298 K
Space group	$P6_3/mmc$ (no. 194)
Cell parameters, Å	$a = b$ = 6.0650(15) c = 9.747(3)
V, Å^3	310.50(14)
Wyckoff Site and Atom Positions	4*f* Ca (1/3, 2/3, 0.5622(3)) 2*a* Si (0, 1, 0) 6*h* Mg (0.1686(5), 0.3372(11), 1/4)
Z	2
Density (calc.), g cm^{-3}	1.938
μ, mm^{-1}	2.18

Table 4.1 Continued	
Data collection range, deg.	$3.88 < \theta < 19.04$
Reflections collected	1113
Independent reflections	66 [$R_{int} = 0.1128$]
Parameters refined	11
R_1[a)], wR_2 [b)] [$F_o > 4\sigma F_o$]	0.0219, 0.0424
R_1, wR_2 (all data)	0.0453, 0.0463
Largest diff. peak and hole [e/Å^3]	0.238 and -0.156
Goodness-of-fit	1.074

a) $R_1 = \Sigma \| F_o | - | F_c \| / \Sigma | F_o \|$.
b) $wR_2 = [\Sigma w(F_o^2 - F_c^2)^2 / \Sigma w(F_o^2)^2]^{1/2}$, $w = [\sigma^2(F_o^2) + (A \cdot p)^2 + B \cdot p]^{-1}$; $p = (F_o^2 + 2F_c^2)/3$; A = 0.0067, B = 0.

The only known and accepted ternary phases of Mg-Si-Ca are the compounds CaMgSi, with Co_2Si structure type (see Chapter 5; orthorhombic space group *Pnma* (#62) $a = 7.48$ Å , $b = 4.40$ Å , $c = 8.29$ Å) and $Ca_7Mg_{6-7.25}Si_{14}$ (*P6/mmm* $a = 12.696$ Å, $c = 4.4025$ Å), the latter is a more accurate formula of the phase $MgSi_3Ca_2$.[74,87,88] The existence of a third phase, Ca_2Mg_3Si, has been controversial, with some authors reporting the phase as a small fraction of a Mg-Ca-Si mixture and others reporting the phase as impossible to reproduce.[89-91] The formation of Ca_2Mg_3Si depends on forcing substitution of Si on the Mg site in Mg_2Ca; a range of stoichiometries $Ca_2Mg_{4-x}Si_x$ is seen, up to x = 1. This can be accomplished by including at least one molar equivalent excess Si in high temperature reactions containing stoichiometric amounts of Mg and Ca targeting Ca_2Mg_3Si. The Ca_2Mg_3Si system does have a large phase width (can be written as $Ca_2Mg_{4-x}Si_x$), and isolation of the fully substituted product proved difficult. Stoichiometric melts formed multi-phase composites of Mg_2Si, Mg_2Ca, Ca_2Si and $Ca_2Mg_{4-x}Si_x$ instead of a single phase product containing only the target phase. Reactions without excess Si will form a region-dependant composite of Mg_2Ca, Mg_2Si and CaMgSi with only a small fraction of Ca_2Mg_3Si occurring at grain boundaries between phases. Whether the resulting matrix is primarily Mg_2Ca or as Mg_2Si (in reactions containing excess Si) depends on the stoichiometry and competition between the different hexagonal or cubic structures, respectively. In the ternary reaction studied here, the competition occurring between the Mg_2Ca and Mg_2Si phases was resolved by formation of a Mg-based composite comprised of a main phase,

Ca_2Mg_3Si, which has the Mg_2Ca structure type with preferential 2*a* site substitution of Mg by Si, and a minor phase of Mg_2Si with the remaining Si.

PXRD could not distinguish between the very similar unit cells of isostructural Ca_2Mg_3Si and Mg_2Ca. However, SCXRD was able to solve multiple crystal structures to r values less than 0.05 from multiple batches of reactions, all having the selective site substitution of Mg by Si in the target phase, Ca_2Mg_3Si. The reactions not containing excess Si did not form substantial amounts of the target phase, and instead the substitution of Si into Mg_2Ca was superseded by the formation of CaMgSi. For reactions containing less than 17 molar % Si, the $Ca_2Mg_{4-x}Si_x$ structure was substituted with small amounts Si on the *2a* site and a single phase product was obtained. When excess Si was included in the reaction, product formation was the fully substituted Ca_2Mg_3Si phase, but this was present along with CaMgSi.

The Mg-Ca phase diagram shows the Mg_2Ca phase melting at 710 ºC which is below the highest point of the temperature program. The Mg / Ca mmol ratio (2 / 1) used in these reactions produced a melt which is perfectly proportioned to crystallize as Mg_2Ca. In contrast, a Mg / Si mmol ratio (2 / 1) was also used in the reaction and this corresponds to a point along the solidus line of the Mg-Si phase diagram at ~1100 ºC, which is outside the highest point of the temperature program. Likewise, at the reacted ratio of 1 / 1, the Ca-Si phase diagram shows the formation of CaSi occurs only above 1315 ºC.[30] Therefore, the only full melt achieved was in the Mg-Ca system. The control product, Ca_2Mg_3Si, was a result of the completely liquid Mg-Ca melt formation and the good diffusion and reactivity of Si in the melt.

The addition of Co to the mixtures resulted in the formation of a highly substituted analog major phase, $Ca_2Mg_{3-y}Co_ySi$, with the minor phase Mg_2Co also formed. When Fe was added to the mixtures, the major phase formed was Fe_3Si, with smaller yields of Mg_2Si and $Ca_2Mg_{3-y}Fe_ySi$. Due to the random substitution of the transition metals in $Ca_2Mg_{3-y}Co_ySi$ and $Ca_2Mg_{3-y}Fe_ySi$ the stoichiometry of the products varies for each reaction. Also, due to the low solubility and relatively high mass of elemental Fe and Co, some metal remains un-reacted on the bottom of the niobium crucible, which accounts for the low concentration of Fe and Co metal (approximately less than 5%) in the resulting composite products.

Structural Characteristics

The Mg / Ca / Si control reaction (with no transition metal added) yielded Ca_2Mg_3Si in both powder and single crystal form. Single crystal XRD data indicated the expected Mg_2Ca structure with space group $P6_3/mmc$ a = 6.065(1) Å, c = 9.747(3) Å.[74] The unit cell dimensions of the control product were slightly smaller than those associated with pure Mg_2Ca (a = 6.225 Å, c = 10.18 Å)[74] due to the substitution of smaller Si atoms which led to a shrinking of the dimensions by shortening of the Si-Mg and Si-Ca bonds. The structure of Ca_2Mg_3Si is shown in Figure 4.1 and Table 4.2 is a comparison of related structures. This layered structure features kagome nets of Mg alternating with slabs of Ca-Si in the a-b plane.

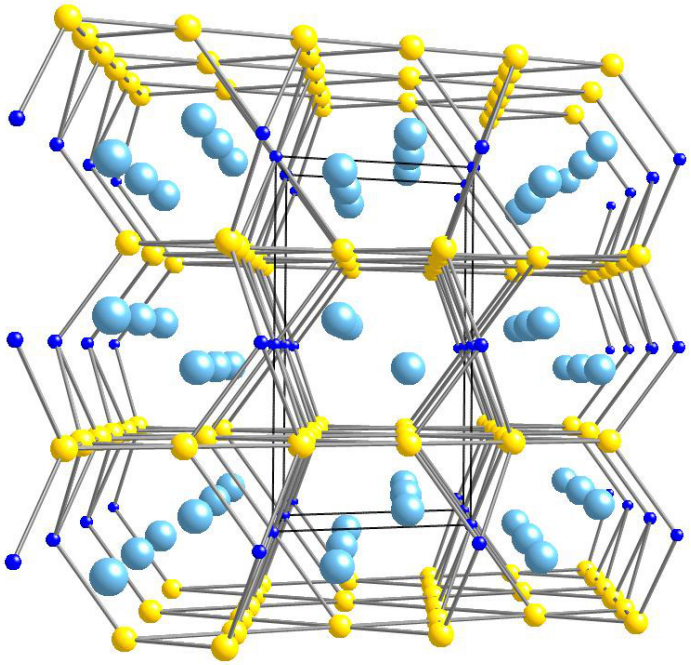

Figure 4.1 The structure of Ca_2Mg_3Si, viewed down the b-axis with unit cell outlined in black. Bonds are drawn between magnesium (yellow atoms) and silicon (small blue atoms).

The local Si (2*a* site), Mg (6*h* site) and Ca (4*f* site) environments are shown in Figure 4.2. Preferential substitution of silicon for magnesium on the 2*a* site is observed, and is likely promoted by the short bond lengths from this site to neighboring Mg atoms in the *6h* sites.

Occupation of the 2*a* site also allows the relatively electronegative Si atom to interact more closely with both Mg and Ca with a higher level of coordination to these electropositive neighboring atoms, while the 6*h* site is not situated to allow comparable coordination. Mg fully occupies the 6*h* site and has a Mg-Mg bond length of ~3.07 Å, which is shorter than the normal Mg-Mg bond in Mg_2Ca by ~0.04 Å. Because of the much larger radius of Ca atoms with respect to Mg or Si atoms, the 4*f* site is fully occupied by Ca and has no substitution in this system. Any sporatic random substitutions for Ca by Mg could improve the hydrogen storage properties of the product material slightly (as is seen in studies of CaSi vs. $Ca_{0.5}Mg_{0.5}Si$), but was not observed.[92]

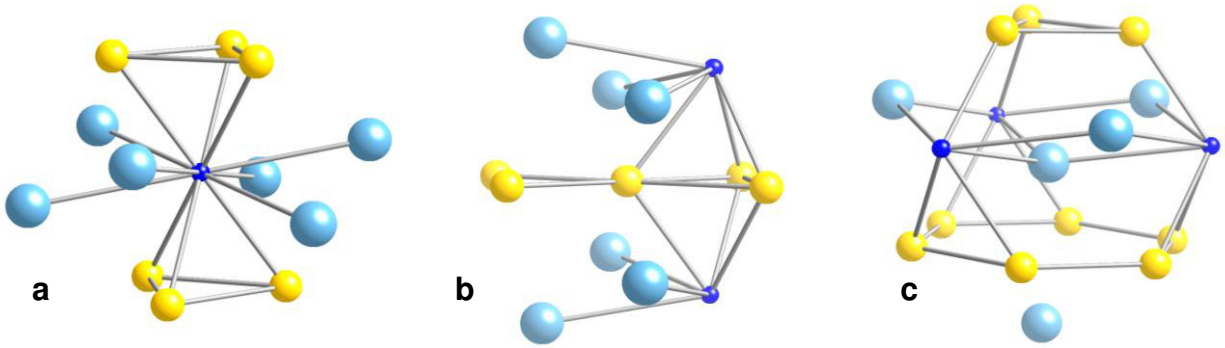

Figure 4.2 The local coordination environments of a) Si (*2a* site), b) Mg (*6h* site) and c) Ca (*4f* site).

The addition of Co to the reaction mixtures results in the formation of the same structure as the control product, Ca_2Mg_3Si, with substitution of Co into the Mg *6h* crystal site to yield $Ca_2Mg_{3-y}Co_ySi$ with $1 < y < 2$. In the Fe containing reaction mixtures, most of the iron is consumed in the formation of Fe_3Si, with $Ca_2Mg_{3-y}Fe_ySi$ present in smaller amounts in the product. The Co containing product had a more metallic luster, while the Fe containing product was duller with little shine. Mg_2Si was easily identified in products by its characteristic metallic blue shine and formed in isolated extremity regions of the reaction vessels. If the reaction time was shortened or the reaction vessels not flipped mid-reaction, Si was not incorporated into the Mg_2Ca matrix and instead, predominant regions of isolated Mg_2Si and small ingots of Mg_2Ca formed with unreacted Ca, Mg and transition metal present in the final material. Although there

are several stable phases in the binary systems Co-Si, Ca-Si and Fe-Si, these were not observed in the products, with the exception of Fe_3Si in the iron containing products.

Table 4.2 Cell parameters and bond distances of the reference and product materials.

	Mg_2Si [14]	**CaSi [17]**	**Mg_2Ca [14]**	**Ca_2Mg_3Si**	**$Ca_2Mg_{3-y}Co_ySi$**
a	6.35(1)	4.545(3)	6.225(1)	6.06(15)	6.252(3)
b	6.35(1)	10.728(10)	6.225(1)	6.06(15)	6.252(3)
c	6.35(1)	3.890(3)	10.180(1)	9.74(28)	10.135(7)
V	256.10	175.57	343.45	310.50	343.09
Mg-Si	2.75	-	-	3.01	3.12
Mg-Ca	-	-	3.66	3.54	3.63
Mg-Mg	3.17	-	3.13	3.07	3.12
Ca-Si	-	3.00	-	3.55	3.66
Ca-Ca	-	3.48	3.82	3.66	3.31

Preparation for Hydriding

Ball milling was carried out on the samples to increase the reactive surface area of the product material; this has been shown to lower the desorption temperature and absorption pressure of the hydride phase.[93] The ball milling program for the raw samples produced a uniform powder of particles less than 50 um. To ensure the product structures were retained during the ball milling treatment, hand ground product was analyzed in comparison to ball milled product using powder X-ray diffraction. Figure 4.3 shows the XRD data for ball milled (blue) and hand ground (red) Co-containing product. At the conditions used in this work, the heat and mechanical deformation associated with high intensity ball milling is not sufficient to create additional phases or destroy existing phases in the products during the treatement. The peaks corresponding to the Mg_2Ca structure phase became wider, showing a reduction in particle size, but no new peaks appeared/disappeared in the patterns before and after ball milling and this trend was consistent for the control, Co-containing and Fe-containing products.

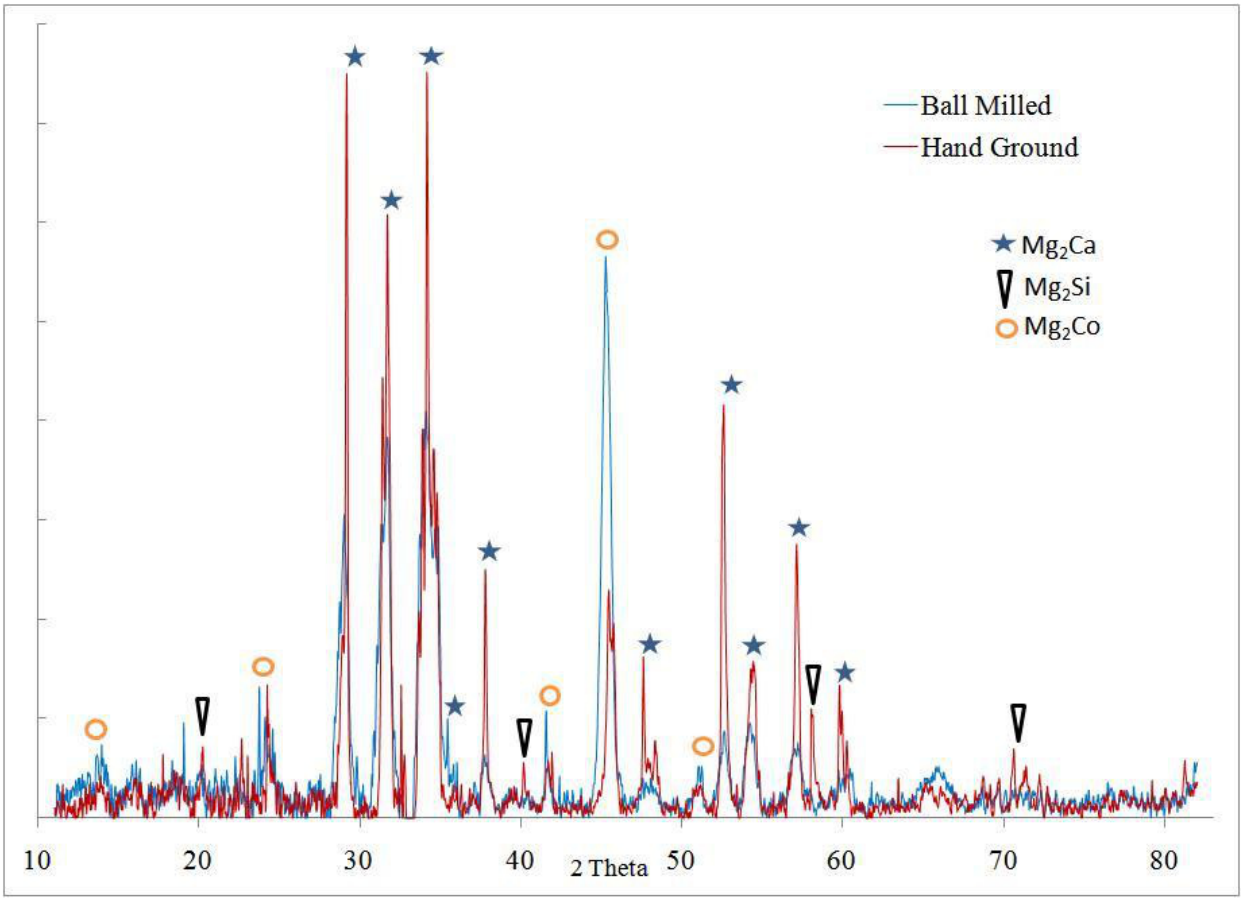

Figure 4.3 Powder XRD of samples of $Ca_2Mg_{3-y}Co_ySi$ with $1 < y < 2$, comparing hand grinding to ball milling. The milling process does not degrade the structure.

Hydriding Process

SEM images of compounds before and after hydrogenation are shown in Figure 4.4. All products were homogeneous powders with consistent particle sizes. Upon hydrogenation, the products gained a more sharp edged appearance, were less aggregated and turned darker black in color despite the low hydrogenation pressure. The SEM images show that the product morphology and particle size are retained through the hydrogenation process. A disproportionation reaction was not observed to occur upon hydrogenation, which would have been evident in the SEM images as a change in the physical appearance of the products. These images indicate the likelihood that the products can reversibly store hydrogen within the interstitial sites of the crystal lattice.

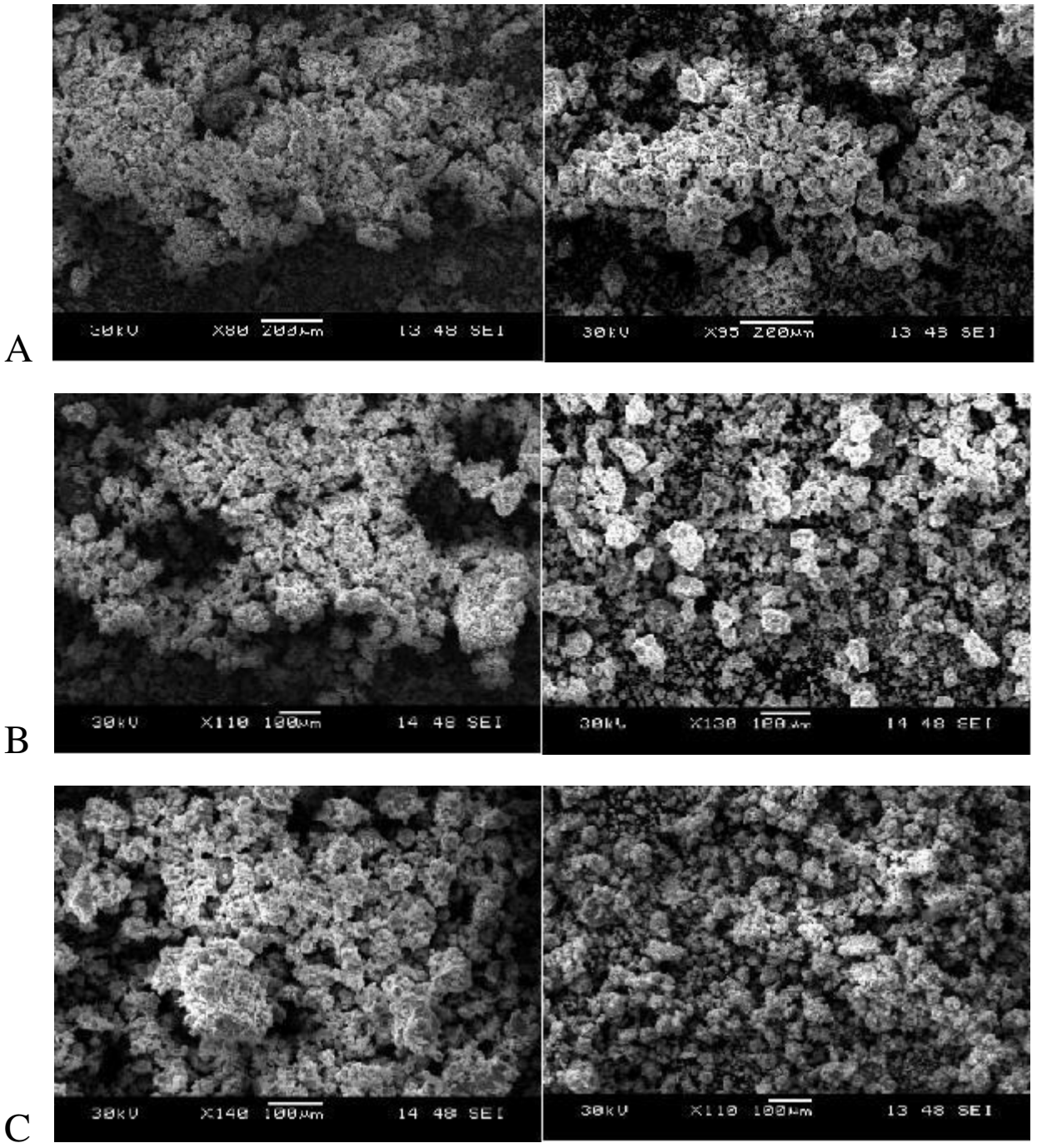

Figure 4.4 SEM images of (A) Mg / Ca / Si, (B) Mg / Ca / Si / Co and (C) Mg / Ca / Si / Fe mixtures before and after hydrogenation at 400 °C and 13.6 atm for 1 hour.

Powder X-ray diffraction patterns of samples before and after hydriding (collected under nitrogen) are displayed in Figure 4.5. The Mg_2Ca structure is clearly evident in all products

except the Fe containing products, which show only a minor fraction of this phase. Upon hydrogenation, there were no new peaks apparent in the patterns, which indicates that a disproportionation reaction did not occur under the given hydrogenation conditions.[16] The retention of characterstic peaks, with a slight shift along the 2-Theta axis after hydrogenation, shows the products absorbed hydrogen by incorporation of H atoms into interstitial sites within the crystal lattice. When the PXRD pattern for unhydrided Ca_2Mg_3Si was indexed, the unit cell parameters were a = 6.262(3) Å, c = 9.758(5) Å, V = 382.6(4) Å³, but after hydrogenation, the parameters were a = 6.277(5) Å, c = 10.120(4) Å, V = 401.9(3) Å³. This unit cell expansion corresponds to the extra space occupied by hydrogen atoms situated on the interstitial sites in the Ca_2Mg_3Si lattice. The control product and Fe containing product absorbed the most hydrogen; accordingly, these patterns show the most significant peak shifts upon hydrogenation. The patterns show no peaks for elemental Mg or Ca as these reactants were completely consumed in the reaction at the ratio used in this experiment.

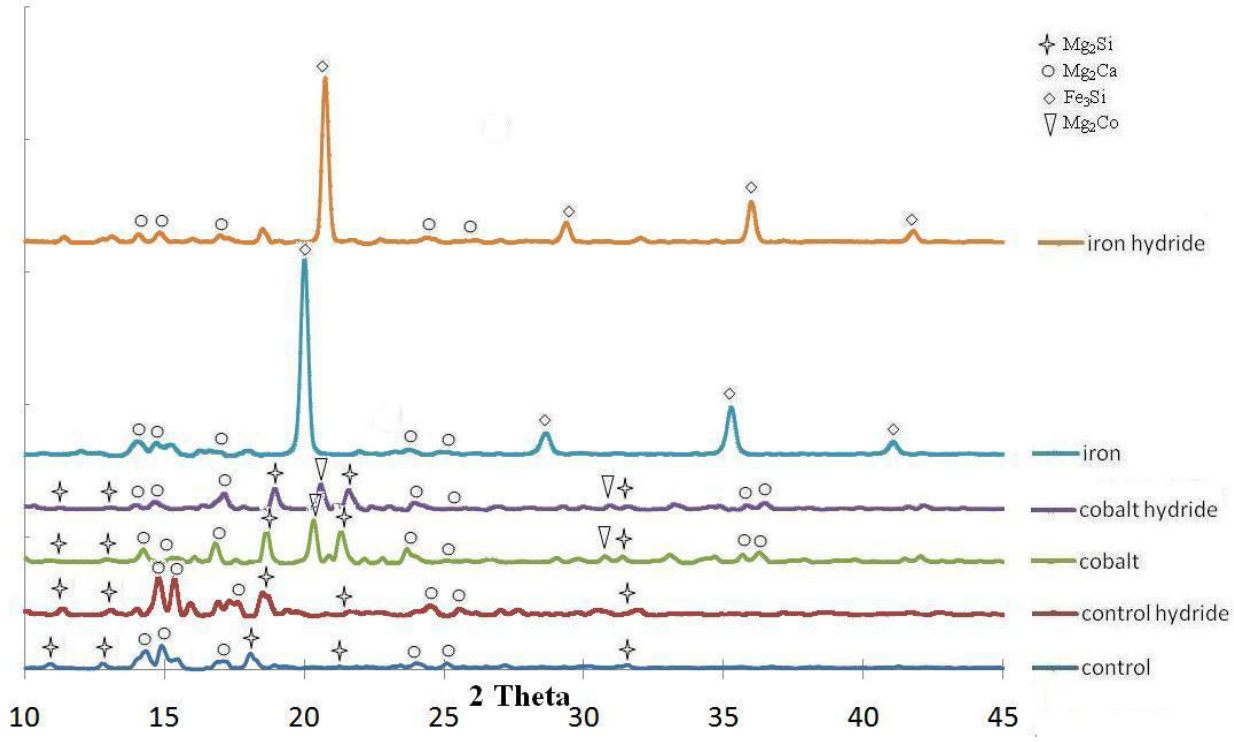

Figure 4.5 PXRD (Mo Kα) patterns for products before and after hydrogenation.

Figure 4.6 displays the PXRD patterns for ternary melts of Mg / Ca / Si which contained 9% and 17% molar Si in the starting mixture; these reactions were carried out to determine the feasibility of forming single phase $Ca_2Mg_{4-x}Si_x$. The phases present in the patterns are CaMgSi and $Ca_2Mg_{4-x}Si_x$. The formation of the fully substituted x = 1 phase (Ca_2Mg_3Si) requires the use of large amounts of Si (higher that the 17% molar Si indicated by the stoichiometry), but this also produces large amounts of CaMgSi. If stoichiometric amounts of Si are used in an attempt to synthesize Ca_2Mg_3Si, the predominant product is CaMgSi, with smaller amounts of partially substituted $Ca_2Mg_{4-x}Si_x$ ($x < 1$) (Figure 4.6A). Use of a small amount of Si (9% molar) produces nearly single phase $Ca_2Mg_{4-x}Si_x$ with a low amount of Si substitution ($x = 0.27$ in the compound studied here (Figure 4.6B)). The Mg_2Ca phase will substitute Si on the 2*a* site until it becomes more energetically favorable to form CaMgSi instead. At this point, formation of the fully substituted Ca_2Mg_3Si is nearly impossible since the Si will instead be incorporated into the CaMgSi phase. Therefore, the presence of excess Si in the melt is necessary to force the Si atoms into the Mg_2Ca structure to form the fully substituted Ca_2Mg_3Si compound.

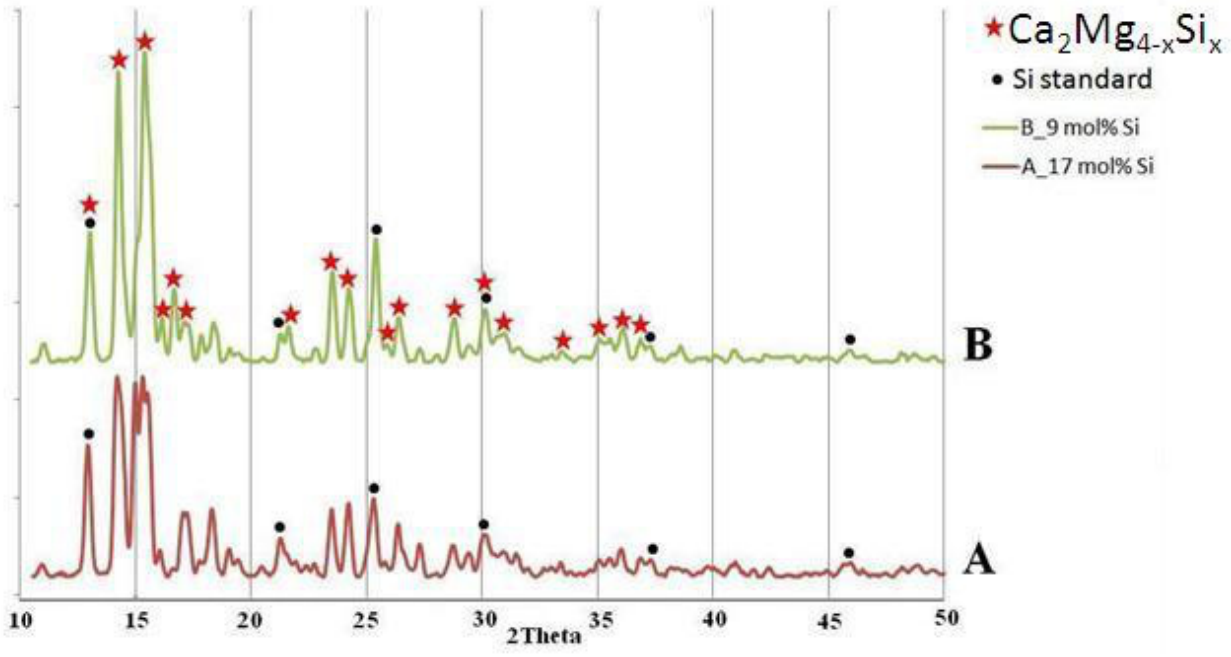

Figure 4.6 PXRD (Mo Kα) of Mg / Ca / Si mixtures reacted at mmol ratios of A=20 / 10 / 5 and B=20 / 10 / 3. Sample A is mostly CaMgSi (not marked), but sample B shows predominantly Ca_2Mg_3Si.

Release of Hydrogen

The TGA data of the compounds studied here are compared to MgH_2 in Figure 4.7. MgH_2 showed characteristic dehydrogenation at 420 ºC with 7.5 wt% desorbed hydrogen. The Mg / Ca / Si / Co mixture showed only a small amount of hydrogen desorption at ~450 ºC; the iron analog performed much better with 2.5 wt% H_2 desorption at ~380 ºC. Ca_2Mg_3Si desorbed 3.5 wt% hydrogen at ~310 ºC after hydrogenation for one hour under only 13.6 atm and 400 °C. There was no disproportionation reaction observed. The data corresponds to a stoichiometry of $Ca_2Mg_3SiH_7$ for the hydrided phase of Ca_2Mg_3Si. This was surprising because despite the lack of transition metal in the control product, desorption occurred at lower temperatures than for pure MgH_2. The presence of elemental Si atoms in the structure could be responsible for the lowered desorption temperature of Ca_2Mg_3Si with respect to Mg_2Ca, with Si acting as a pseudo-non-hydride forming "B" element in the structure. In early reports on the hydrogen storage capacity of Mg_2Ca, the maximum achieved weight percent hydrogen was 1.4 %, with later reports of 5.9 %, but with the onset of a disproportionation reaction of Mg_2Ca to MgH_2 and CaH_2. Data for the temperature at which dehydrogenation begins was not measured in these reports.[94-97] The performance of Ca_2Mg_3Si showed that, although the material had a lower weight percent hydrogen desorbed than pure Mg_2Ca, it was not subject to a disproportionation reaction and thus could be reversibly used to deliver and store hydrogen repeatedly in a power generation system.

A sample without full substitution of Si on the *2a* site (product B from Figure 4.6*)* was hydrogenated to investigate the effects of Si substitution on hydrogen storage capacity. The release of hydrogen results in a significant weight percent change at about 400 °C, which is significantly lower than the desorption onset temperature for MgH_2 (420 °C), but still higher than that of fully substituted Ca_2Mg_3Si (310 °C). The lowered desorption temperature and increased theoretical hydrogen weight percent is a result of destabilization of the hexagonal Mg_2Ca matrix by Si substitution. The intermetallic produced is a metastable lattice which can absorb significant amounts of hydrogen interstitially to form the hydride phase, while retaining enough lattice stability to desorb the hydrogen and reform the original non-hydride phase.

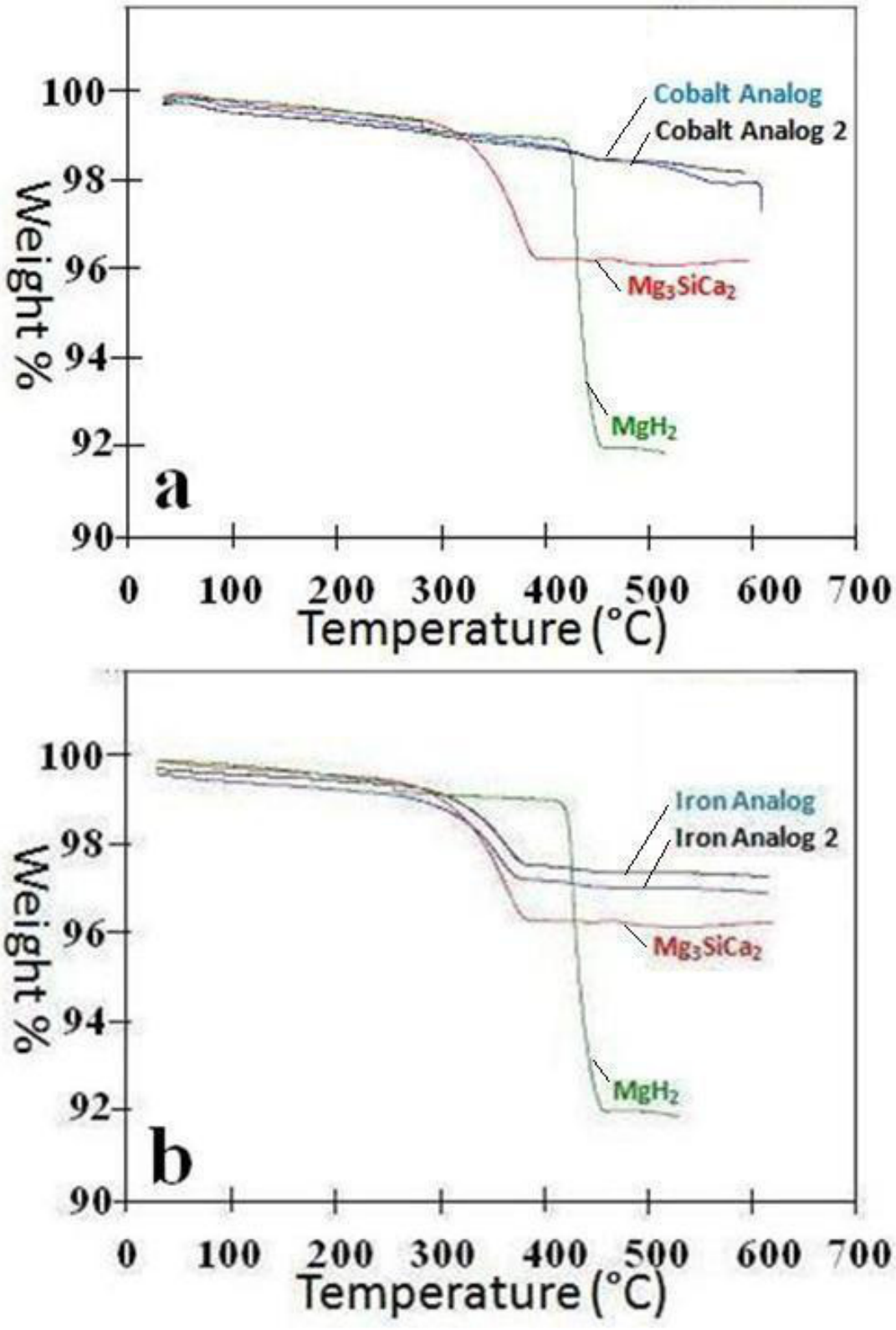

Figure 4.7 TGA data for the Co containing product (black and blue lines (a)), Fe containing product (black and blue lines (b)) with control product (red line), and MgH_2 reference (green line) (a and b).

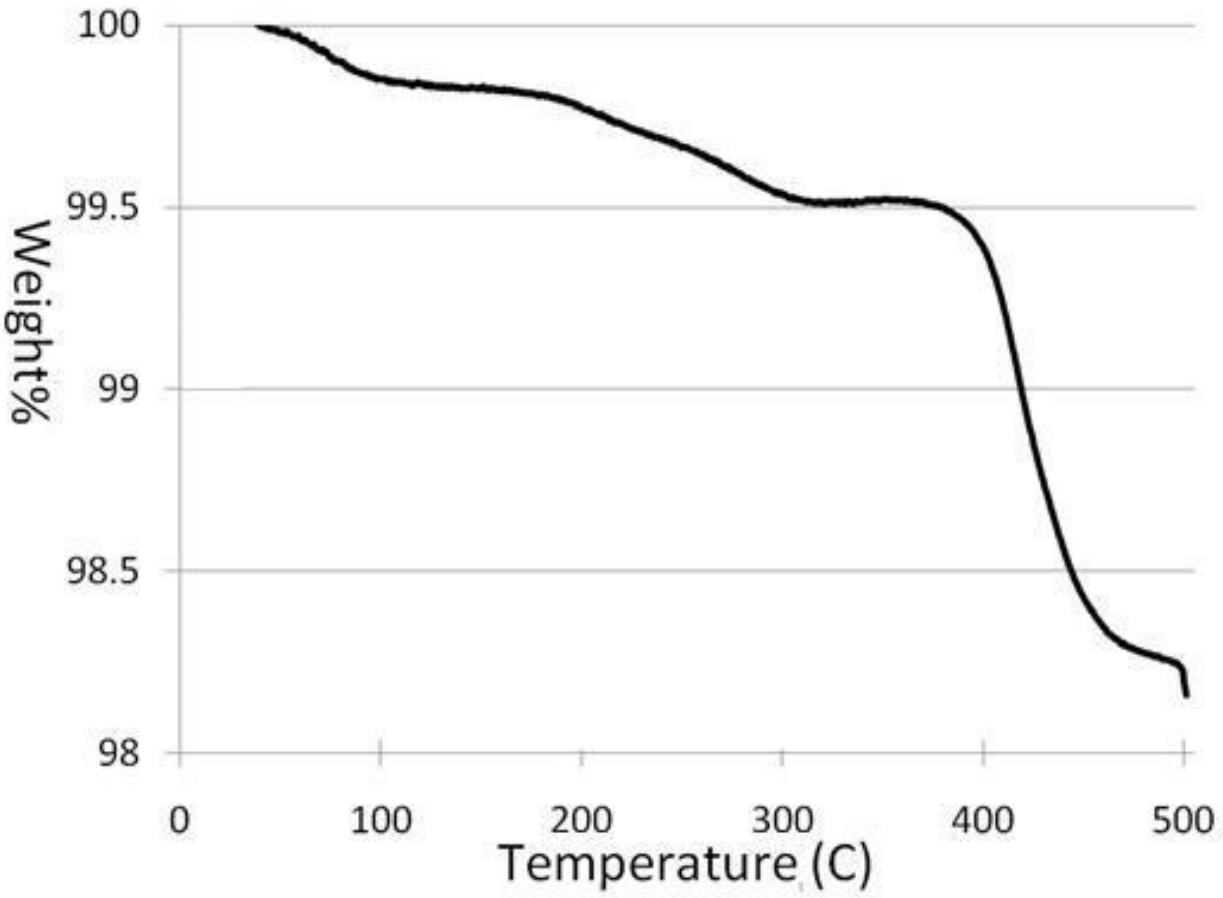

Figure 4.8 TGA data for $Ca_2Mg_{3.73}Si_{0.27}$ (Product "B" from Figure 4.6) showing 1.9 wt.% change from hydrogen desorption.

Final Discussion

Mixtures of Mg / Ca / Si at 20 / 10 / 10 mmol ratio, and Mg / Ca / Si / M (M=Fe,Co) at 20 / 10 / 10 / 20 mmol ratio were synthesized into multi-phase composites composed of Ca_2Mg_3Si with minor phase formation of Mg_2Si, Fe_3Si (for Fe containing products) and Mg_2Co (for Co containing products). The composites containing the fully substituted product, Ca_2Mg_3Si, as the main phase showed appreciable H_2 absorption (3.5 wt% hydrogen). Compared to the severe conditions (197 atm H_2 pressure and 840 K) required to hydrogenate Mg to MgH_2,[4] the hydrogenation of Ca_2Mg_3Si occurs at more feasible conditions for application of the material in hydrogen storage systems. Absorption of hydrogen occurred interstitially and no

disproportionation reactions were observed. The product materials synthesized in this investigation could perform as part of a hydrogen storage system for fuel cell application, but optimization/modification of reactions to form single phase products and proper preparation of samples will be required to maximize the weight percent hydrogen that can be stored in Ca_2Mg_3Si. The relatively low pressure required to hydrogenate Ca_2Mg_3Si could save energy costs in production of the activated hydride phase during industrial production. Formation of a single phase, hydrogen absorbing product from a ternary or quaternary melt avoids hydrogen storage problems stemming from multiphase products which contain phases that do not appreciably absorb hydrogen, such as CaMgSi and Mg_2Si.[98] Future work will be directed toward reactions resulting in the pure phase product (preferably as single crystals grown from a flux), doping of the structure in order to lower the temperature for the onset of desorption and higher hydrogenation pressures to maximize the hydrogen capacity.

CHAPTER 5

METAL TO INSULATOR TRANSITION OF CAMGSI SYNTHESIZED IN MG-AL FLUX

Introduction

Magnesium alloys and intermetallics are being widely investigated as potential aerospace and hydrogen storage materials because of their low expense and mass.[1] Other lightweight elements such as Si, Ca, Al, Zn, and Mn are commonly added to improve the strength and ductility of these materials.[99-101] This has led to growing research interest in the properties of compounds in the ternary Mg-Ca-Si system; these ternaries often occur as adventitious byproducts in mixed composites. Two phases are known in this system: CaMgSi and $Ca_7Mg_{7.5-\delta}Si_{14}$.[88,89] A third compound, Ca_2Mg_3Si, was reported but later disputed; as described in the previous chapter, this phase can be successfully grown in a Mg/Ca matrix composite.[90,91] CaMgSi is commonly observed as a precipitate in Mg alloys which increases tensile strength.[102-105] However, synthesis of single phase samples (particularly formation of single crystals) is problematic. Small crystals of CaMgSi were grown in previous studies, but measurements of physical and mechanical properties were limited by their size.[106]

In this work large single crystals of CaMgSi were reproducibly synthesized in a molten Mg-Al eutectic flux. Metal fluxes have proven to be a useful crystal growth medium; a wide variety of intermetallics and Zintl phases can be synthesized in commonly used solvents such as Al, Ga, and Sn.[25,26,107] Our lab has been investigating eutectic mixtures of metals as fluxes. In addition to lowering the melting point of the solvent, mixed fluxes introduce an additional avenue of control over the reaction chemistry. In some cases, both components of the eutectic are reactive and are incorporated into the products, as observed in the growth of $Ca_{21}Ni_2Zn_{36}$ and $Ca_6Pt_3Zn_5$ from Ca/Zn eutectic.[39] In other mixed metal solvent systems one of the flux components is inert; this is seen for several reactions in La/Ni eutectic, which yield nickel-free

compounds such as $La_{21}Fe_8Sn_7C_{12}$ and $La_6Fe_9Al_4$.[40] It is also surprisingly seen in the synthesis of CaMgSi in Mg/Al eutectic. The Mg-Al phase diagram has a broad eutectic region from 62%Al:38%Mg to 30%Al:70%Mg with a nearly uniform melting point of ~450 °C across this composition range.[30] Both flux components are usually highly reactive metals, but aluminum is not incorporated into the product. A variety of synthetic techniques and fluxes were explored, but large crystals of CaMgSi could only be obtained using Mg/Al as a reaction solvent.

The electronic properties of CaMgSi are of particular interest. From its stoichiometry, this compound would appear to be related to the Zintl phases Mg_2Si and Ca_2Si; it is in fact a substitutional variant of Ca_2Si. Magnesium silicide is a semiconductor (E_g = 0.77 eV) with the cubic Laves structure.[108] The electronic properties of orthorhombic calcium silicide are less clear-cut, although most studies indicate it is also a semiconductor.[108-111] CaMgSi is also expected to be a Zintl phase. However, our findings indicate that this phase spans the boundary between charge balanced semiconducting Zintl phases and fully delocalized polar intermetallics. Exploration of materials falling between these two classifications has been of great interest in recent years, yielding compounds with unusual structures and electronic properties.[112] In the title compound, a transition from metallic to semiconducting behavior is observed below 50 K, evidenced by resistivity and magnetic susceptibility measurements. This is accompanied by a structural distortion from the TiNiSi structure type toward a more layered structure; this was followed using powder X-ray diffraction. In addition to structural and electronic characterization, hydrogenation of this phase was also investigated; little absorption was seen, but destabilization of the lattice was evident.

Experimental Procedure

Synthesis

Mg metal slugs (3.175mm x 3.175mm, 99.95%) and Ca shot (1cm and down, 99.5%) were obtained from Alfa Aesar, and Si and Al powders (both 99+%) from Strem Chemicals. The elements Mg / Al / Ca / Si were weighed out in a 15 / 15 / 3 / 3 mmol ratio in air and placed into

a niobium crucible obtained from JXMetals, Inc. (CaMgSi crystals can be synthesized in stainless steel crucibles, but this causes incorporation of Fe, Cr, and Ni impurities). The crucible was welded shut in an argon-filled glovebox, then put into a silica tube, which was sealed under vacuum. Each reaction vessel was gently shaken several times to mix the components before being placed into the furnace. Reactions were heated from room temperature to 950 ºC in 5 hours, held at 950 ºC for 5 hours, cooled to 750 ºC in 60 hours, and held at 750 ºC for 20 hours at which point the reaction tubes were removed from the hot furnace, quickly inverted and centrifuged. It was not necessary to use a filter in the reactions because most of the product adhered to the crucible walls. When left out in air, the crystals show signs of surface oxidation after 1 week; they were therefore stored in sealed vials. Temperature programs with different cooling times (30-100 hours from 950°C to 750 °C) were explored, but the optimal cooling time was found to be 60 hours, which resulted in growth of the largest crystals in highest yield (90% based on Si). Cooling times longer than 100 hours resulted in no crystals. Stoichiometric reactions were also explored; these produced multi-phase composites of CaMgSi, Mg_2Si, Ca_2Si, and Ca_2Mg_3Si.

Elemental Analysis

Samples for SEM-EDS analysis were mounted onto Al pucks with double-sided carbon tape. Elemental compositions of products were assessed using a JEOL 5900 scanning electron microscope (30 kV accelerating voltage) equipped with PGT Prism energy dispersion spectroscopy software. Analysis of the surface of the crystals did show some residual flux coating, but measurements on the interior of shattered crystals indicated a 1 / 1 / 1 molar ratio of Mg, Ca, and Si, with no aluminum or niobium present.

Structure

Single crystal X-ray diffraction data were collected on a Bruker APEX2 single crystal X-ray diffractometer with Mo K□ source. Samples were chosen by breaking the as-synthesized crystals to obtain fragments of the appropriate size and crystal quality. Full spheres of data were collected at 293 K and 100 K under flowing nitrogen. The data was integrated by SAINT and

was corrected for absorption effects using the empirical method (SADABS).[85] Space group assignment was done by XPREP, and structure refinement was carried out using SHELXTL.[86] Crystallographic data and collection parameters are shown in Table 5.1.

Low temperature powder X-ray diffraction samples were prepared by grinding crystals in an agate mortar. Experiments were run on an original setup based on a HUBER imaging plate with Guinier camera 670 using Cu $K\alpha_1$ radiation and a Ge monochromator. Data was collected from room temperature down to 10 K by employing a closed cycle He refrigerator system using a temperature sweeping rate of 0.5 K/minute and a dwell time of 10 minutes/temperature. Data for Rietveld refinement was collected for longer exposure times (40 minutes) at 10 K, 45 K, 60 K, 200 K, and 282 K. The unit cell parameters were calculated from least-squares fits using the program package WinCSD.[113] Lattice parameters were obtained from the refinement of a set of 20 reflections common for all samples. Rietveld refinement was performed using the JANA2000 program package.[114] During Rietveld refinement the unit cells were fixed to those obtained from least –square fits (WinCSD).

Resistivity and Magnetism

Resistivity measurements were conducted by a conventional four-point *dc* method on a Physical Property Measurement System (PPMS) by Quantum Design. Crystals (size range: 5-7 mm x 1 mm x 1 mm) were mounted on the sample holder of a ^{4}He probe with a small amount of N-type Apiezon vacuum grease. Crystals were connected to the electrodes of the sample holder with 0.001 inch diameter gold wires using silver paint. Measurements were carried out from 1.8 – 300 K, using an applied excitation current of 1 mA. Magnetic susceptibility data was collected on a Quantum Design SQUID magnetic property measurement system. Crystals were held between two strips of kapton tape, oriented with the *c*-axis parallel to the applied field. Susceptibility data were collected at 2-300 K at an applied field of 100 G.

Nuclear Magnetic Resonance

Magic angle spinning (MAS) ^{29}Si NMR data was collected on a Varian Inova 500 wide-bore spectrometer. Tetramethylsilane was used as a reference. The CaMgSi crystals were

ground with NaCl in a 1 / 1 ratio by volume to facilitate spinning of the conducting material; the mixture was packed into 4 mm zirconia rotors sealed with airtight screw caps. Data was collected at 25 °C and 4 kHz spinning rate with a single pulse sequence of 2.5 μs length and 6 second relaxation delay. The spin-lattice T_1 relaxation time for CaMgSi was determined using the standard inversion recovery method.

Electronic Structure Calculations

Calculation of band structure and density of states (DOS) were performed with the TB-LMTO-ASA program package.[115] CaMgSi crystal structure parameters determined from room temperature X-ray single crystal data were used for the calculations. Addition of empty Wigner-Seitz spheres was found to be unnecessary. The following radii of atomic spheres were used: r(Ca) = 2.03 Å, r(Mg) = 1.62 Å, and r(Si) = 1.55 Å. The basis set consisted of the Ca(4s, 3d), Mg(3s, 3p) and Si(3s, 3p) with Ca(4p, 4f), Mg(3d), Si(3d) being downfolded. The calculation was made for 10368 κ-points in the irreducible Brillouin zone. Integration over the Brillouin zone was made by the tetrahedron method.

Hydrogenation and Dehydrogenation

CaMgSi crystals were ground in an agate mortar to increase the reactive surface area of the material. Samples were then activated and hydrogenated in a lab-built volumetric pressure and temperature gas control system.[116] Activation of the powder was carried out by heating under dynamic vacuum for 30 minutes at 450 ºC. Hydrogen gas was then introduced into the sample chamber at 37.4 atm (550 PSIG) and 450 ºC. The sample chamber pressure was automatically re-adjusted by the apparatus every 30 seconds for 15 intervals. When complete, the samples were removed from the sample chamber and analyzed using TGA/DSC analysis with a TA Instruments SDT 2960 Simultaneous DSC-TGA. The samples were heated to 520 ºC at 5 ºC/min then held at 520 ºC for 30 minutes. Identical DSC/TGA measurements were carried out on MgH_2 from Alfa Aesar as a standard hydride comparison.

Results and Discussion

Magnesium-based fluxes have not been widely investigated as synthesis media because of their volatility and corrosive nature. Our use of sealed steel or niobium ampoules allows for containment of the Mg vapors and facilitates flux growth of Mg-containing products. The use of a pure Mg flux does not result in formation of the CaMgSi phase, instead yielding a bulk material consisting of Mg_2Si and Mg_2Ca. The need for aluminum to promote the reaction could be due to the role of Al as either a transport agent within the flux, a destabilizing agent (which hinders the formation of Mg_2Ca and Mg_2Si by retaining Mg in the excess flux solution), or a solvent for the incorporation of elements with low solubility in molten Mg. The observation that aluminum from the flux does not incorporate into the product is surprising; this metal is usually a highly reactive solvent, facilitating the growth of aluminide intermetallics.[25,26,32,107,117,118] The existence of many Mg-Al binary phases, and no known Al-Si phases, might rationalize why the Al metal is retained in the flux without incorporation into the CaMgSi crystals. The Mg/Al eutectic flux solidifies at 450 °C, but it becomes very viscous and difficult to remove well above this temperature. Therefore the ampoules were removed from the furnace at 750 °C to ensure that the flux remained in its molten state during transfer of the reaction vessel from the furnace to the centrifuge. After centrifugation and cooling of the reaction vessels, the excess flux is found solidified in the end of the crucible which indicates successful separation. The crystals are found adhered to the wall of the ampoules on the opposite end. The maximum size of the crystals appears to be limited only by the diameter of the crucible.

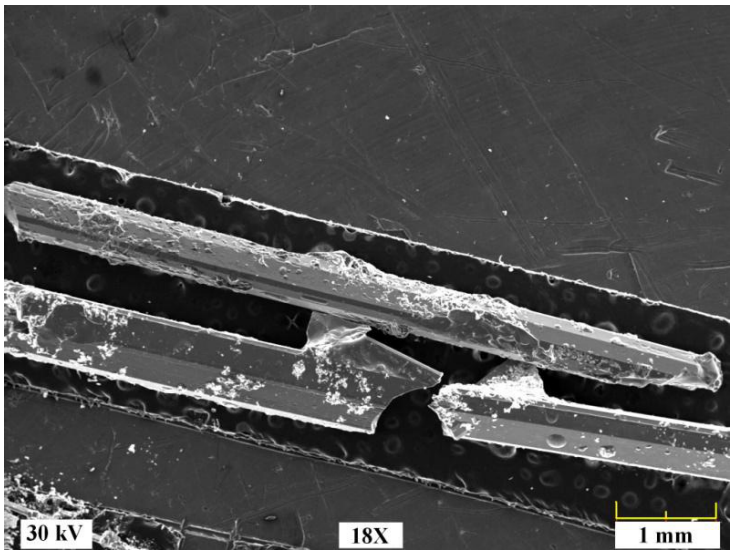

Figure 5.1 SEM image of representative crystals of CaMgSi grown in Mg/Al flux.

Figure 5.1 shows an SEM image of several large CaMgSi crystals (approx. 7 mm x 1 mm x 1 mm) which are actually broken fragments of larger crystals. Small amounts of Mg-Al flux are adhered to regions on the surface of the crystals; these areas were not targeted during elemental analysis. Analyses on several cleaved surfaces show an average mole percent composition of 33(2)% Mg, 36(2)% Si, and 31(2)% Ca. The CaMgSi crystals have a minimal phase width exemplified by many different reactions yielding products with nearly identical unit cell and elemental analysis values. An earlier study indicated a small phase width to the calcium-rich side ($Mg_{1-x}Ca_{1+x}Si$, $x \leq 0.07$), but given the Mg-rich synthesis medium used in our work, this phase width was not observed.[91]

Structural Features

CaMgSi crystallizes in the orthorhombic TiNiSi structure type, a ternary variant of the Co_2Si or anti-$PbCl_2$ structure type. Atom positions and unit cell parameters are listed in Table 5.1, and the structure is shown in Figure 5.2. The structure is formed from the complete substitution of Mg for Ca on one of the 4c sites in the Ca_2Si (Co_2Si type) lattice. This results in the formation of a 3-dimensional Mg/Si network forming channels in which the calcium cations reside. Both the Mg and Si sites are four-bonded, with highly distorted tetrahedral coordination.

The TiNiSi structure type is common for ternary intermetallic phases RTX with a 1 / 1 / 1 ratio of an electropositive metal (R = rare earth, alkaline earth, early transition metal), a late transition metal T, and a main group element X (X = Si, Ga, Al, Sn, etc.). In the hundreds of phases comprising this family of compounds, the electropositive R metal cation occupies the channels formed from the T/X framework.[119]

Table 5.1 Crystallographic data and collection parameters for CaMgSi at 298 K and 100 K.

	CaMgSi at 298 K	**CaMgSi at 100 K**
Space group	*Pnma* (no. 62)	*Pnma* (no. 62)
Cell parameter, Å	*a* = 7.4752(2) *b* = 4.42720(10) *c* = 8.3149(2)	*a* = 7.441(2) *b* = 4.4100(14) *c* = 8.292(3)
V, Å^3	275.175(12)	272.09(15)
Wyckoff Site and Atom Positions	4*c* Ca (0.01945(3), ¼, 0.68077(2)) 4*c* Si (0.27073(4), ¼, 0.38565(3)) 4*c* Mg (0.14423(5), ¼, 0.06378(4))	Ca (0.01955(4), ¼, 0.68067(4)) Si (0.27059(6), ¼, 0.38560(6)) Mg (0.14414(7), ¼, 0.06382(6))
Z	4	4
Density (calc.), g cm^{-3}	2.232	2.258
μ, mm^{-1}	2.566	2.595
Data collection range, deg.	3.67< θ < 44.84	3.68< θ < 28.07
Reflections collected	4235	2789
Independent reflections	1177 [R_{int} = 0.0272]	366 [R_{int} = 0.0525]
Parameters refined	20	20
R_1 [a)], wR_2 [b)] [$F_o > 4\sigma F_o$]	0.0210, 0.0460	0.014, 0.040
R_1, wR_2 (all data)	0.0272, 0.0480	0.0153, 0.0402
Largest diff. peak and hole [e/Å^3]	0.429 and -0.629	0.305 and -0.311
Goodness-of-fit	1.050	1.168

a) $R_1 = \Sigma \| F_o | - | F_c \| / \Sigma | F_o \|$.

b) $wR_2 = [\Sigma\, w(F_o^2 - F_c^2)^2 / \Sigma\, w(F_o^2)^2]^{1/2}$, $w = [\sigma^2(F_o^2) + (A \cdot p)^2 + B \cdot p]^{-1}$; $p = (F_o^2 + 2F_c^2)/3$; A = 0.0067, B = 0.

This structure is clearly stable for a wide range of valence electron counts, and deriving a Zintl phase model of electron transfer from the R metal to the T/X framework is not applicable in most cases.[120] In spite of this, it is tempting to view CaMgSi as a Zintl phase. It is derived from Ca_2Si, which from its stoichiometry, atomic coordination, and semiconducting properties, can be viewed as $(Ca^{2+})_2(Si^{4-})$. Replacing one calcium ion with a Mg^{2+} ion should lead to another

semiconducting Zintl phase. However, magnesium often does not behave like an alkaline earth metal in alloys and intermetallics.

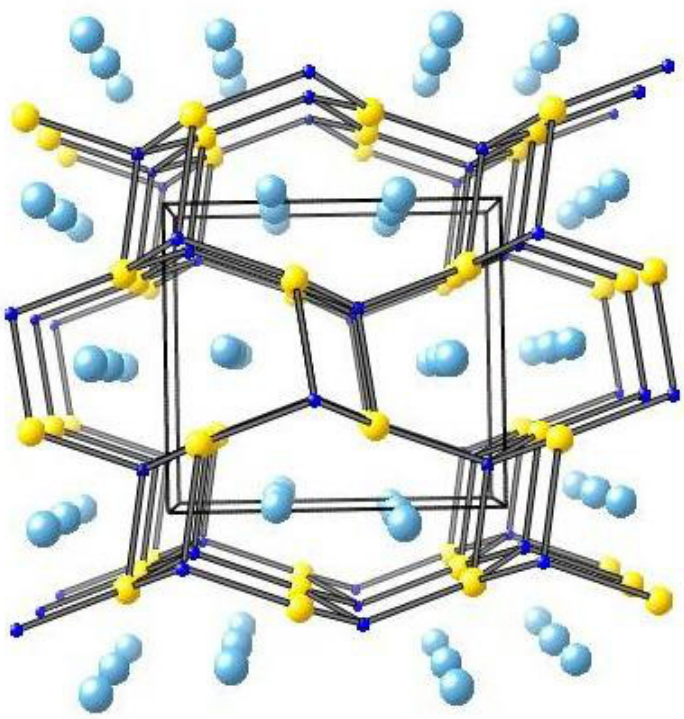

Figure 5.2 CaMgSi crystal structure viewed down the *b*-axis. Large light blue spheres are Ca atoms; yellow spheres are Mg, and small blue spheres are Si.

Incorporation of magnesium into TiNiSi structure phases has been recently observed in compounds such as EuMgT (T = Ag, Au, Tl, Pd, Si, Ge, Sn, Pb), CaMgPd, and YbMgAg, with Mg occupying a site in the "anionic" T/X network.[121,122] While these RMgX phases do appear to favor formation with a divalent R element, they vary in their overall valence electron count and are metallic. CaMgSi also has Mg bonded to Si to form the "anionic" network with short Mg-Si bonds of 2.7382(3) – 2.8234(5) Å. This would indicate this phase is in the same polar intermetallic class as the other RMgX phases. The transport properties of CaMgSi were studied to determine if this compound behaves as a semiconducting Zintl phase or a polar intermetallic.

Solid State MAS-NMR

Solid state ^{29}Si MAS NMR was used to characterize the electronic environment of silicon in the structure. One broad peak was observed, in agreement with the single Si crystallographic site in the structure. The positive chemical shift of about 160 ppm is far from the -177 ppm resonance observed for semiconducting Mg_2Si.[123] Other silicide Zintl phases are also characterized by negative ^{29}Si NMR peaks; the M_4Si_4 family (M = Na, K, Rb, Cs) has resonances in the -280 to -360 ppm region.[124,125] Semiconducting low-sodium silicon clathrates Na_xSi_{136} and doped silicon have resonances falling in the range of -100 to +100 ppm; this can be classified as the covalently bonded semiconducting silicon chemical shift region.[126] The silicon framework atoms of metallic clathrates such as Na_8Si_{46} and $Na_{16}Rb_8Si_{136}$ exhibit Knight shifts due to the conduction electrons in these phases; all their ^{29}Si resonances occur from 200 ppm up to 1000 ppm.[127] Other metallic silicides also have ^{29}Si Knight shifts in this region, such as Ba_3Si_4 (281 ppm) and $Y_5Si_2B_8$ (217 ppm).[128,129]

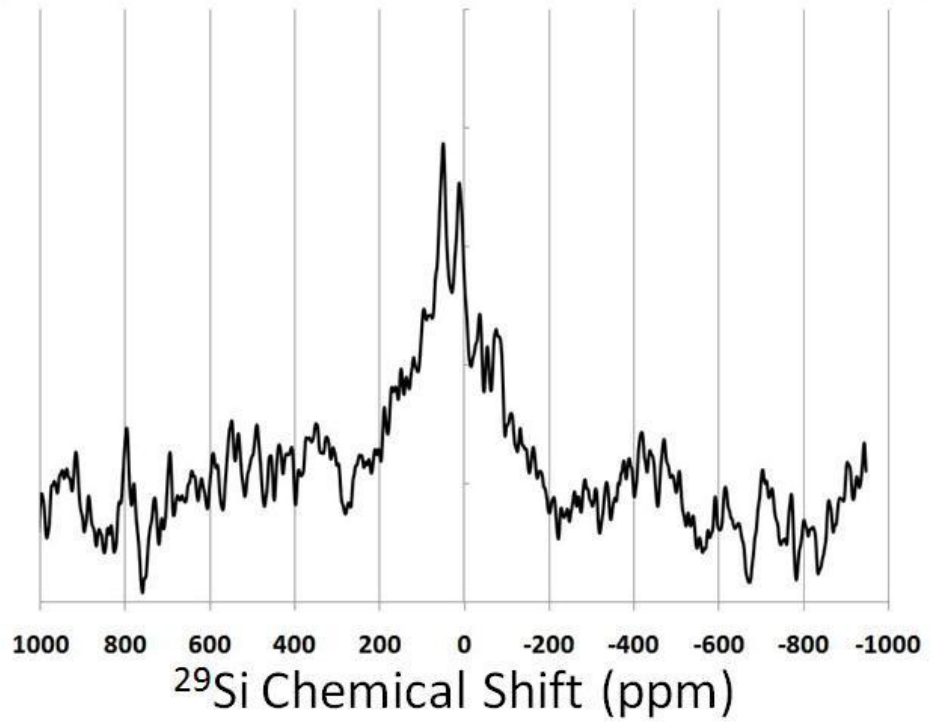

Figure 5.3 ^{29}Si MAS-NMR spectrum for CaMgSi showing a positive chemical shift of ~160 ppm. Peak splitting was caused by spinning sidebands due to the limited spinning rate caused by conduction of the sample.

The 160 ppm peak observed for CaMgSi is on the border of the Knight shift region, and far from the diamagnetic shifts seen for Zintl phases. Figure 5.3 shows the MAS-NMR spectrum for CaMgSi. This indicates poor metal behavior. Additional evidence comes from the observed T_1 spin-lattice relaxation time of 4 seconds for the ^{29}Si nuclei in CaMgSi. This relaxation is facilitated by the conduction electrons, and is orders of magnitude shorter than the slow relaxation characteristic of diamagnetic semiconducting silicide phases such as Mg_2Si (T_1 = 600 seconds).[123,130]

Magnetic Susceptibility

The high temperature molar susceptibility of CaMgSi is small, positive, and independent of temperature, as shown in Figure 5.4. This is consistent with Pauli paramagnetism due to delocalized conduction electrons. A plot of χT vs. T yields a line which intersects both axes at 0 K (Figure 5.4a, inset), also indicative of Pauli paramagnetism. As the material is cooled below 50 K there is a sharp increase in the magnetic susceptibility, evidence of a transition to an insulating/semiconducting state in which the conduction electrons become localized; this occurs at the temperature range corresponding to the local minimum in the resistivity data (Figure 5.4b; *vide infra*). The conductions electrons could be trapped by defects in the lattice or by a specific local environment in the structure. Later experiments using electron paramagnetic resonance techniques showed a sharp peak corresponding to the localized unpaired conduction electrons. This sharp peak had high intensity at low temperature and as the temperature was increased above 70 K, the intensity of the peak remained constant. Similar behavior is seen in another compound, $Sc_3B_{0.75}C_3$; a jump in the susceptibility is seen at the same temperature as a metal-to-insulator transition which the authors postulate may be due to a change in structure.[131]

In addition to the SQUID measurements conducted with the single crystals oriented parallel to the applied magnetic field, powdered sample was also run to observe the effects of random/averaged orientation on the M-I transition. The χ vs. T plot for the powdered sample is shown in Figure 5.5. Although the transition was still visible, its intensity was reduced. This indicates that the transition is more abrupt and causes a greater increase in the susceptibility when the crystals are left intact so that anistropic effects along the c-axis can manifest.

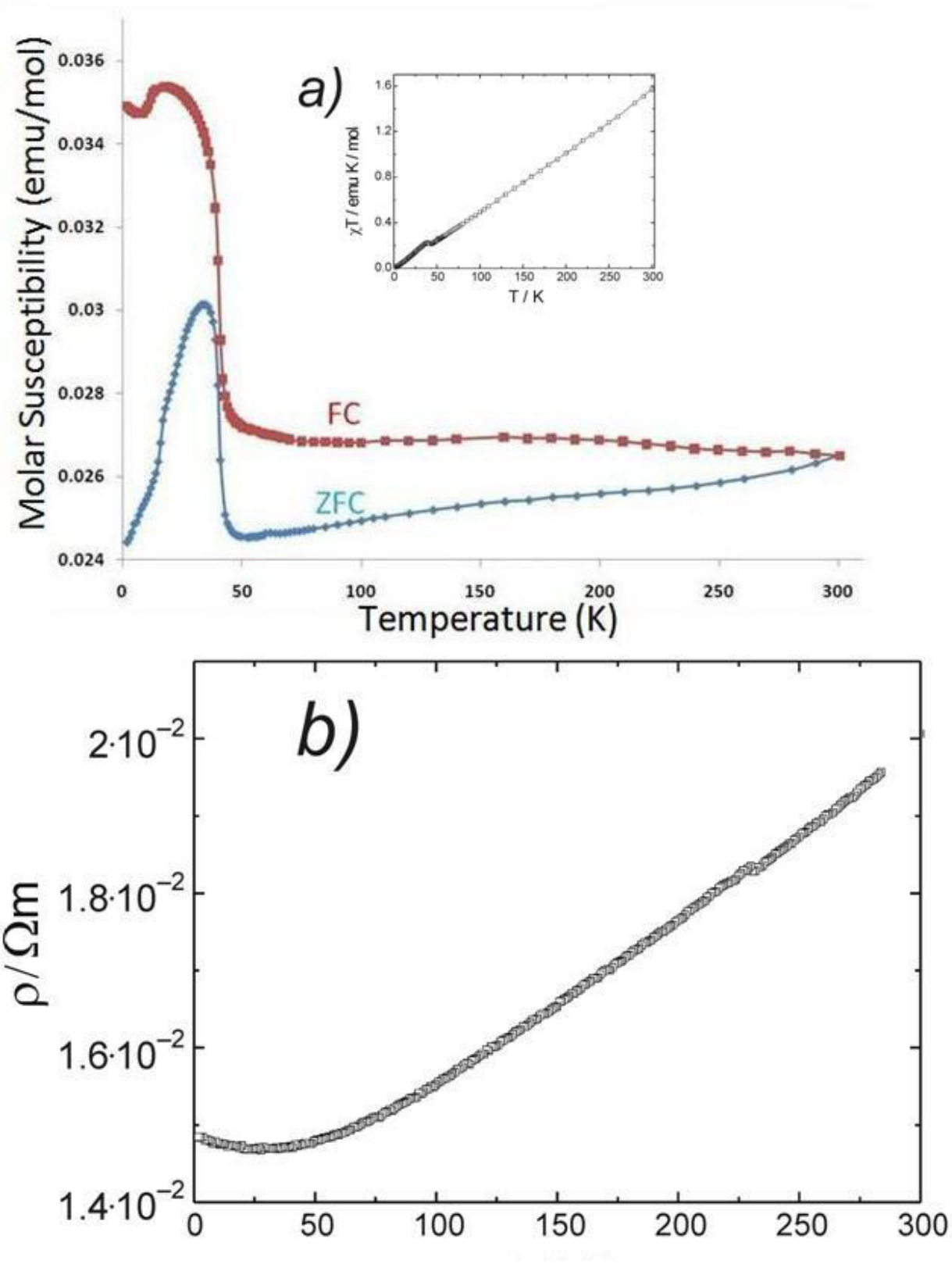

Figure 5.4 Temperature dependencies of a) magnetic susceptibility (100 G field applied along *c*-axis) and b) resistivity.

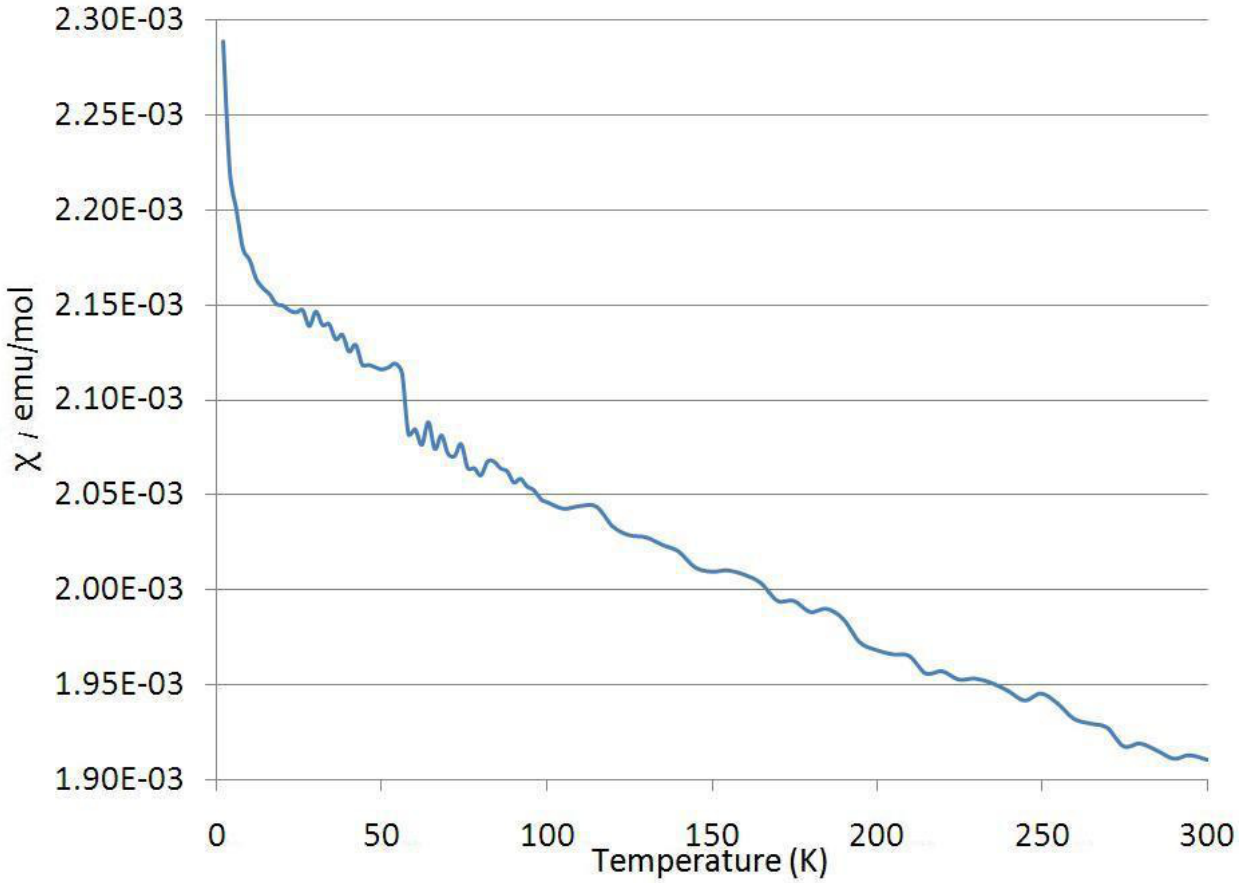

Figure 5.5 Powder CaMgSi sample temperature dependency at 100 G applied field.

Resistivity

Resistivity data from 1.8-300 K is shown in Figure 5.4b. At high temperatures, the resistivity of CaMgSi has a metallic-like dependence on temperature. A change in slope of the plot occurs at 50 K, with an inflection point at about 35 K. This indicates that an electronic phase transition from metal to semiconductor occurs when cooling through this temperature range. Other compounds with similar metal-to-semiconductor electronic transitions, such as $Sc_3B_{0.75}C_3$ and Ba_3Si_4, also display minima in their resistivity plots at temperatures of 50 K and 30K, respectively.[128,131] The room temperature resistivity of CaMgSi is 1.95 Ω·cm; this value lies in the overlap of typical metallic (10^{-5} – 10^{1} Ω·cm) and semiconductor (10^{-2} – 10^{5} Ω·cm) resistivity ranges.[43] $Sc_3B_{0.75}C_3$ and Ba_3Si_4 are also poor metals above their transition temperatures, having room temperature resistivities of 0.185 and 1.20 Ω·cm, respectively.

However, Mg_2Si is a well-characterized semiconductor that shows poor metal behavior when doped with small amounts of aluminum; this includes resistivity data showing a change in behavior from metallic at high temperature to semiconducting at low temperature.[132] Therefore, calculations of the theoretical density of states of CaMgSi were carried out to determine if the metallic behavior at high temperatures is intrinsic or due to inadvertent doping.

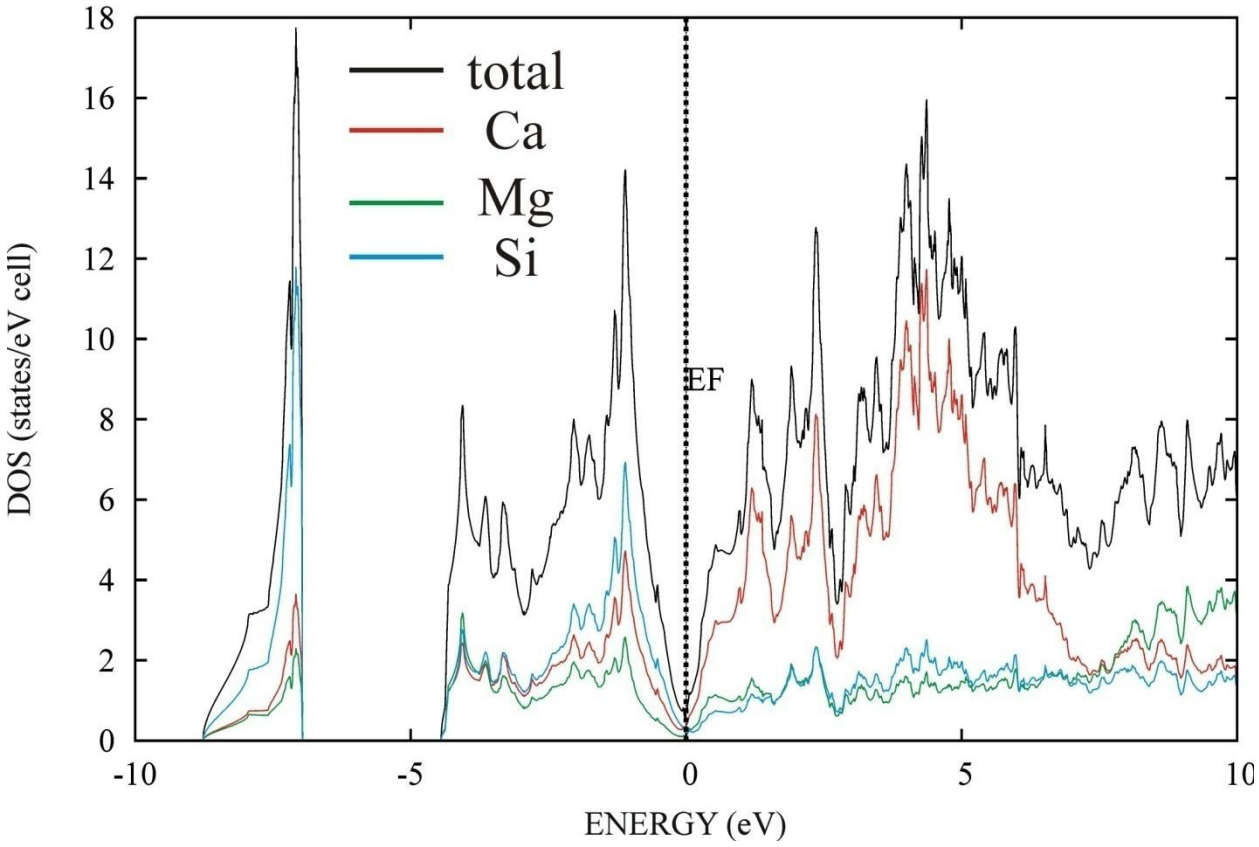

Figure 5.6 Total and partial density of states for CaMgSi. Contributions from different atoms are color-coded.

Electronic Structure Calculations

The calculated density of states (DOS) for CaMgSi is shown in Figure 5.6. The analysis of total DOS reveals that while there is a pronounced pseudo-gap at the Fermi level, the compound is still intrinsically metallic. Ca, Mg and Si contribute to the states near E_f nearly equally. This indicates significant cation-anion orbital mixing (hybridization); the interaction between Mg and Si has significant covalent character, which leads to the closing of the gap at the Fermi level and poor-metal behavior. The experimentally observed temperature dependence and magnitude of resistivity for CaMgSi above 50 K is typical for a poor metal with a low DOS at E_f. The room temperature ^{29}Si NMR resonance is also in agreement with poor metal behavior. As the temperature is lowered, it is possible that thermal contraction or a subtle structural transition occurs that causes the pseudogap to enlarge and become an actual gap at the Fermi level, resulting in semiconducting behavior below 50 K.

Structural Distortion at Low Temperature

Low temperature powder diffraction data was collected to probe the structural characteristics of the metal to insulator transition. As the sample is cooled to 10 K, the unit cell parameters decrease due to the expected thermal contraction of the cell volume (Figure 5.8). However, this decrease shows a distinct change in slope at T = 50 K, particularly noticeable for the a-axis parameter. To determine the cause of this deviation, Rietveld refinements were performed on data collected at 10 K, 45 K, 60 K, 200 K and 282 K. Information and parameters used for Rietveld refinement are shown in Table 5.2. No splitting of the peaks due to a lowering of symmetry was observed and all peaks could be indexed in the primitive orthorhombic unit cell of the TiNiSi structure. However, analysis of bond lengths revealed abrupt changes upon lowering the temperature below 50 K, highlighted in Figure 5.7.

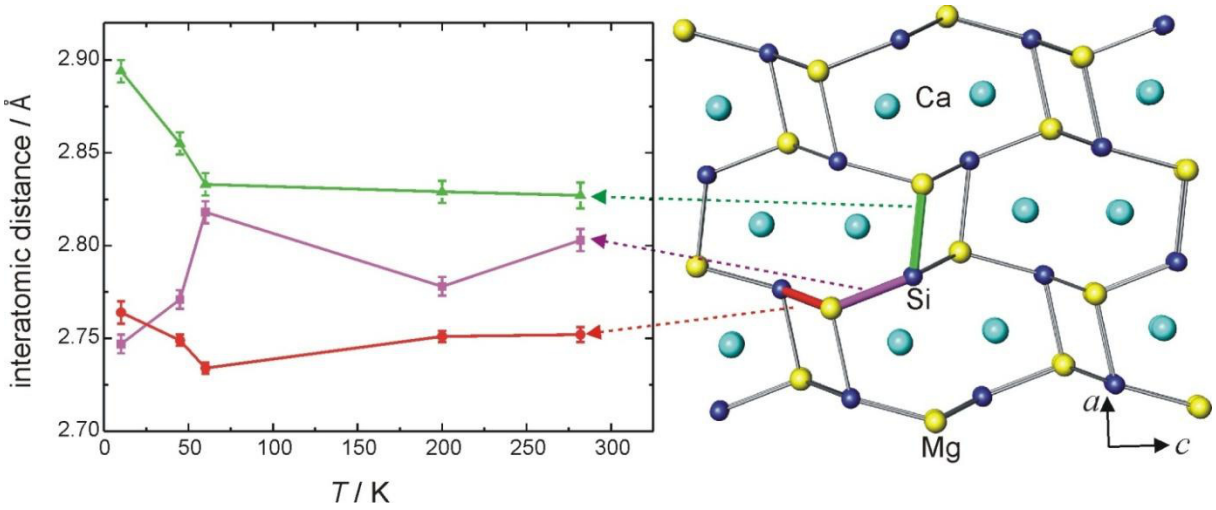

Figure 5.7 Temperature dependence of individual Mg-Si bonds for CaMgSi.

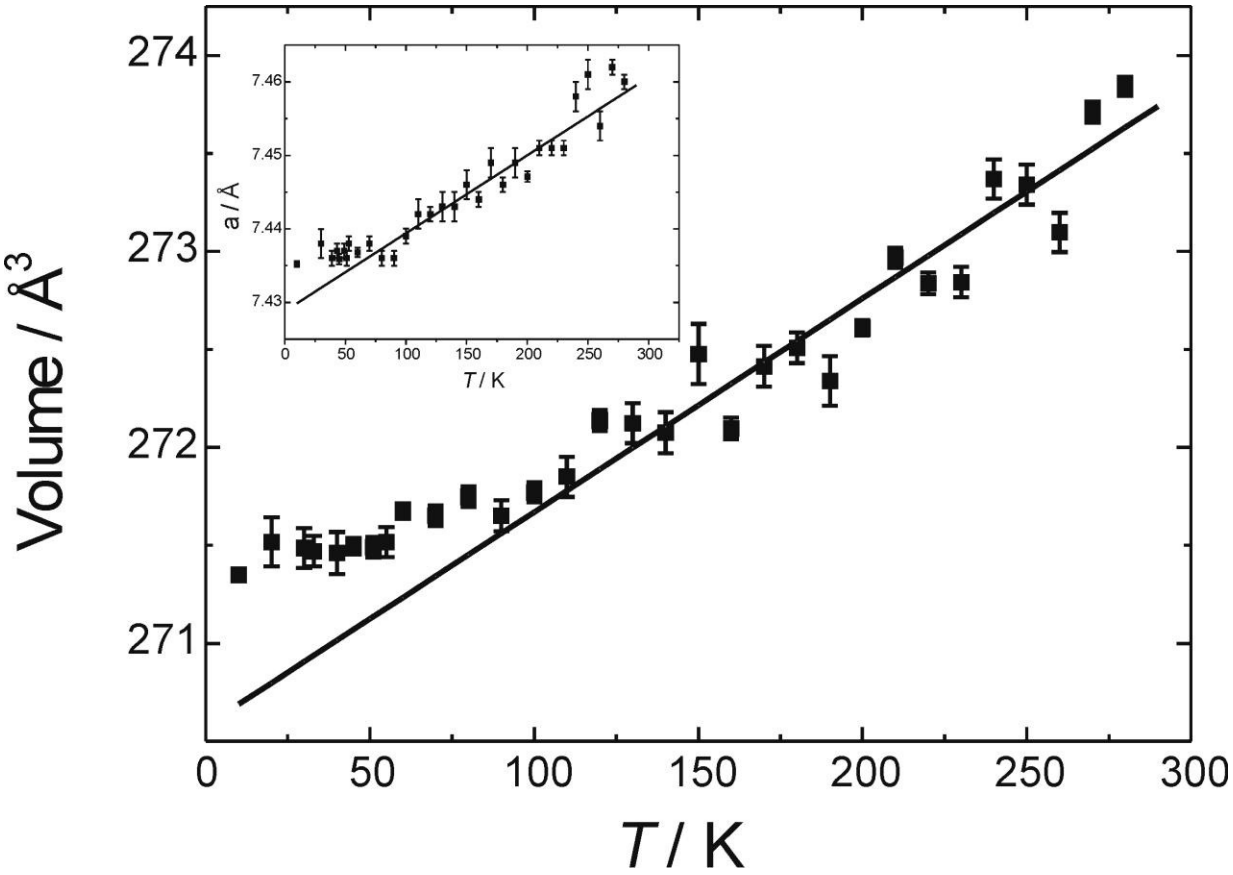

Figure 5.8 Temperature dependence of unit cell volume and (inset) unit cell parameter, *a*, for CaMgSi. The linear dependence at temperature range 100-300 K is depicted by solid line.

The nature of this distortion is a transition from a 3-D Mg/Si network toward a more layered structure. The structure can be viewed as puckered hexagonal Mg/Si sheets stacked along the a-axis and pinned together. At room temperature the intralayer bonds (red and magenta in Figure 5.7) and the interlayer bond (green) are of similar length. Upon cooling below 60 K, the interlayer bond lengthens abruptly (producing a noticeable effect on the a-axis parameter), while the intralayer magenta bond decreases and the intralayer red bond increases only slightly. The local environments of Mg and Si atoms change from distorted tetrahedral coordination by four neighboring Si and/or Mg, respectively, to the low temperature coordination best described as 3+1: trigonal planar with three Si or Mg atoms at a distance of about 2.75 Å (two red and one magenta bond) and one elongated contact (green) of 2.90 Å. This reduces the puckering of the layers in the low temperature structure (Figure 5.9).

Table 5.2 Data collection parameters and Rietveld refinement results for powder X-ray diffraction data of CaMgSi.

Collection temperature	**10 K**	**45 K**	**60 K**	**200 K**	**282 K**
Space group	*Pnma* (no. 62)				
Lattice parameters [a], **Å**	*a* = 7.4352(4) *b* = 4.4064(3) *c* = 8.2823(6)	*a* = 7.4359(7) *b* = 4.4071(4) *c* = 8.2847(9)	*a* = 7.4368(6) *b* = 4.4074(4) *c* = 8.2886(9)	*a* = 7.4471(7) *b* = 4.4133(4) *c* = 8.2945(8)	*a* = 7.460 (1) *b* = 4.4194(4) *c* = 8.3061(9)
***V*, Å^3**	271.35(3)	271.50(5)	271.68(4)	272.61(4)	273.84(5)
Wavelength, λ, Å	Cu$K\alpha_1$ radiation (1.540598 Å)				
Range 2θ, degree	15-100				
Stepsize 2θ, degree	0.01				
Profile function	pseudo-Voigt				
Background function	36 Chebyshev polynoms				
R_P R_{wP} χ^2	0.015 0.021 1.77	0.015 0.020 1.58	0.015 0.021 1.68	0.014 0.019 1.51	0.015 0.022 2.07
Coordinates for atoms in position 4*c* (*x*, ¼, *z*)					
Ca, *x*	0.0155(4)	0.0178(4)	0.0167(4)	0.0179(4)	0.0160(4)
Ca, *z*	0.6808(3)	0.6814(3)	0.6836(3)	0.6855(3)	0.6793(3)
Mg, *x*	0.1477(5)	0.1478(6)	0.1442(6)	0.1472(6)	0.1444(6)
Mg, *z*	0.0648(5)	0.0637(5)	0.0615(5)	0.0655(5)	0.0643(5)
Si, *x*	0.2634(5)	0.2690(5)	0.2683(6)	0.2720(6)	0.2701(6)
Si, *z*	0.3798(4)	0.3800(4)	0.3828(4)	0.3811(4)	0.3824(5)

[a] The unit cell parameters were calculated from least-squares fits using the program package WinCSD.

A similar modification of the TiNiSi structure type is seen in EuZnSn.[133,134] Much like the low temperature form of CaMgSi, EuZnSn has very weakly puckered layers, and the

interlayer Zn-Sn distance is much larger (by 0.26 Å) than the intralayer Zn-Sn bond lengths. Both TiNiSi and EuZnSn crystallize in the *Pnma* space group with the same Wyckoff sites occupied, but due to the distinct difference in the nature of the bonding, these structures are referred to as isopointal instead of isotypic. Displacive phase transitions resulting in symmetry changes have been seen between related structures in the TiNiSi family.[45] For instance, UFeGe has the TiNiSi structure at high temperatures, but below 500 K adopts a distorted monoclinic structure (α-UFeGe).[46] The lack of peak splitting indicates that the abruptly changing bond lengths in CaMgSi do not signal a phase transition to a structure type with different symmetry. The structure change is instead a more subtle conversion toward the isopointal EuZnSn structure; this distortion is evidently sufficient to initiate a band gap opening and a metal to insulator transition.

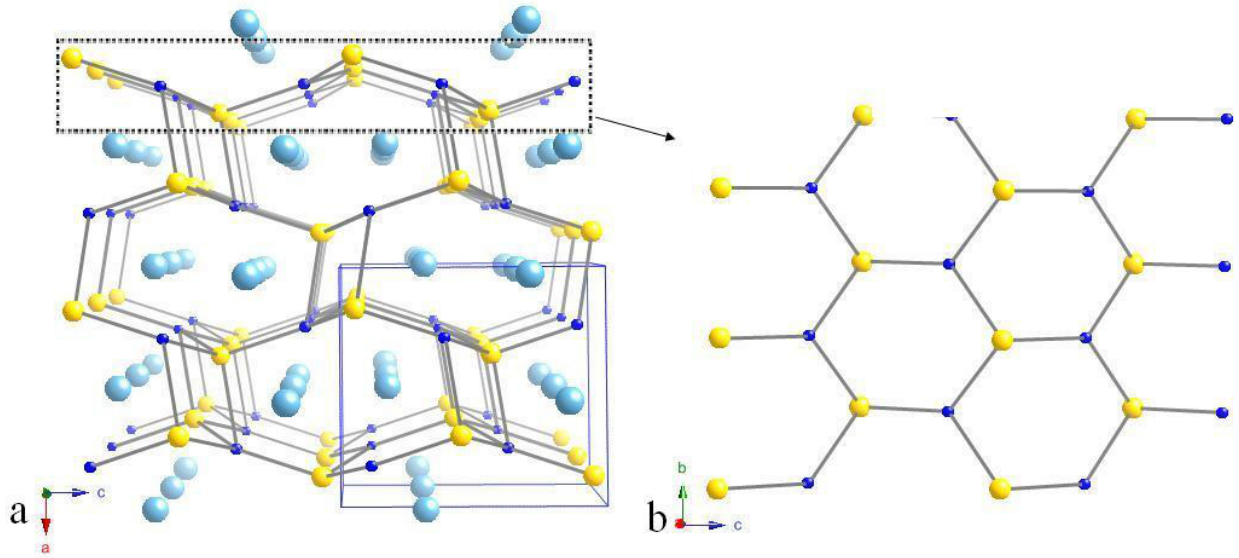

Figure 5.9 The CaMgSi structure at 10K. a) Structure viewed down the *b*-axis. b) The Mg/Si puckered layer, viewed down the *a*-axis. The Mg-Si bonds within this layer are in a small range of 2.74-2.77Å and the puckering angle is reduced, indicative of this sheet becoming more 2-dimensional below the metal to insulator transition temperature.

Hydrogen Storage and Thermal Stability

CaMgSi has previously been reported to have very little hydrogen absorption capability.[135] Poor hydrogen absorption could be a result of the contracted structure of the phase which has minimal interstitial space to accommodate hydrogen atoms. After exposure to 37.4 atm of H_2 at 450 ºC, the thermogravimetric data for CaMgSi shows very little weight loss from room temperature through 500 °C (less than 0.5 wt.% for multiple sample runs). Decomposition of the compound occurred above 500 ºC; powder XRD data for these dehydrogenated samples indicates formation of elemental Mg and Ca_2Si. Magnesium deposits are also visually apparent on the surface of the samples after this process. CaMgSi crystals which had not been hydrogenated do not exhibit the same behavior upon heating, remaining stable up to 1000 °C (the maximum temperature applied in the TGA). This is consistent with previous reports stating that CaMgSi melts congruently at 1234 °C.[91] Absorption of even a trace of hydrogen evidently destabilizes the lattice of this compound; release of hydrogen from $CaMgSiH_x$ induces an irreversible disproportionation reaction which causes the release of Mg and formation of the more stable binary compound, Ca_2Si.

Final Discussion

Mg/Al eutectic flux provides a unique crystal growth environment which allows for the formation of large crystals of CaMgSi. The size of these crystals enables the use of a variety of characterization techniques which have shown that this phase behaves like a polar intermetallic at high temperatures, but undergoes a metal to insulator transition and becomes semiconducting below 50 K. This is accompanied by a subtle structural distortion from the TiNiSi structure type to a closely related but more 2-dimensional structure type. Several RMgT analogs (R = Ca, Sr, Ba; T = Si, Ge, Sn) can be grown from Mg/Al eutectic, and may also be susceptible to these distortions and their accompanying electronic modifications.

CHAPTER 6

MG-AL FLUX SYNTHESIS: TECHNIQUES, PRELIMINARY ANALYSIS AND FUTURE WORK

The Analogs of CaMgTt (Tt=Si, Ge, Sn)

Introduction

After synthesizing and characterizing CaMgSi, it was logical to explore analogs based on substitution of Si for other Group 14 elements. Initial reactions with Ge and Sn in Mg-Al flux produced the target phases, CaMgGe and CaMgSn, which are structural analogs of CaMgSi. Since CaMgSi undergoes a metal-insulator transition, transport and susceptibility measurements were carried out on both the Ge and Sn analogs to observe any phase transitions. PPMS measurements posed some challenges due to the slight air sensitivity of CaMgGe and CaMgSn and the time required to set up samples which caused some samples to oxidize slightly before being run.

The observation of anisotropic effects in CaMgSi validated investigation of the same effects in CaMgGe and CaMgSn. In the susceptibility studies of CaMgSi, when the crystals were oriented with field along the c-axis instead of in powdered form, the M-I transition was much more abrupt and additional features were observed at low temperature. The anisotropic effects related to the orientation of the crystal in the field (for SQUID) or the positioning of the leads (for PPMS) provided insight into how this related to the M-I transition. Previous work on powdered samples of $Ca_{2-x}Mg_xTt$ (Tt = Sn, Pb) grown from sealed stoichiometric reactions and indicate temperature independent semiconductor or poor metal behavior.[138]

Reactions exploring hole/electron doping of CaMgSi, CaMgGe and CaMgSn were also carried out and interesting effects were obtained, especially with respect to product crystal size. For the reactions of Mg / Al / Ca / Si, the inclusion of Al in the flux was imperative for the

growth of the CaMgSi single crystals. Inclusion of Al into Mg / Al / Ca / Ge did produce the target CaMgGe phase, but reactions of Mg / Ga / Ca / Ge yielded much larger crystals than those synthesized in Al. For growth of the CaMgSn phase, inclusion of Al in the reaction inhibited crystal growth altogether. CaMgSn could be synthesized in good yield from a pure Mg flux, but inclusion of In in the Mg / In / Ca / Sn reactions led to larger crystals. A pattern in the growth of these analogs was observed which correlated the location of the elements in the periodic table, to which mixed flux would produce the best crystals of the desired phase. CaMgSi was best synthesized in a Mg / Al flux, CaMgGe in a Mg / Ga flux and CaMgSn in a Mg / In flux. The synthesis of the analogs was optimized to produce large single crystals in >90% yield (based on the Group 14 element). No incorporation of the Group 13 flux component was seen in the products.

Results and Discussion for CaMgGe

The phase transition in CaMgSi at 50 K and the phase transition in CaMgGe at 40 K have stark similarities in the features of the susceptibility plots. Figure 6.1 shows the CaMgGe SQUID plot. Even the small upturn in the susceptibility at 5 K was observed for both Si and Ge analogs. The M-I transition in CaMgSi was accompanied by a deviation from normal thermal contraction which resulted in distortion of the orthorhombic structure toward Mg-Si 2-D layers instead of 3-D network. CaMgGe has similar layers made up of Mg-Ge instead of Mg-Si. The CaMgGe (a = 7.502(4), b = 4.445(3), c = 8.360(5)) unit cell parameters are very similar to that of CaMgSi (a = 7.4752(2), b = 4.42720(10), c = 8.3149(2)) which could be related to the very similar susceptibility behavior of the compounds. Low temperature PXRD data has been collected for CaMgGe and will be analyzed in future work to determine if displacive distortion occurs analogously to the distortion in CaMgSi. Table 6.1 shows the crystallographic data for CaMgGe and CaMgSn.

Structural Features of Ge and Sn Analogs

Table 6.1 Crystallographic data for CaMgGe and CaMgSn.

Composition	CaMgGe	CaMgSn
Space group	*Pnma* (no. 62)	*Pnma* (no. 62)
Data collection temperature, K	296	296
Cell parameter, Å	*a* = 7.502(4) *b* = 4.445(3) *c* = 8.360(5)	*a* = 7.878(3) *b* = 4.693(2) *c* = 8.759(4)
V, Å^3	278.8(3)	323.8(2)
Wyckoff Site and Atom Positions	4*c* Ca (0.02063(11), ¼, 0.67985(10)) 4*c* Ge (0.26821(5), ¼, 0.38440(5)) 4*c* Mg (0.14330(7), ¼, 0.06338(16))	Ca (0.01971(7), ¼, 0.68257(7)) Sn (0.26670(2), ¼, 0.38371(2)) Mg (0.14377(13), ¼, 0.06308(12))
Z	4	4
Density (calc.), g cm^{-3}	3.264	3.755
μ, mm^{-1}	12.677	9.345
Data collection range, deg.	3.65< θ < 29.20	3.48< θ < 29.16
Reflections collected	3129	3599
Independent reflections	410 [R_{int} = 0.0363]	476 [R_{int} = 0.0233]
Parameters refined	20	20
R_1 [a)], wR_2 [b)] [$F_o > 4\sigma F_o$]	0.0266, 0.0465	0.0156, 0.0326
R_1, wR_2 (all data)	0.0213, 0.0452	0.0139, 0.0322
Largest diff. peak and hole [e/Å^3]	0.539 and –0.651	0.576 and -0.543
Goodness-of-fit	1.082	1.156

[a)] $R_1 = \Sigma \| F_o | - | F_c \| / \Sigma | F_o \|$.

[b)] $wR_2 = [\Sigma w(F_o^2 - F_c^2)^2 / \Sigma w(F_o^2)^2]^{1/2}$, $w = [\sigma^2(F_o^2) + (A \cdot p)^2 + B \cdot p]^{-1}$; $p = (F_o^2 + 2F_c^2)/3$; A = 0.0067, B = 0.

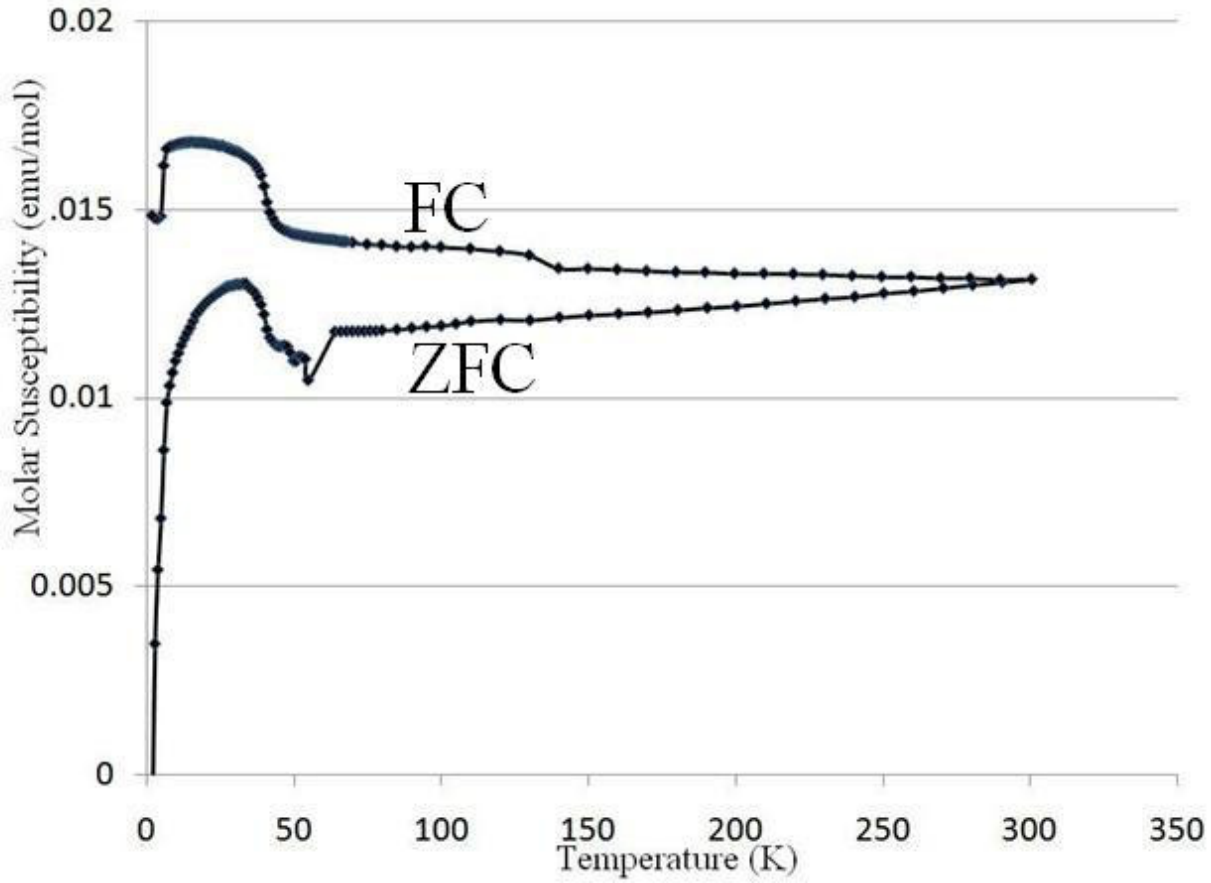

Figure 6.1 SQUID data showing phase transition in FC/ZFC χ vs. T plots for CaMgGe.

The resistivity curve from the PPMS shown in Figure 6.2 indicates CaMgGe behaves like a metal and has an upturn in resistivity at 40 K, which corresponds to the electronic transition observed in the susceptibility plot. The absolute resistivity values ($3.5*10^{-3}$ to $5.0*10^{-3}$ Ω•m) of the curve are within those designated as a metal behavior (typical metallic ($10*10^{-5}$ – $10*10^{1}$ Ω•cm).[43] Despite the increasing resistivity with decreasing temperature, CaMgGe does not ever have resistivity high enough to be considered a semiconductor. CaMgSi had absolute resistivities of $1.5*10^{-2}$ Ω•m and $1.95*10^{-2}$ Ω•m at 50 K and 298 K, respectively. CaMgGe had much lower resitivities of $4.5*10^{-5}$ Ω•m and $3.5*10^{-5}$ Ω•m at 50 K and 298 K, respectively. The lower resistivity of CaMgGe compared to CaMgSi is a reflection of the germanide's more metallic nature based on traditional periodic trends.

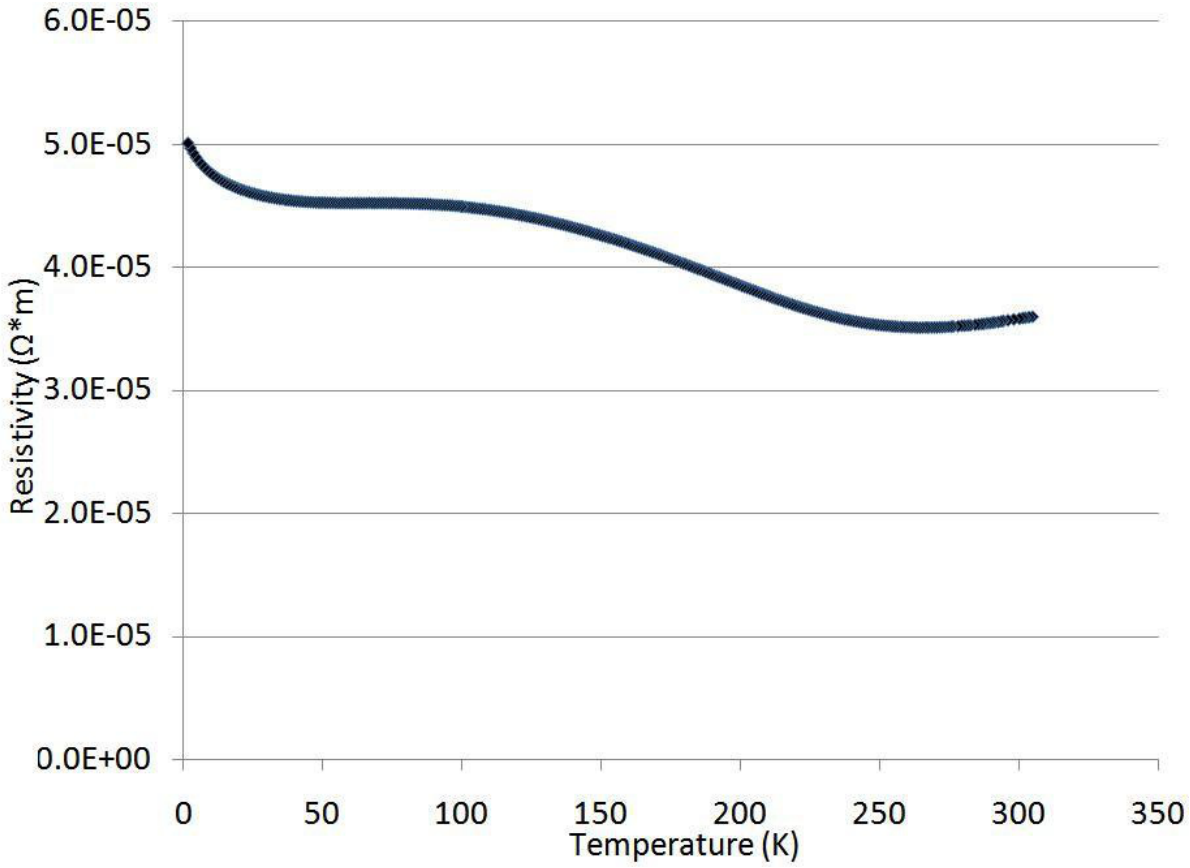

Figure 6.2 Resistivity data for CaMgGe.

Results and Discussion for CaMgSn

Compared with CaMgGe and CaMgSi, CaMgSn has very different electronic, magnetic and structural properties. The unit cell of CaMgSn (V = 323.8 Å^3) is significantly larger than that of the silicide (V = 275.175 Å^3) and germanide (V = 278.8 Å^3) analogs and its magnetic susceptibility behavior reflects a stark difference as well. The larger unit cell for the stannide results from longer bond distances between the larger atoms in the lattice. Comparing the atomic radii of Si, Ge and Sn (1.176 Å, 1.25 Å, and 1.45 Å, respectively) reveals that the size difference does follow normal periodic size trends, but the jump from Ge to Sn shows a large increase in size. The stannide has a much more traditional metallic behavior, showing temperature independent paramagnetism with a Curie tail appearing at low temperatures. There is no low temperature (at ~5 K) upturn as in the case for the silicide and germanide analogs, which also is a

reflection of the very different bonding within the compound. The susceptibility plot shown in Figure 6.3 for CaMgSn shows a stark difference from the plots of CaMgSi and CaMgGe. The pronounced transition observed in CaMgSi and CaMgGe, was very subtle for CaMgSn and shows in the plot as a shoulder at about 20 K. This is consistent with previous reports about CaMgSn and it's behavior as a poor metal.[138] The plots indicate a trend for the CaMgSi, CaMgGe and CaMgSn having transition temperatures that are shifted to lower temperatures when moving down in the Group 14 elements.

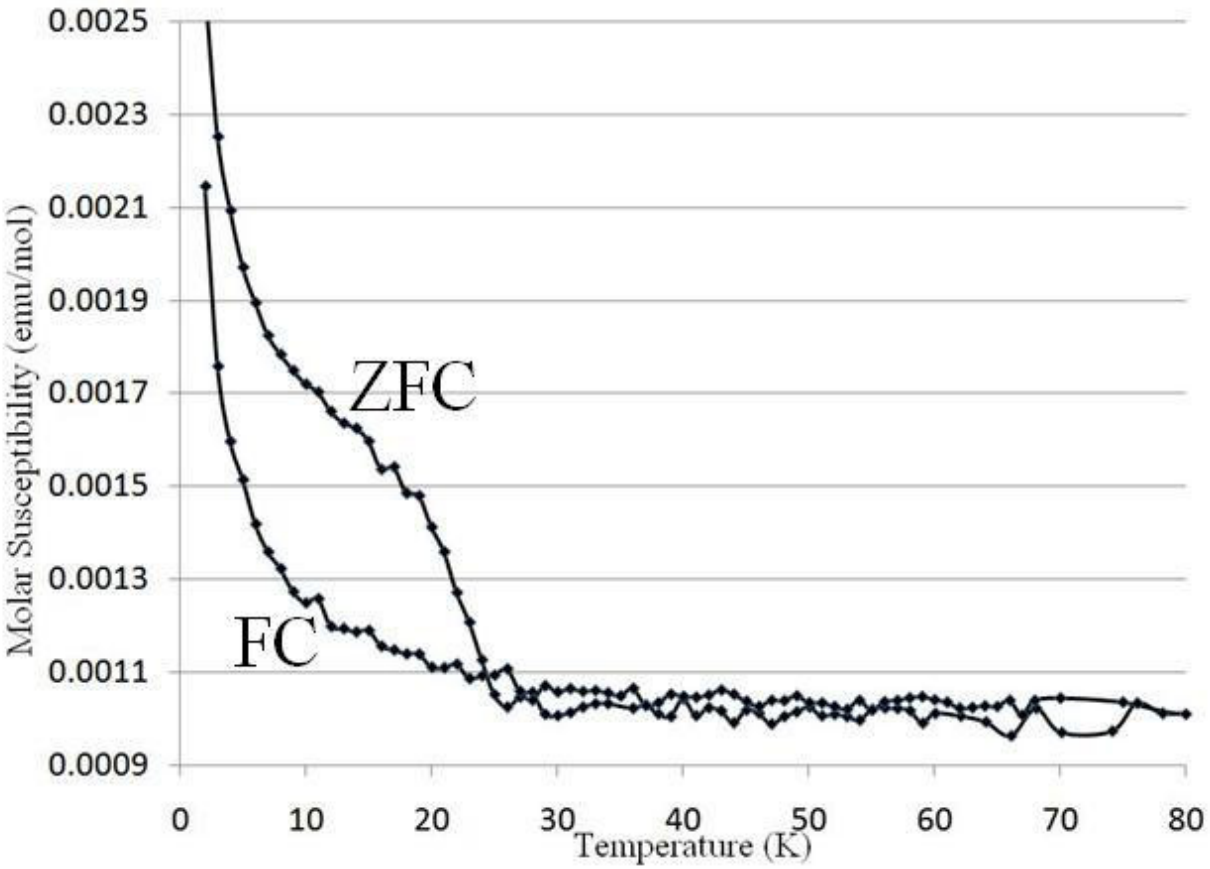

Figure 6.3 FC/ZFC χ vs. T susceptibility plot for CaMgSn.

$Yb_6Mg_{11}Fe_2Si_5$ and $Eu_8Mg_{18}Si_{13}$ Grown in Mg-Al Flux

The Mg-Al flux is an excellent solvent for lanthanide elements, which were included as reactants in several syntheses. These reactions produced crystals that were stored in the crystal bank (see Table 6.7), but two reactions of particular interest yielded very large crystals of $Eu_8Mg_{18}Si_{13}$ and $Yb_6Mg_{11}Fe_2Si_5$, respectively. These were screened for preliminary electronic and magnetic characterization. The crystals produced in these reactions were relatively air stable (did not decompose even after weeks of exposure to air). The crystallographic information for $Eu_8Mg_{18}Si_{13}$ and $Yb_6Mg_{11}Fe_2Si_5$ are shown in Table 6.2 and Table 6.4, respectively.

Table 6.2 Crystallographic data for $Eu_8Mg_{18}Si_{13}$.

Space group	*P-62m* (no. 189)
Data collection temperature, K	296
Cell parameters, Å	$a = b = 14.621(3)$ $c = 4.4073(9)$
V, Å^3	816.0(3)
Z	8
Density (calc.), g cm^{-3}	3.327
μ, mm^{-1}	15.564
Data collection range, deg.	$1.61 < \theta < 34.11$
Reflections collected	6429
Independent reflections	1196 [$R_{int} = 0.0977$]
Parameters refined	47
R_1[a)], wR_2 [b)] [$F_o > 4\sigma F_o$]	0.0399, 0.1091
R_1, wR_2 (all data)	0.0353, 0.0792
Largest diff. peak and hole [e/Å^3]	3.765 and –1.415
Goodness-of-fit	1.121

[a)] $R_1 = \Sigma \| F_o | - | F_c \| / \Sigma | F_o |$.

[b)] $wR_2 = [\Sigma w(F_o^2 - F_c^2)^2 / \Sigma w(F_o^2)^2]^{1/2}$, $w = [\sigma^2(F_o^2) + (A \cdot p)^2 + B \cdot p]^{-1}$; $p = (F_o^2 + 2F_c^2)/3$; A = 0.0067, B = 0.

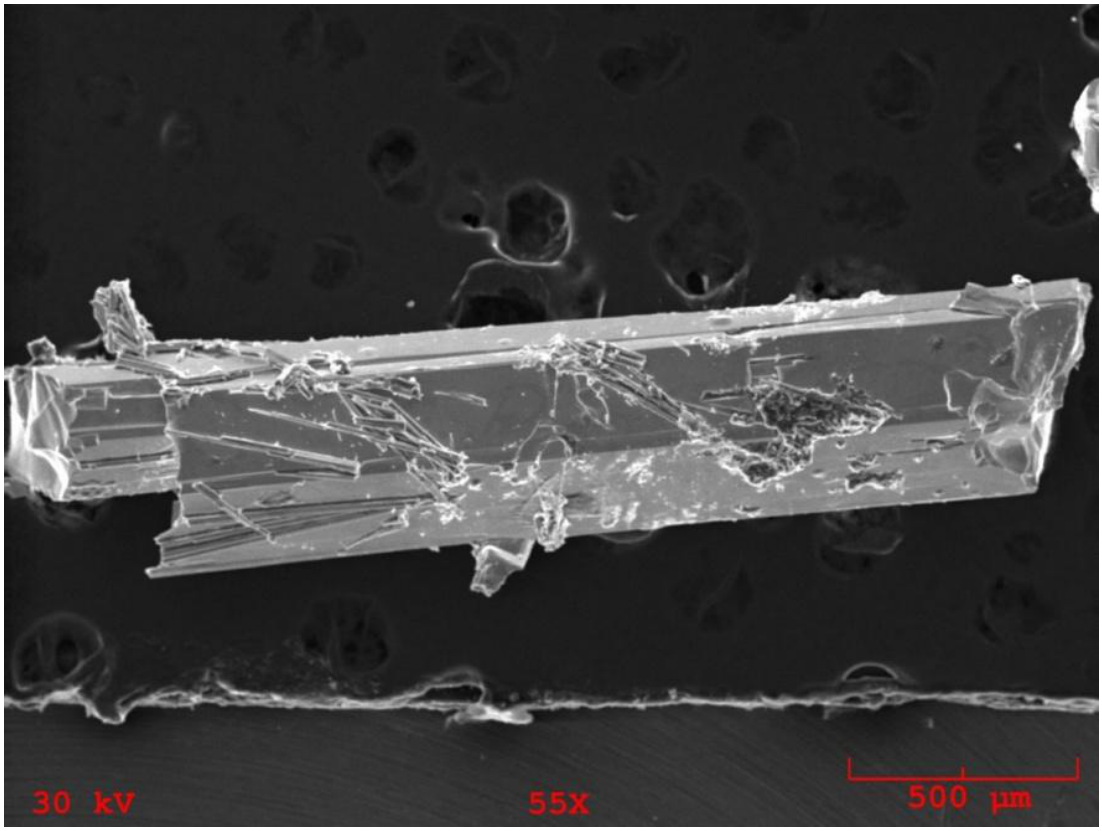

Figure 6.4 $Eu_8Mg_{18}Si_{13}$ SEM image.

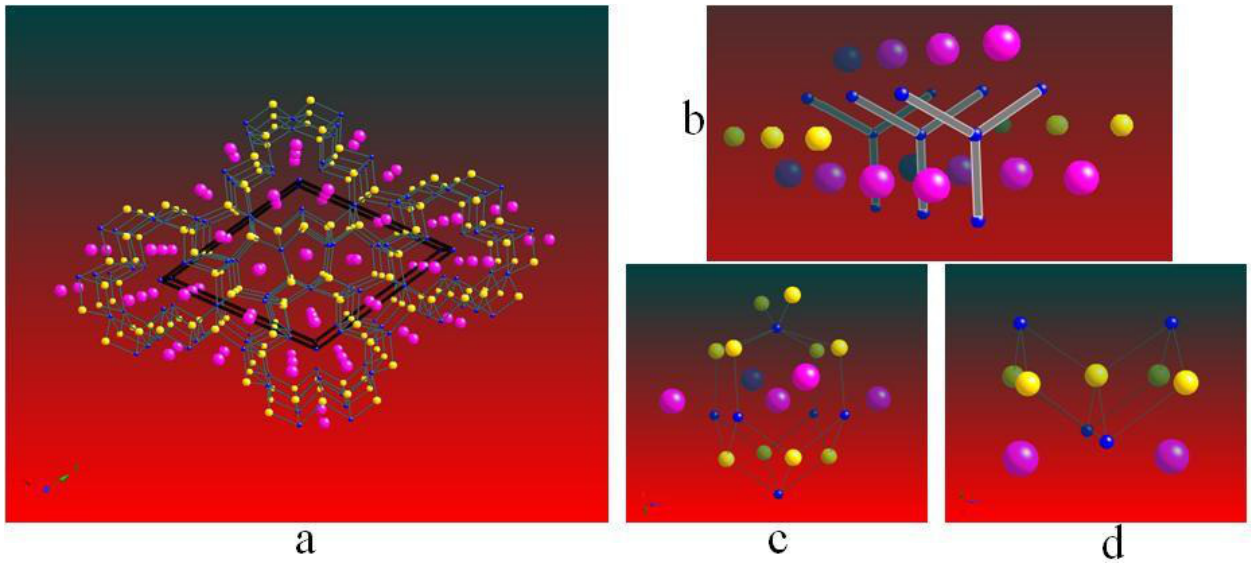

Figure 6.5 (a) Expanded crystal lattice of $Eu_8Mg_{18}Si_{13}$ with hexagonal unit cell outlined in black; (b) planar Si_4^{8-} silane units; (c) europium local environment; (d) tetrahedral $MgSi_4$ coordination.

The $Eu_8Mg_{18}Si_{13}$ phase was synthesized from a mixture of Mg / Al / Ca / Si / Eu at a 15 / 15 / 4 / 2 / 1 mmol ratio in welded stainless steel crucibles which were encased in quartz ampoules. Later reactions were carried out in niobium crucibles to ensure there were no impurities, but initial reactions were conducted in stainless steel for better cost effectiveness. The reaction vessels were heated to 950 °C in 5 hours, held for 5 hours, cooled to 750 °C in 80 hours and held at 750 °C for 24 hours then centrifuged. A representative crystal is shown in Figure 6.4.

Table 6.3 Wyckoff sites, atomic coordinates, equivalent isotropic displacement parameters [$Å^2$] and occupancies of $Eu_8Mg_{18}Si_{13}$.

	Wyckoff Site	**Atomic Coordinates**	**U_{eq}**	**Occupancy**
Eu1	*2c*	2/3, 1/3, 0	0.0129(3)	1
Eu2	*3g*	0.82212(6), 0, 1/2	0.0137(1)	1
Eu3	*3f*	0.43789(7), 0, 0	0.0091(1)	0.76257
Mg1	*3f*	0.2754(5), 0, 1/2	0.0105(5)	1
Mg2	*6k*	0.8756(3), 0.5193(4), 1/2	0.0122(4)	1
Mg3	*3f*	0.43789(7), 0, 0	0.0091(1)	0.23743
Mg4	*6j*	0.6267(4), 0.8069(4), 0	0.0117(4)	1
Si1	*1a*	0, 0, 0	0.058(4)	0.72693
Si2	*3f*	0.1722(3), 0, 0	0.0109(3)	1
Si3	*3f*	0.6411(4), 0, 0	0.0099(3)	1
Si4	*6k*	0.8295(4), 0.3099(1), 1/2	0.0097(3)	1

A $Ba_5Mg_{18}Si_{13}$ analog has been previously reported, and exhibits the variable occupancy of crystallographic sites in the lattice which leads to a range of stoichiometries of Ba in the compound between 5-8. In the $Ba_5Mg_{18}Si_{13}$ reports, the planar starlike Si_4^{8-} units were studied in depth and it was found that these crystallographic units contributed to the electronic and magnetic susceptibility of the compound, which was reported as having metallic conductivity with temperature–independent Pauli paramagnetism.[139]

This compound has interesting structural features that include both trigonal planar and pyramidal Si_4 anionic units and Mg atoms tetrahedrally coordinated by Si (Figure 6.5). Normal Zintl electron counting to charge balance $Eu_8Mg_{18}Si_{13}$ is complicated by the multiple charges of

the Si_4 anionic units and the mixed valence of Eu^{2+}/Eu^{3+}. The 8-/10- charge of the Si_4 anionic units depends on if they are planar or pyramidal, respectively. The short bonds to Si3 (2.9708(52) Å) and Si4 (3.1470(25) Å) by the 3*f* Eu3/Mg3 site is indicative of Eu^{3+} atoms substituting for Mg^{2+}. The fully occupied Eu sites have much longer bond lengths (0.5 Å longer) than the mixed Eu/Mg site. Mixed valence was not possible for the $Ba_8Mg_{18}Si_{13}$ analog reported previously (there is only one possible oxidation state for Ba as Ba^{2+}). The bond lengths for Mg-Si and Eu-Si are shown in Table 6.3.

Table 6.4 Eu-Si, Mg-Si and Eu/Mg-Si bond lengths (in Å) of $Eu_8Mg_{18}Si_{13}$.

	Eu1	**Eu2**	**Eu3/Mg3**	**Mg1**	**Mg2**	**Mg4**
Si1	*	3.4089(8)	*	*	*	*
Si2	*	3.3783(19)	*	2.6705(49)	*	2.7998(52)
Si3	*	3.4444(40)	2.9708(52)	*	2.8452(35)	2.7239(51)
Si4	3.3856(26)	*	3.1470(25)	2.7786(53)	2.7863(58)	2.7480(51)

The magnetic susceptibility plot for this compound shows it has Curie-Weiss metallic behavior with ferromagnetic ordering at 10 K as shown in Figure 6.6. The calculated Weiss constant (θ) agrees well with the Curie temperature (T_c) and thus the compound orders with negligible frustration (see Figure 6.6 inset). Calculation of the magnetic moment per formula unit with all Eu atoms as Eu^{2+} (theoretical μ_B = 7.94 per Eu^{2+} atom) would be 63.0 μ_B. The observed moment of 23.3 μ_B is much lower than that calculated for exclusively Eu^{2+} in the compound. Eu^{3+} has a theoretical moment of 0 and its presence in the compound is the cause for the lower than expected magnetic moment. According to the occupancy of the mixed Eu/Mg site, there are 3 Eu^{3+} atoms and 5 Eu^{2+} atoms per formula unit and this would lead to a theoretical moment of 23.8 μ_B, which is in much closer agreement to the observed magnetic moment.

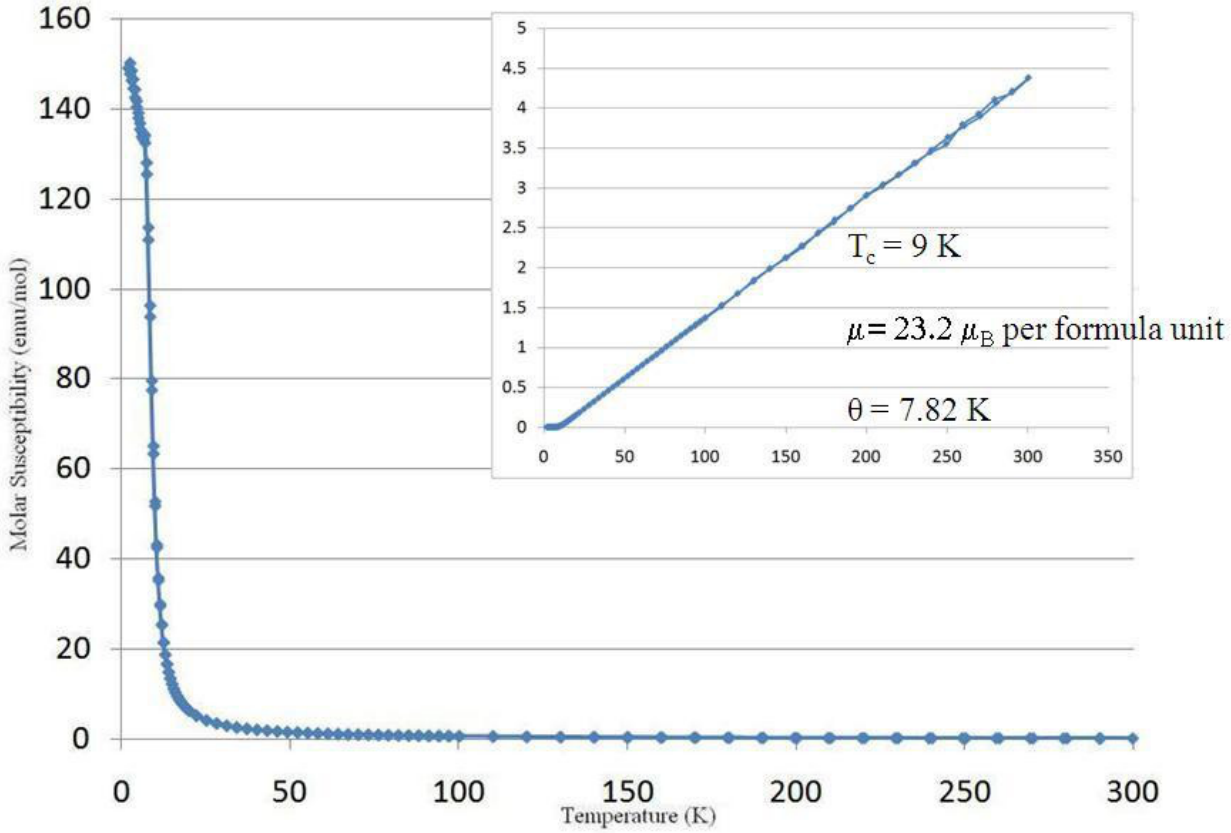

Figure 6.6 χ vs. T magnetic susceptibility plot (collected at 100 G) for $Eu_8Mg_{18}Si_{13}$ with 1/ χ vs. T plot, Curie temperature, magnetic moment per fomula unit and Weiss constant shown in inset.

In a similar reaction, $Yb_6Mg_{11}Fe_2Si_5$ was grown in the form of large single crystals. The phase was synthesized from a mixture of Mg / Al / Ca / Si / Yb at a 15 / 15 / 4 / 2 / 1 mmol ratio in welded stainless steel crucibles which were encased in quartz ampoules. Fe was leached from the crucible and incorporated into the product. Later reactions were carried out in niobium crucibles with Fe added as a reactant (Mg / Al / Ca / Si / Fe / Yb at 15 / 15 / 4 / 2 / 0.8 / 1 mmol ratio). The reaction vessels were heated to 950 °C in 5 hours, held for 5 hours, cooled to 750 °C in 80 hours and held at 750 °C for 24 hours then centrifuged. The SEM image of the compound is shown in Figure 6.7. There are no known analogs of this structure making this work the discovery and initial characterization of the phase. The magnetic susceptibility of this compound shows normal Curie-Weiss behavior; see Figure 6.10.

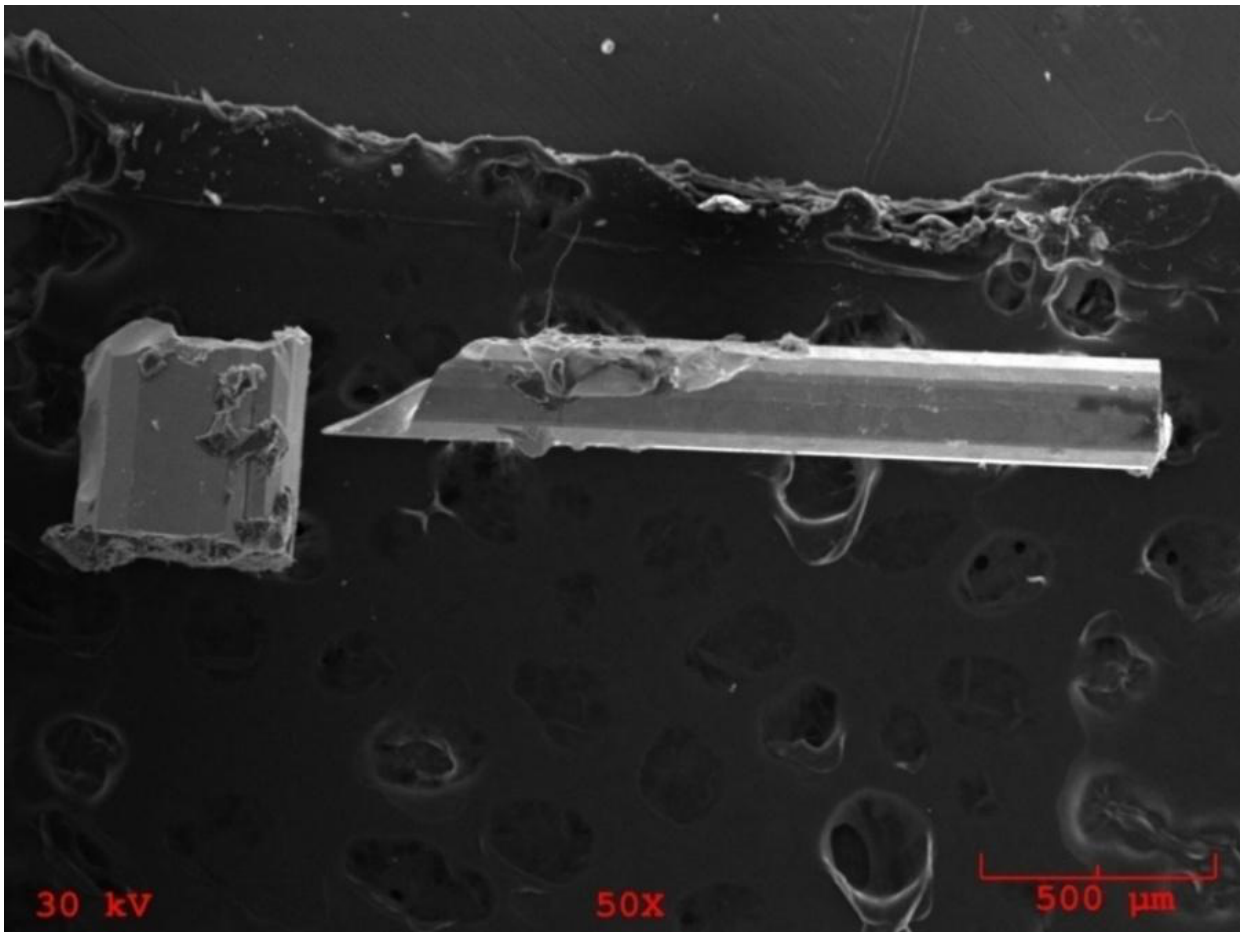

Figure 6.7 $Yb_6Mg_{11}Fe_2Si_5$ SEM image.

The structure of this compound is fairly complex (the expanded lattice is shown in Figure 6.8), having many crystallographic sites and some site mixing of Mg and Yb atoms. Crystallographic data for the compound is shown in Table 6.6. An interesting feature of this compound is the open cage present in the center of the unit cell (see Figure 6.9a). The local atomic environments are shown in Figure 6.9 while Table 6.5 displays the interatomic bond lengths. It might be possible to fill this cage with guest atoms, like hydrogen, but this compound is very heavy (FW = 1557.8 g/mol) so its application to hydrogen storage would be very limited.

Table 6.5 Crystallographic data for $Yb_6Mg_{11}Fe_2Si_5$.

Space group	*P4/mbm* (no. 127)
Data collection temperature, K	296
Cell parameter, Å	$a = b = 13.3379(14)$ $c = 4.0877(6)$
V, Å^3	727.20(15)
Z	4
Density (calc.), g cm^{-3}	7.311
μ, mm^{-1}	53.006
Data collection range, deg.	$2.16 < \theta < 42.00$
Reflections collected	9389
Independent reflections	1438 [$R_{int} = 0.1823$]
Parameters refined	38
R_1[a)], wR_2 [b)] [$F_o > 4\sigma F_o$]	0.0687, 0.1802
R_1, wR_2 (all data)	0.0912, 0.1853
Largest diff. peak and hole [e/Å^3]	12.142 and –12.594
Goodness-of-fit	1.648

[a)] $R_1 = \Sigma \| F_o | - | F_c \| / \Sigma | F_o \|$.

[b)] w$R_2 = [\Sigma w(F_o^2 - F_c^2)^2 / \Sigma w(F_o^2)^2]^{1/2}$, $w = [\sigma^2(F_o^2) + (A \cdot p)^2 + B \cdot p]^{-1}$; $p = (F_o^2 + 2F_c^2)/3$; A = 0.0067, B = 0.

Table 6.6 Wyckoff sites, atomic coordinates, equivalent isotropic displacement parameters [Å^2] and occupancies of $Yb_6Mg_{11}Fe_2Si_5$.

	Wyckoff Site	Atomic Coordinates	U_{eq}	Occupancy
Yb1	*8j*	0.17913(3), 0.06028(5), 1/2	0.0063(4)	0.90973
Yb2	*4h*	0.66679(5), 0.16679(5), 1/2	0.0078(7)	1
Fe1	*4h*	0.12212(2), 0.62212(1), 1/2	0.0053(4)	1
Si1	*8i*	0.09699(4), 0.18752(3), 0	0.0073(2)	1
Si2	*2c*	0, 1/2, 1/2	0.0119(2)	1
Mg1	*8j*	0.17913(3), 0.06028(5), 1/2	0.0063(4)	0.09027
Mg2	*8i*	0.34955(4), 0.00696(4), 0	0.0026(2)	1
Mg3	*4h*	0.20355(3), 0.70355(3), 0	0.0036(1)	1
Mg4	*2a*	0, 0, 0	0.0076(3)	1

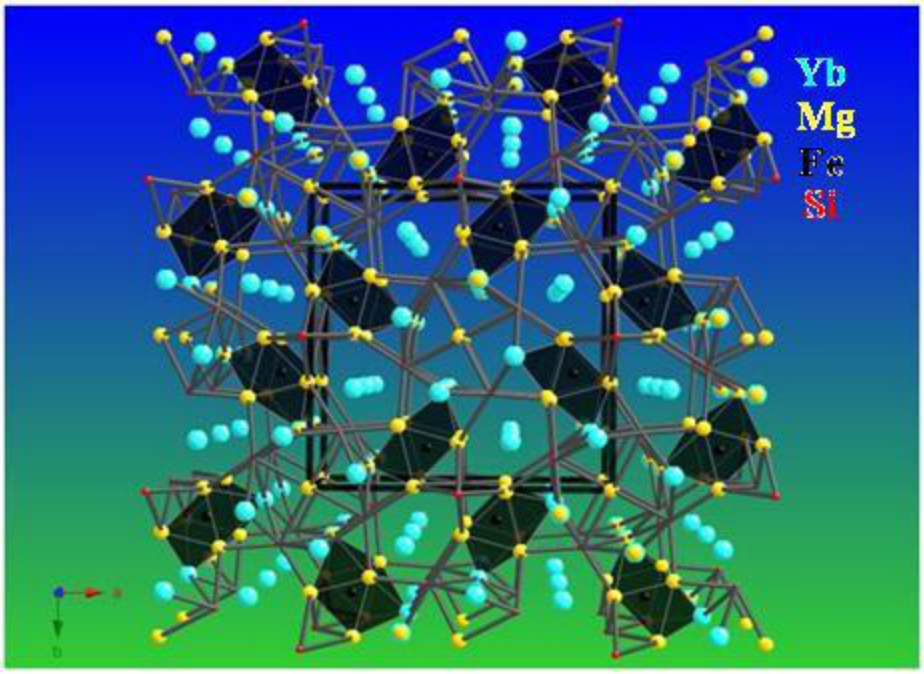

Figure 6.8 Expanded lattice of $Yb_6Mg_{11}Fe_2Si_5$ with tetragonal unit cell outlined in black.

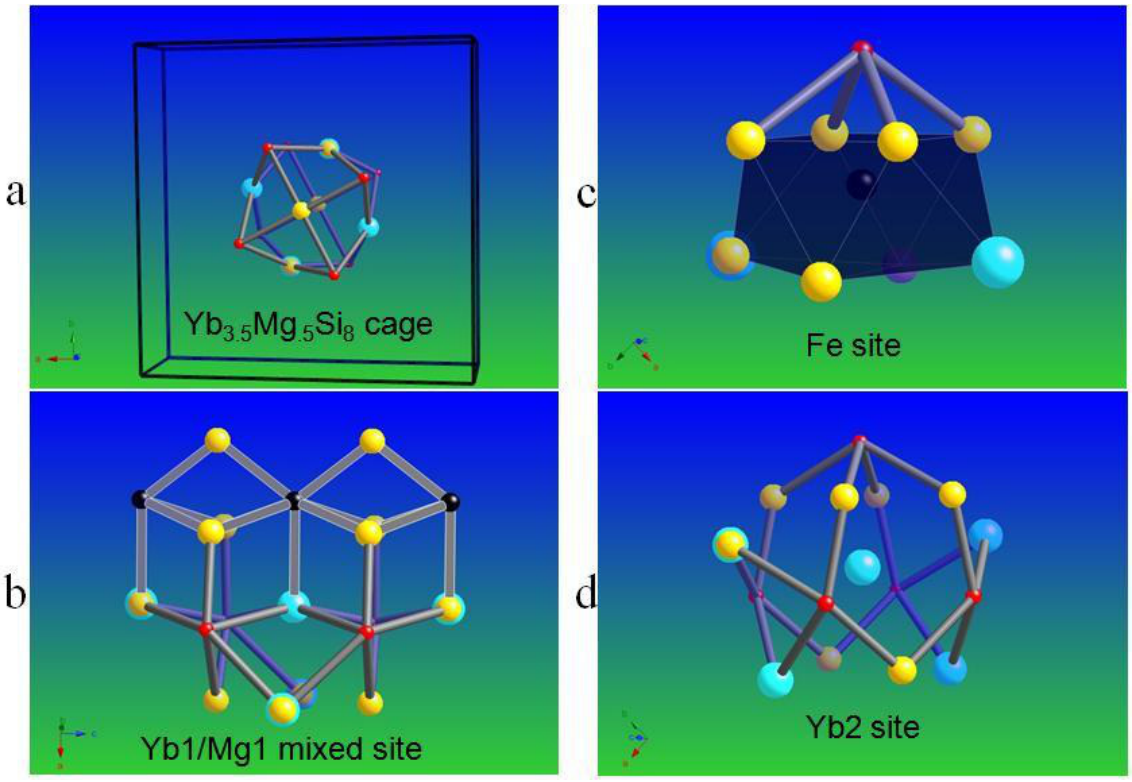

Figure 6.9 Central $Yb_{3.5}Mg_5Si_8$ open cage inside unit cell (a); Yb/Mg mixed site coordination (b); Fe centered Mg/Yb polyhedron (c); second Yb site local environment (d).

Table 6.7 Interatomic bond lengths in $Yb_6Mg_{11}Fe_2Si_5$.

	Yb1/Mg1	**Yb2**	**Mg6**	**Mg7**	**Mg8**
Fe3	2.7761 Å	*	2.5567 Å	2.5844 Å	*
Si4	2.8737 Å	2.9698 Å	2.6689 Å	2.5677 Å	2.816 Å
Si5	*	3.1461 Å	*	2.8657 Å	*

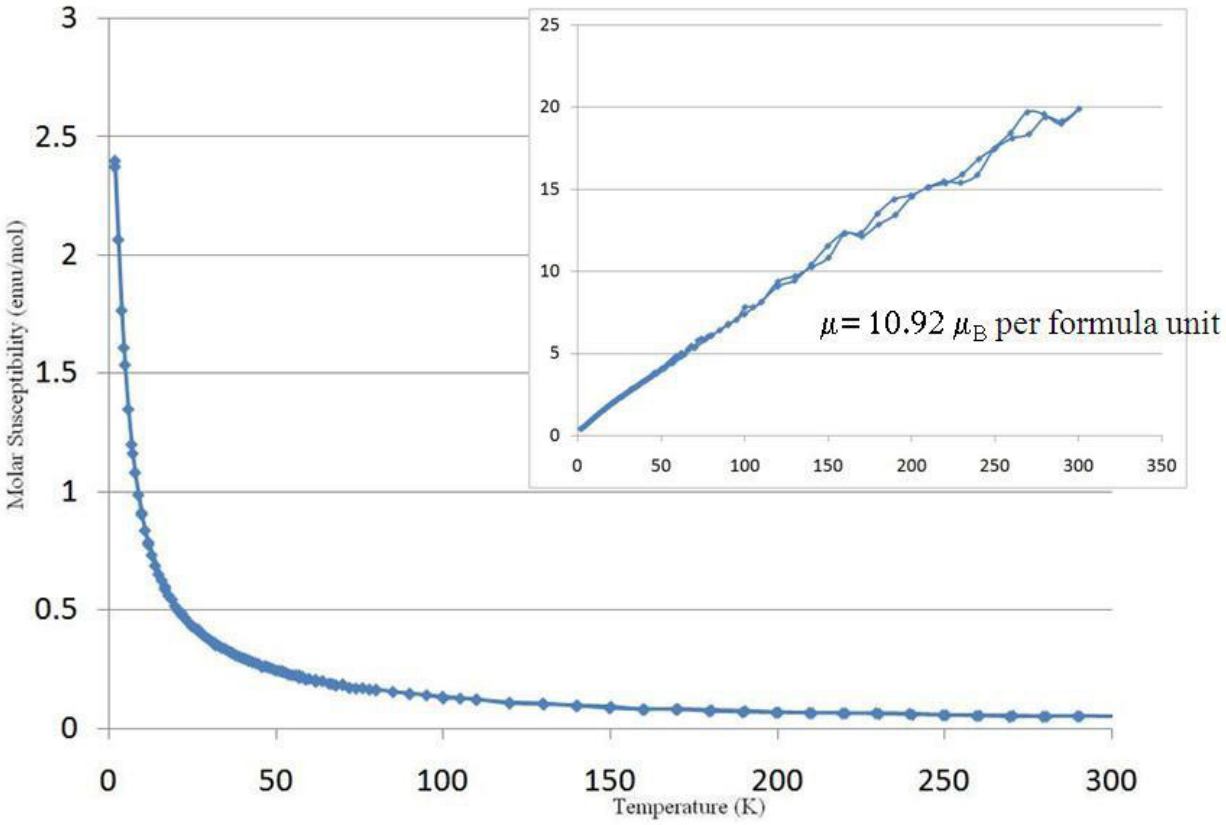

Figure 6.10 χ vs. T magnetic susceptibility plot (collected at 100 G) for $Yb_6Mg_{11}Fe_2Si_5$ with 1/ χ vs. T plot and magnetic moment per formula unit shown in inset.

Mg-Al Flux Exploratory Strategies

Exploratory synthesis has indicated that the Mg-Al flux mixture is a particularly effective solvent for growth of Mg-containing intermetallics. Reactions in the flux have produced some interesting phases that are difficult or impossible to synthesize using traditional solid state methods. The reactions explored with Mg-Al fluxes produced Mg and/or Al-containing compounds that were not formed when pure Mg or Al fluxes were used. The notoriously unpredictable synthetic nature of elemental Mg, combined with the highly reactive metalloid behavior of Al, create a very reactive crystal growth environment. The use of the Mg-Al mixture inhibits the growth of known binary phases such as Mg_2Ni and $CaAl_2$; reactions usually yield ternary or quaternary single crystals or simply nothing at all. Reactions in pure Mg flux have a tendency to favor thermodynamically stable binary phases that consume reactants and do not allow for the growth of more interesting ternary or quaternary compounds. Products are also often bulk polycrystalline materials, not clean single crystals. This is not the case for the Mg-Al flux mixture reactions. The Mg-Al binary phase diagram shows two phases (refer to Figure 1.8), Mg_2Al_3 and $Mg_{17}Al_{12}$. The crystallization of these phases occurs at low temperatures (~450 °C) and can be avoided by centrifuging well above this temperature.

The approach to exploratory synthesis using this system was to vary experimental factors (heating/cooling rates, flux ratios, reactants and centrifugation temperatures), while also incorporating large concentrations other elements into the flux to create ternary mixed fluxes of Mg-Al-X (X= Li, Ca, Zn, Ga, As, In, Sb, Pb, Bi). Most of the elements used to make the mixed fluxes have melting points near or below Mg and Al, and this enables the reactions to be centrifuged at 750 °C with a high probability that the flux is molten at that temperature. Ca, Ni, Cu and As have slightly higher melting points so these were used only in small amounts, maintaining the normal melting point of the Mg-Al binary flux.

Table 6.8 Melting points of elements used to make mixed fluxes with Mg.

Flux Element	Melting Point (°C)
Mg	650.0
Al	660.4
Ga	29.8
As	817.0
In	156.6
Sb	630.6
Bi	271.5

The Mg-Al or Mg-Al-X flux mixtures were used at fixed ratios for a batch with 12 individual reactions per batch. Li, B, C, Si, Ca, Ge, Sr, Sn, Y, Nb, Ba, 3d transition metals and lanthanides were used as reactants in the fluxes with the flux / reactant ratio always above 3 / 1 to ensure the presence of excess solvent. The systematic variation of synthesis procedure led to many reactions; the products were stored to stockpile a crystal bank. This crystal bank is being kept under protective Ar atmosphere for future characterization. Table 6.7 shows the possible reactions. Most of these reactions have been run and the products stored in the crystal bank, but more reaction options still have yet to be explored.

The broad eutectic region evident in the phase diagram for the Mg-Al system (refer to Figure 1.7)[30] allowed for the use of a Mg-rich, equal parts, or Al-rich flux to be employed. As expected, Mg-rich flux reactions usually yielded Mg-containing products, while Al-rich flux reactions yielded Al-containing products. The use of Mg-rich fluxes often yielded Mg-containing Zintl phases such as CaMgGe, CaMgSn and $Eu_8Mg_{18}Si_{13}$ for reactions with Group 14 elements. Synthesis of compounds on the border between the intermetallic and Zintl phase classifications represents a growing field in the search for materials with desirable electronic, magnetic and optical properties. The Zintl border can be hypothetically drawn vertically between Group 13 and Group 14. Compounds containing alkaline earth metals combined with elements from Group 13 usually form more electrically conductive metallic phases, while Zintl compounds of Group 14, 15 and 16 are usually semiconductors and insulators.[136,137]

Table 6.9 Possible reactions using Mg-X and Mg-Al-X fluxes (X=Li, Al, Ca, Ni, Cu, Zn, Ga, Ge, As, In, Sn, Sb, Pb, Bi). Starred reactions have been explored.

Reaction	Ratio	Comment
Mg-Al-X and mixed flux		
Mg-Al-Ca-(Li,B,C,nitrides,Si,TM,RE)*	15-15-4-2	Not fully explored
Mg-Al-Si-(Li,B,C,nitrides,Ca,TM,RE)*	15-15-2-2	Not fully explored
Mg-Al-Ca-Si-(Li,B,C,nitrides,TM,RE)*	15-15-3-3-2	Not fully explored
Mg-Al-MgB2-(Li,C,nitrides,Si,Ca,TM)	15-15-1-2	
Mg-Al-Li-(B,C,nitrides,Si,Ca,TM)*	15-15-4-2	Not fully explored
Mg-Al-Ca-Si-Li*	15-15-3-3-4	Air sensitive products
Mg-Al-Ca-Si-Li-(B,C,nitrides,TM,RE)*	15-15-3-3-4-2	Air sensitive products
Mg-X		
Mg-Mg3N2-(Li,B,C,Si,Ca,TM)*	20-2-1-1	Some rxns exploded
Mg-TiN-(Li,B,C,Si,Ca,TM)	20-1-1-1	
Mg-Si3N4 -(Li,B,C,Si,Ca,TM)	20-1-1	
Mg-Y-(Li,B,C,nitrides,Si,Ca,TM)*	20-2-1	Not fully explored
Mg-Sn-(Li,B,C,nitrides,Si,Ca,TM)*	20-2.14-1	Reactive with crucible
Mg-Li-(B,C,nitrides,Si,Ca,TM)*	20-4-1	Air sensitive products
Mg-Li-(B,C,nitrides,Si,Ca,TM)*	15-10-1	Air sensitive products
Mg-As-(Li,B,C,nitrides,Si,Ca,TM)*	30-1.8-1	Not fully explored
Mg-Ga-(Li,B,C,nitrides,Si,Ca,TM)*	20-10-2	Reactive with crucible
Mg-In-(Li,B,C,nitrides,Si,Ca,TM)*	30-5-2	
Mg-Al eutectic ratio variations		
Mg-Al-(Li,B,C,nitrides,Si,Ca,TM,RE)*	(5-25)-(5-25)-3	Not fully explored
Mg-B rich rxns		
Mg-Al-B-(Li,C,nitrides,Si,Ca,TM)*	15-15-3-1	Few crystals
Mg-Al-Li-B-(C,nitrides,Si,Ca,TM)	15-15-4-3-1	
Mg-Al-(Ni,Cu,Zn)-B-(Li,C,nitrides,Si,Ca,TM)	15-15-(4-8)-3-1	
Mg-TM rich rxns		
Mg-(Ni,Cu,Zn)-(Li,B,C,nitrides,Si,Ca,TM)*	30-(4-8)	Few crystals
Mg-Al-(Ni,Cu,Zn)-(Li,B,C,nitrides,Si,Ca,TM)	15-15-(4-8)-1	
Mg-Al-Si-(Ni,Cu,Zn)-(Li,B,C,nitrides,Ca,TM)	15-15-2-(4-8)-1	
Mg-Al-Si-Ca-(Ni,Cu,Zn)-(Li,B,C,nitrides,TM)	15-15-3-3-(4-8)-1	
Electron/Hole Doping Rxns		
Mg-Al-(Ga,In,As,Sb,Bi)-(Li,B,C,nitrides,Si,Ca,TM)*	15-(8-15)-2	Not fully explored
Mg-Al-(Ga,In,As,Sb,Bi)-(Si,Ge,Sn)-Ca*	15-(8-15)-3-3	Not fully explored
Mg-Al-(Ca,Sr,Ba)-(Si,Ge,Sn) variations		
Mg-Al-Ca-(Ge,Sn)*	15-15-3-3	
Mg-Al-Ca-(Ge,Sn)-(Li,B,C,nitrides,Si,Ca,TM)*	15-15-3-3-1	Not fully explored
Mg-Al-(Ca,Sr,Ba)-(Si,Ge,Sn)*	15-15-3-3	Not fully explored
Mg-Al-(Ca,Sr,Ba)-(Li,B,C,nitrides,Si,Ca,TM)*	15-15-3-1	Not fully explored

By using either Group 13 or 15 elements to make the mixed flux, electron and hole doped products were targeted. Low concentration substitution of the Group 14 element in a compound for either a Group 13 (hole doped) or Group 15 (electron doped) element was the target effect of these mixed flux reactions. Doping of these structures with elements that change the population of electrons near the Fermi level will have effects on the electronic properties of the compounds. For example, a reaction targeting hole doping of Mg / Al / Ga / Ca / Ge led to the growth of significantly larger crystals than the reaction of Mg / Al / Ca / Ge, while showing no measurable incorporation of Ga into the final CaMgGe product crystals. The possibility of slight Ga doping in the CaMgGe crystals could have effects on the electronic properties of this compound and this would be evident in resistivity, heat capacity or magnetization measurements.

The Crystal Bank

The purpose of leaving behind a crystal bank was to enable a large amount of flux reactions to be run using a synthesis that was producing interesting phases. Initial screening of all samples and future extensive characterization of interesting phases will be conducted. Although many reactions were run without initial characterization, the batches had significant variations between them (such as reaction stoichiometry and heating profile) and this ensured that the same products would not be simply reproduced. Even from observation of the macroscopic morphology of the products, it was evident that many different phases were present (some reactions yielded rods, and others blocks). The crystal bank will serve as a starting point for future projects. For example, the synthesis of $Eu_8Mg_{18}Si_{13}$ occurred from an initial reaction which gives future researchers a starting point to begin optimization or extensive synthesis variations to search for similar intermetallics or related analogs.

Incorporation of the lightest elements possible for hydrogen storage was one of the main focuses of the reactions comprising the crystal bank. Li, B, C and Si were used in many of the reactions to search for ways to incorporate these elements into intermetallics. Working with these elements was difficult for various reasons (C and B are insoluble in many fluxes). Current work with lightweight elements has shown that they can achieve impressive hydrogen storage

capacities, but usually this is the case of liquid solutions, not intermetallics. Work to synthesize materials containing these elements will continue with emphasis on fluxes that can solvate Li, B, C and Si.

The crystal bank also contains many reactions with mixed fluxes of Mg and Al with Group 13, 14, and 15 elements. Early reactions showed that these combinations of elements had a uniquely high reactivity. Most of the Group 13, 14 and 15 elements have good solubilities in Mg and Al, thus allowing feasible centrifugation temperatures. Additionally, the use of the Group 13, 14, and 15 elements in the mixed fluxes allowed for better solvation of Li, B, C and Si.

Lastly, reactions including lanthanides were included in the crystal bank to search for interesting compounds not necessarily targeted at hydrogen storage. The Mg-Al flux had good reactivity with many of the lanthanides, but these reactions required special care beyond synthesis. All reactions of this kind were stored under inert atmosphere to ensure there would be no decomposition. Despite the extra work involved in handling and storing the product crystals, these reactions proved to be a worthwhile effort, and may yield compounds with interesting magnetic properties.

CHAPTER 7

FINAL CONCLUSIONS

Mg-based fluxes were used for exploratory synthesis for new phases and analog compounds. Products were characterized for structure, composition, electronic, transport and hydrogen storage properties. Many of the characterization techniques required for exploratory materials research were used. Emphasis was placed on creating a usable hydrogen storage material will enable future diminishment of dependence on fossil based fuels. Synthesis of Mg-based materials for hydrogen storage was the main goal and many challenges associated with producing these types of materials were faced.

In order to screen newly synthesized products, it was necessary to construct an apparatus to activate and hydrogenate the materials, as well as conduct volumetric measurements. A high pressure gas controlling and measurement system was developed performs temperature and pressure related tasks. This high pressure system is the only one of its kind available in the FSU chemistry department. It is constructed mainly of stainless steel and operates by computer control with LabView programming. The system can expose samples to conditions from 0-2500 PSIG and 25-700 °C with several types of gases (H_2, CO_2, O_2, N_2, etc.).

Among the materials which were synthesized and tested in the volumetric system, the Mg-Ca-Si system yielded two interesting phases, $Ca_2Mg_{4-x}Si_x$ and CaMgSi. Despite their similar elemental composition, these compounds have very different properties. $Ca_2Mg_{4-x}Si_x$ can reversibly absorb up to 4 weight percent hydrogen depending on the amount of Si incorporated. The lightweight of this compound make it a viable candidate for application in solid state hydrogen storage systems, like those necessary for PEM fuel cells. Its structure is analogous to hexagonal Mg_2Ca, with one of the Mg sites being partially occupied by Si. Incomplete substitution of Si into the structure has a negative effect on the hydrogen storage capacity, lowering it to 1.9 weight percent. Full substitution of Mg for Si results in the highest hydrogen

storage capacity and this was best achieved by stoichiometric melting and annealing of the elements.

Unlike $Ca_2Mg_{4-x}Si_x$, CaMgSi has a completely different structure type and properties. CaMgSi is based on the Ca_2Si orthorhombic structure having one of the Ca sites fully occupied by Mg. Synthesized from a Mg-Al flux, CaMgSi always had full substitution of Mg and there was no phase width observed (as was seen in $Ca_2Mg_{4-x}Si_x$). Stoichiometric melts to produce this phase resulted in multi-phase polycrystalline products instead of the large single crystals obtained from the flux synthesis methods. CaMgSi shows an interesting metal-insulator transition at 50 K but has negligible hydrogen storage capacity. Both resistivity and magnetic susceptibility measurements show the transition and low temperature PXRD confirms structural distortion below 50 K.

The analogous compounds CaMgSi, CaMgGe and CaMgSn were all synthesized using flux methods. CaMgSi and CaMgGe have nearly the same unit cell parameters and their resulting transport and magnetic properties are also very similar. Additionally, low temperature susceptibility behavior stemming from anisotropic effects was observed for both the silicide and germainide analogs, but not the stannide. CaMgSn, having much larger unit cell parameters, displays very different transport and susceptibility behavior. Mg / Al flux proved most effective at synthesizing CaMgSi, while Mg / Ga and Mg / In fluxes were best for CaMgGe and CaMgSn, respectively.

The Mg-Al flux has proven a useful exploratory synthetic tool and will continue to be used for future reactions. Initial reactions have yielded two interesting phases, $Yb_6Mg_{11}Fe_2Si_5$ and $Eu_8Mg_{18}Si_{13}$; the latter has Curie-Weiss magnetic behavior and ferromagnetic ordering at 10 K. This was the first discovery of the $Yb_6Mg_{11}Fe_2Si_5$ phase and its preliminary characterization. $Eu_8Mg_{18}Si_{13}$ is an analog of a previously reported compound, $Ba_5Mg_{18}Si_{13}$. Future reactions with the Mg-Al flux will focus on the use of the most lightweight elements possible for creating potential hydrogen storage materials. The use of these extremely lightweight elements would allow for materials with maximum gravimetric hydrogen storage capacity as well as reduced cost. In addition, lanthanides will be used in the Mg-Al flux in efforts to create interesting materials that are not necessarily for use in hydrogen storage, but instead, for electronic or magnetic materials. Ternary and quaternary mixed fluxes including Mg were created which were targeted at increasing the solubility of certain reactants, especially Li, B, C and Si. The

reactions run in the Mg-Al flux have been stockpiled and stored appropriately to create a crystal bank which was organized for future extensive characterization.

LIST OF REFERENCES

[1] Züttel, A. *Naturwissenschaften* **2004**, *91*, 157-172

[2] Uttara, S.; Norton, M.G. *J. Mater. Sci.* **2008**, 43, 5395-5429

[3] Sakintuna, B.; Lamari-Darkrim, F.; Hirscher, M. *Int. J. of Hyd. Energy* **2007**, *32*, 1121-1140

[4] Klyamkin, S.N. *Russian J. Gen. Chem.* **2007**, *77*, 712-720

[5] Wikipedia Internet Encyclopedia, http://en.wikipedia.org/ **2009**

[6] Kojima, Y.; Kawai, Y.; Akihiko, K.; Suzuki, N.; Haga, T.; Hioki, T.; Tange, K. *J. Alloys and Comp.* **2006**, 421, 204-208

[7] Henwood, D.; Carey, J.D. *Phys. Rev. B* **2007**, 75, 245413

[8] Henwood, D.; Carey, J.D. *Phys. Rev. B* **2007**, 76, 049901(E)

[9] Nikitin, A.; Li, X.L.; Zhang, Z.Y., *et. al. Nano Letters* **2008**, Vol.8, Iss.1, 162-167

[10] Dinca, M.; Long, J.R. *Angew. Chem. Int. Ed.* **2008**, 47, 6766 – 6779

[11] Kaye, S.S.; Long, J.R. *Catalysis Today* **2007,** 120, 311–316

[12] Hydrogen Storage Challenges for Mobility Symposium *Center for Hydrogen Research, Aiken, SC, USA* I.D.# 2006S05, **Dec. 6-7, 2006**, www.sae.org/hydrostorage

[13] Schlapbach, L.; Züttel, A. *Nature* **2001**, 414, p.353

[14] Silberberg, M. *CHEMISTRY The Molecular Nature of Matter and Change, Third Edition* **2003**, © McGraw-Hill Companies, Inc., Ch.5

[15] Texaco Ovonic Hydrogen Storage Systems, LLC., **2003**, www.h2fc.com/Newsletter/PDF/Advances%20of%20Solid%20Hydrogen%20Storage%20Systems.pdf

[16] Morinaga, M.; Yukawa, H.; Nakatsuka, K.; Takagi, M. *J. of Alloys and Comp.* **2002,** 330-332, 20-24

[17] Wallace, W.E.; Karlicek, Jr.; R.F., Imamura, H. *The J. of Phys. Chem.* **1979**, Vol. 83, No. 13

[18] Hotta, H.; Abe, M.; Kuji, T.; Uchida, H. *J. of Alloys and Comp.* **2007**, 439, 221-226

[19] Kinaci, A.; Aydinol, M.K. *Int. J. or Hyd. Ener.* **2007**, 32, 2466-2474

[20] Haussermann, U.; Blomqvist, H.; Noreus, D. *Inorg. Chem.* **2002**, 41, 3684-3692

[21] Orimo, S.; Fujii, H. *Appl. Phys. A* **2001**, 72, 167-186

[22] Tsushio, Y.; Akiba, E. *J. of Alloys and Comp.* **1998**, 269, 219-223

[23] U.S. Naval Research Laboratory website, "Crystal-Lattice Structures" Database, **2008**, http://cst-www.nrl.navy.mil/lattice/index.html

[24] U.S. Department of Energy website, "DOE Hydrogen Storage Goals", **2009**, http://www.hydrogen.energy.gov/storage.html

[25] Fisk, Z.; Remeika, J. P. *Handbook of the Physics and Chemistry of Rare Earths,* **1989,** G. Schneider and Eyring. Vol. 12, Chapter 81

[26] Kanatzidis, M.G., *et. al. Angew. Chem. Int. Ed.* **2005**, 44, 6996-7023

[27] Fisher, I.R.; Kramer, M.J.; Islam, Z.; Wiener, T.A.; Kracher, A.; Ross, A.R.; Lograsso, T.A.; Goldman, A.I.; Canfield, P.C. *Mat. Sci. and Eng.* **2000**, 294-296, 10-16

[28] Fisher, I.R.; Islam, Z.; Panchula, A.F.; Cheon, K.O.; Kramer, M.J.; Canfield, P.C.; Goldman, A.I. *Philisophical Magazine B* **1998**, Vol.77, No.6, 1601-1615

[29] Kanatzidis, M.G.; Poeppelmeier, K.R., Organizers *Progress in Solid State Chem.* **2007**, 36, 1-133

[30] Massalski, T.B. *Binary Alloy Phase Diagrams, Second Edition*, ASM International **1990**, Materials Park, Ohio, , 1 & 2

[31] Latturner, S.E.; Bilc, D.; Mahanti, S.D.; Kanatzidis, M.G. *Chem. Mater.* **2002**, 14, 1695-1705

[32] Latturner, S.E.; Kanatzidis, M.G. *Inorg. Chem.* **2008**, 47, 2089-2097

[33] Latturner, S.E.; Kanatzidis, M.G. *Inorg. Chem.* **2002**, 41, 5479-5486

[34] Wu, X.; Latturner, S.E.; Kanatzidis, M.G. *Inorg. Chem.* **2006**, 45, 5358-5366

[35] Latturner, S.E.; Kanatzidis, M.G. *Inorg. Chem.* **2004**, 43, 2-4

[36] Latturner, S.E.; Bilc, D.; Mahanti, S.D.; Kanatzidis, M.G. *Inorg. Chem.* **2003**, 42, 7959-7966

[37] Mathieu, J.; Achey, R.; Park, J.H.; Purcell, K.M.; Tozer, S.W.; Latturner, S.E. *Chem. Mater.* **2008**, 20, 5675-5681

[38] Benbow, E.M.; Latturner, S.E. *J. of Solid State Chem.* **2006**, 179, 3989-3996

[39] Stojanovic, M.; Latturner, S.E. *J. of Solid State Chem.* **2007**, 180, 907-914

[40] Benbow, E.M.; Dalal, N.S.; Latturner, S.E. *J. of Amer. Chem. Soc.* **2009**, 131, 3349-3354

[41] Goldstein, J. *Scanning electron microscopy and X-ray microanalysis*. **2003** Kluwer Adacemic/Plenum Pulbishers, p. 689

[42] Egerton, R. F. *Physical Principles of Electron Microscopy: An Introduction to TEM, SEM, and AEM*. **2005** Springer, p. 202

[43] West, A.R. *Basic Solid State Chemistry: Second Edition.* John Wiley & Sons, LTD, **1999** Chichester, West Sussex, England

[44] Quantum Materials Group at NHMFL website, http://neutron.magnet.fsu.edu/x-ray_scattering.html

[45] Huheey, J.E.; Keiter, E.A.; Keiter, R.L. *Inorganic Chemistry, Principles of Structure and Reactivity, Fourth Edition* © **1993** HarperCollins College Publishers

[46] Quantum Design website, © **2009** Quantum Design, http://www.qdusa.com/

[47] Lachawiec, A.J., Jr.; DiRaimondo, T.R.; Yang, R.T. *Rev. of Sci. Instr.* **2008**, 79, 063906

[48] Muthukumar, P.; Maiya, M.P.; Murthy, S.S. *Int. J. of Hyd. Energy* **2005**, 30, 879-892

[49] Checchetto, R.; Trettel, G.; Miotello, A. *Meas. Sci. Technol.* **2004**, 15, 127-130

[50] Friedrichs, O.; Borgschulte, A.; Züttel, A. *Int. J. of Hyd. Energy* **2008**, 33, 5606-5610

[51] Meyer, G.; Larachette, P.A.; Baruj, A.; Castro, F.J.; Lacharmoise, P.; Zacur, E.; Talagañis, B.A. *Rev. of Sci. Instr.* **2007**, 78, 023903

[52] Blach, T.P.; Gray, E.MacA. *J. of Alloys and Comp.* **2007**, 446-447, 692-697

[53] Urretavizcaya, G.; Fuster, V., Castro, F.J. *Rev. of Sci. Instr.* **2005**, 76, 073902

[54] Blackman, J.M.; Patrick, J.W.; Snape, C.E. *Carbon* **2006**, 44, 918-927

[55] Zhang, C.; Lu, X.; Gu, A. *Int. J. of Hyd. Energy* **2004**, 29, 1271-1276

[56] Dantzer, P.; Millet, P. *Rev. of Sci. Instr.* **2000**, Vol.71, No.1, 142-153

[57] Hiden Isochema website, © Hiden Isochema **2009** Registered in England, No. 2865845. Registered Office: 420, Europa Boulevard, Warrington, WA5 7UN. Hiden Isochema is a subsidiary of Hiden Analytical Ltd., http://www.hidenisochema.com/

[58] Hy-Energy Hydrogen Sciences website, © Hy-Energy LLC. **2005,** http://www.hy-energy.com/index.html

[59] Broom, D.P. *Int. J. of Hyd. Energy* **2007**, 32, 4871-4888

[60] Broom, D.P.; Moretto, P. *J. of Alloys and Comp.* **2007**, 446-447, 687-691

[61] Latroche, M. *Z. Kristallogr.* **2008**, 223, 666-673

[62] Yartys, V.A.; Vajeeston, P.; Riabov, A.B.; Ravindran, P.; Denys, R.V.; Maehlen, J.P.; Delaplane, R.G.; Fjellvåg, H. *Z. Kristallogr.* **2008**, 223, 674-689

[63] Cermak, J.; Kral, L. *Acta Mater.* **2008**, 56, 2677-2686

[64] Wu, H. *ChemPhysChem* **2008**, 9, 2157-2162

[65] Oriani, R.A. *ICCF4, Fourth Int. Conf. on Cold Fusion* **1993**, Lahaina, Maui: Electric Power Reseach Institute 3412 Hillview Ave., Palo Alto, CA 94304, USA

[66] Borgschulte, A.; Gremaud, R.; Griessen, R. *Phys. Rev. B* **2008**, 78, 094106

[67] Akiba, E. *Current Opinion in Solid State and Materials Sci.* **1999**, 4, 267-272

[68] Yukawa, H.; Nakatsuka, K.; Morinaga, M. *Solar Energy Mat. & Solar Cells* **2000**, 62, 75-80

[69] Yvon, K. *Z. Kristallogr.* **2003**, 218, 108-116

[70] Sandia National Laboratories Hydride Materials Listing Database **2002**, http://hydpark.ca.sandia.gov/MaterialsFrame.html

[71] Ruoff, A.L. *Introduction to Materials Science* © **1972** Prentice-Hall, Inc., Englewod Cliffs, N.J.

[72] Révész, A.; Fátay, D.; Spassov, T. *J. Mater. Res.* **2007**, Vol.22, No.11, 3144-3151

[73] Larsson, P.; Araujo, C.M.; Larsson, J.A.; Jena, P.; Ahuja, R. *PNAS* **2008**, Vol.105, No.24, 8227-8231

[74] FindIt, Version 1.4.4, FIZ/NIST, ICSD Database Ver. 2008-1

[75] Gruehn, R.; Glaum, R. *Angew. Chem. Int. Ed.* **2000**, 39, 692-716

[76] Stojanovic, M. *Dissertation: Synthesis of New Intermetallics in Metal Fluxes* **2008**

[77] U.S. DOE EERE Hydrogen, Fuel Cells and Infrastructure Program, *Multi-Year Research, Development and Demonstration Plan for 2005-2015*, **2007**

[78] Tang, F.; Parker, T.; Li, H.-F.; Wang, G.-C.; Lu, T.-M.; *J. of Nanoscience and Nanotechnology* **2007,** Vol. 7 3239-3244

[79] Stampfer, Jr., J. F.; Holley, Jr., C. E.; Suttle, J. F. *Contribution from The University of California, Los Alamos National Lab and the Department of Chemistry, University of New Mexico* **1960** Vol. 82 3504-3508

[80] Xie, L.; Liu, Y.; Wang, Y.T.; Zheng, J.; Li, X.G. *Acta Materialia* **2007,** 55 4585-4591

[81] Jongh, P.; Wagemans, R.; Eggenhuisen, T.; Dauvillier, B.; Radstake, P.; Meeldijk, J.; Gues, J.; Jong, K. *Chem. Matter* **2007,** 19 6052-6057

[82] Yin, Y.; Zhang, G.; Xia, Y. *Adv. Funct. Mater.* **2002,** 12 No. 4

[83] Zuttel, A.; Wenger, P.; Rentsch, S.; Sudan, P.; Mauron, Ph.; Emmenegger, Ch. *J. Power Sources* **2003,** 118, 1-7

[84] Fernandez, I.; Gennari, F.C.; Meyer, G.O. *J. Alloys and Comp.* **2008,** 462, 119-124

[85] SAINT, V. 6.02a, **2000,** Bruker AXS Inc., Madison, WI

[86] Sheldrick, G.M. SHELXTL NT/2000, V. 6.1, **2000,** Bruker AXS Inc., Madison, WI

[87] Villars, P. *Pearson's Handbook Desk Edition, Vol 1 and 2*, **1997,** Materials Park, OH 44073

[88] Nesper, R.; Currao, A.; Wengert, S. *Chemistry-A European Journal* **1998,** 4, 2251-2257

[89] Axel, H.; Eisenmann, B.; Schafer, H.; Weiss, A. *Z. Naturforsch.* **1969**, *24b*, 815-817

[90] Zmiy, O.F.; Gladyshevskii, E.I. *Visn. Lviv. Derz. Univ, Se Khim.* **1969**, *11*, 38-39

[91] Grobner, J.; Chumak, I.; Schmid-Fetzer, R. *Intermetallics* **2003**, *11*, 1065-1074

[92] Miyoshi, M.; Kinoshita, K.; Aoki, M.; Ohba, N.; Miwa, K.; Noritake, T.; Towata, S. *J. of Alloys and Comp*. **2007,** 446-447, 15-18

[93] Vojtech, D.; Novak, P.; Cizkovsky, J.; Knotek, V.; Prusa, F. *J. of Physics and Chemistry of Solids* **2007,** 68, 813-817

[94] Rielly, J.J.; Wiswall, R.H.; Waide, C.H. *Report TEC-75/001* **1974**, U.S. Energy Research and Development Admin. Brookhaven N.L. 1-84

[95] Semenenko, K.N.; Verbetsky, V.N.; Kochukov, A.V.; Sytnikov, A.N. *Bulletin of Moscow University, Chemistry Series* **1983,** 24, No. 1, 16-26

[96] Verbetsky, V.N.; Sytnikov, A.N.; Semenenko, K.N. *Russian Journal of Inorganic Chemistry* **1984,** 29, No. 3, 622-624

[97] Semenenko, K.N.; Verbetsky, V.N.; Sytnikov, A.N. *Russian Journal of Inorganic Chemistry* **1984,** 25, No. 5, 509-512

[98] Wu, H.; Zhou, W.; Udovic, T.J.; Rush, J.J. *J. of Alloys and Comp.* **2007**, 446-447, 101-105

[99] Avedesian, M.; Baker, H. *Magnesium and Magnesium Alloys*, **1998,** ASM International, Materials Park

[100] Kim, J.M.; Seong, K.D.; Jun, J.H.; Shin, K.; Kim, K.T.; Jung, W.J. *J. Alloys Compd.* **2007**, *434-435*, 324-326

[101] Park, S.S.; Bae, G.T.; Kang, D.H.; Jung, I.H.; Shin, K.S.; Kim, N.J. *Scripta Mater.* **2007**, 793-796

[102] Ben-Hamu, G.; Eliezer, D.; Shin, K.S. *Mat. Sci. Eng. A* **2007**, *447*, 35-43

[103] Kim, J.J.; Kim, D.H.; Shin, K.S.; Kim, N.J. *Scripta Mater.* **1999**, *41*, 333-340

[104] Ai, Y.; Luo, C.P.; Liu, J. *Acta Mater.* **2007**, *55*, 531-538

[105] Hosono, T.; Kuramoto, M.; Matsuzawa, Y.; Momose, Y.; Maeda, Y.; Matsuyama, T.; Tatsuoka, H.; Fukuda, Y.; Hashimoto, S.; Kuwabara, H. *Applied Surf. Sci.* **2003**, *216*, 620-624

[106] Carbonneau, Y.; Couture, A.; Van Neste, A.; Tremblay, R. *Metal. Mater. Trans. A* **1998**, *29A*, 1759-1763

[107] Fisk, Z.; Canfield, P.C. *Philos. Mag*. **1992**, *65*, 1117-1123

[108] Imai, Y.; Watanabe, A.; Mukaida, M. *J. Alloys Compd.* **2003**, 358, 257-263

[109] Bisi, O.; Braicovich, L.; Carbone, C.; Lindau, I.; Iandelli, A.; Olcese, G.L.; Palenzona, A. *Phys. Rev. B.* **1989**, *40*, 10194-10209

[110] Ivanenko, L.I.; Shaposhnikov, V.L.; Filonov, A.B.; Krivosheeva, A.V.; Borisenko, V.E.; Migas, D.B.; Miglio, L.; Behr, G.; Schumann, J. *Thin Solid Films* **2004**, *461*, 141-147

[111] Lebegue, S.; Arnaud, B.; Alouani, M. *Phys. Rev. B* **2005**, *72*, 085103

[112] Corbett, J.D. *Angew. Chem. Int. Ed.* **2000**, *39*, 670

[113] Akselrud, L.G.; Zavalij, P.Y.; Grin, Y.; Pecharsky, V.K.; Baumgartner, B.; Wölfel, E. *Mater. Sci. Forum* **1993**, *133-136*, 335-351

[114] Petricek,V.; Dusek, M.; Palatinus, L. "Jana2000. The crystallographic computing system." **2000,** Institute of Physics, Praha, Czech Republic

[115] Jepsen, O.; Burkhardt, A.; Andersen, O. K. The Program TB-LMTO-ASA, version 4.7 **2000**; Max-Planck-Institut für Festkörperforschung: Stuttgart, Germany

[116] Whalen, J.; Greska, B.; Latturner, S.E. in preparation

[117] Latturner, S.E.; Bilc, D.; Mahanti, S.D.; Kanatzidis, M.G. *Inorg. Chem.* **2009**, 48, 1346-1355

[118] Kauzlarich, S.M.; Condron, C.L.; Wassei, J.K.; Ikeda, T.; Snyder, G.J. *J. Solid State Chem.* **2009**, *182*, 240-245

[119] Landrum, G.A.; Hoffmann, R.; Evers, J.; Boysen, H. *Inorg. Chem.* **1998**, *37*, 5754-5763

[120] Kauzlarich, S. *Structure and Bonding of Zintl Phases and Ions.* **1996,** VCH Publishers: New York

[121] Rodewald, U.C.; Chevalier, B.; Pöttgen, R. *J. Solid State Chem.* **2007**, *180*, 1720-1736

[122] Fornasini, M.L.; Merlo, F.; Napoletano, M.; Pani, M. *J. Phase Equil.* **2002**, *23*, 57-60

[123] Ratai, E.; Augustine, M.P.; Kauzlarich, S.M. *J. Phys. Chem. B* **2003**, 107, 12573-12577

[124] Bohme, B.; Guloy, A.; Tang, Z.; Schnelle, W.; Burkhardt, U.; Baitinger, M.; Grin, Y. *J. Am. Chem. Soc.* **2007**, *129*, 5348-5349

[125] Stearns, L.A.; Gryko, J.; Diefenbacher, J.; Ramachandran, G.K.; McMillan, P.F. *J. Solid State Chem.* **2003**, *173*, 251-258

[126] Pouchard, M.; Cros, C.; Hagenmuller, P.; Reny, E.; Ammar, A.; Menetrier, M.; Bassat, J.M. *Solid State Sci.* **2002**, *4*, 723-729

[127] Latturner, S.E.; Iversen, B.B.; Sepa, J.; Srdanov, V.; Stucky, G. *Phys. Rev. B* **2001**, *63*, 125403

[128] Aydemir, U.; Ormeci, A.; Borrmann, H.; Bohme, B.; Zurcher, F.; Uslu, B.; Goebel, T.; Schnelle, W.; Simon, P.; Carrillo-Cabrera, W.; Haarmann, F.; Baitinger, M.; Nesper, R.; Von Schnering, G.H.; Grin, Y. *Z. Anorg. Allg. Chem.* **2008**, *634*, 1651-1661

[129] Roger, J.; Babizhetsky, V.; Cordier, S.; Bauer, J.; Hiebl, K.; Le Polles, L.; Ashbrook, S.E.; Halet, J.F.; Guerin, R. *J. Solid State Chem.* **2005**, *178*, 1851-1863

[130] Meintjes, E.M.; Danielson, J.; Warren, W.W. *Phys. Rev. B* **2005**, *71*, 035114

[131] Mori, T.; Shi, Y.; Tanaka, T. *J. Alloys Compd.* **2000**, *308*, 115-120

[132] Tamura, D.; Nagai, R.; Sugimoto, K.; Udono, H.; Kikuma, I.; Tajima, H.; Ohsugi, I.J. *Thin Solid Films* **2007**, 515, 8272-8276

[133] Pöttgen, R. *Z. Kristallogr.* **1996**, *211*, 884-890

[134] Hoffmann, R.-D.; Pöttgen, R. *Z. Kristallogr.* **2001**, *216*, 127–145

[135] Wu, H.; Zhou, W.; Udovic, T.J.; Rush, J.J. *J. Alloys Compd.* **2007**, *446-447,* 101-105

[136] Corbett, J.D. *Inorg. Chem.* **2000**, 39, 5178-5191

[137] Corbett, J.D. *Angew. Chem. Int. Ed.* **2000**, 39, 670-690

[138] Ganguli, A.K.; Guloy, A.M.; Corbett, J.D. *J. of Solid State Chem.* **2000**, 152, 474-477

[139] Nesper, R.; Wengert, S.; Zürcher, F.; Currao, A. *Chem. Eur. J.* **1999**, 5, No.11, 3382-3389

[140] Song, Y.K.; Varin, R.A. *Intermetallics* **1998**, 6, 43-59

[141] Holman, K.L.; Morosan, E.; Casey, P.A.; Li, L.; Ong, N.P.; Klimczuk, T.; Felser, C.; Cava, R.J. *Materials Res. Bull.* **2008**, 43, 9-15

[142] Yan, X.; Grytsiv, A.; Rogl, P.; Pomjakushin, V.; Xue, X. *J. of Alloys and Comp.* **2009**, 469, 152-155

BIOGRAPHICAL SKETCH

JEFFREY BRIAN WHALEN

Education

Ph.D. in Inorganic Chemistry – The Florida State University, Tallahassee, FL –August 8, 2009

B.S. in Biochemistry – The Florida State University, Tallahassee, FL –April 30, 2005

H.S. Diploma – Chaminade - Madonna College Prepatory (Fort Lauderdale, FL) –May 2001

Research and Working Experience

Graduate Research Assistant, Advised by Dr. Susan Latturner, (Summer 2005-Summer 2009) Dittmer Lab of Chemistry/Chemical Sciences Laboratory (DLC520/CSL4805) Florida State University, Tallahassee, FL

This work was collectively original research, apprenticeship and collaborative publication in a fully equipped chemical solid state synthesis lab mainly focusing on high temperature molten flux synthetic approaches. Responsibilities included appointment of lab safety monitor and directing undergraduate researchers.

Senior Graduate Teaching Assistant, (Fall 2006- Fall 2008), Undergraduate Recitation and Laboratory General Chemistry I & II (CHM1045, CHM1046), Advanced Analytical Chemistry/Instrumental Analysis Laboratory (CHM4130, CHM4135), Florida State University, Hoffman Teaching Labs of Chemistry, Tallahassee, FL

Prior to starting this work, experience with preparation, procedure and execution of various undergraduate teaching labs was obtained during work as lab technician.

Responsibilities included normal teaching assistant duties as well as new graduate teaching assistant training and staff training.

Lab Technician, (Summer 2004-Summer 2005), Florida State University, Hoffman Teaching Labs of Chemistry, Tallahassee, FL

This employment entailed OPS undergraduate work assisting the lab supervisor in complete responsibility for the running of various undergraduate teaching labs. Labs included: biochemistry, physical chemistry, analytical chemistry, general chemistry, inorganic chemistry.

Chemistry and Math Tutor, (Summer 2003-Summer 2009) Greater South Florida and Tallahassee, FL

Experiences in this work include student mentoring and one-on-one chemistry and mathematics teaching training. The 6 years time was a beneficial continuous opportunity to remain versed in all fundamentals of math and chemical science.

Technical Experience

Synthesis of New Intermetallics for Hydrogen Storage

Development of new synthetic methods and analysis of resulting Mg-based materials was the focus of this work. Target materials were lightweight, inexpensive intermetallics capable of hydrogen storage capacities sufficient for application in a hydrogen economy. High-temperature molten metal flux reactions, distillations, stiochiometric melts, reactive ball milling and microwave synthesis were techniques explored.

Analytical Methods

Structural, electronic, magnetic properties were characterized on flux grown alloys.

- Single Crystal and powder X-ray Diffractometry
- Thermogravimetric Analysis/ Differential Scanning Calorimetry
- Scanning Electron Microscopy/Energy Dispersive Spectrometry (EDS)

- Resistivity and Heat Capacity (PPMS)
- Magnetic Susceptibility (SQUID/MPMS)
- Magic Angle Spinning Nuclear Magnetic Resonance (MAS-NMR)
- Pressure-Composition-Temperature Isotherms (PCT/PCI)

Design, Construction and Calibration of a Gas Controlling and Measurement System

An original temperature and pressure gas control device was built in-lab to screen new products for hydrogen storage properties. The machine has computer controlled valves and pressure transducer/thermocouple data acquisition and signal conditioning.

Additional Skills

- Metal welding
- Glass manipulating and sealing
- NI LabView basic programming
- Internal combustion engine mechanics
- Fully integrated electronic and mechanical systems engineering
- Inert atmosphere drybox/glovebox techniques and procedures

Publications

1. J.B. Whalen, R. Stillwell, S. Tozer, S.E. Latturner, *MgCaSi crystals grown in Mg-Al flux displaying semiconducting to metal transition*, submitted 2009
2. J.B. Whalen, S.E. Latturner, *Synthesis, Characterization and Hydrogen Desorption from Alkaline Earth Silicide Composites*, submitted 2009
3. J.B. Whalen, B. Greska, S.E. Latturner, *Design, Construction and Calibration of a Gas Controlling and Measurement System*, submitted 2009
4. S.E. Latturner, J.B. Whalen, M. Stojanovic, *Growth of new intermetallics in alkaline earth metal fluxes*, Abstracts of Papers, 236th ACS National Meeting, Philadelphia, PA, USA, August 17-21, 2008

Presentations

1. *Energy Challenges: Power with Hydrogen*, Global Education Outreach for Science Engineering and Technology (GEOSET, geoset.info), Available on the web at: http://mediasite.oddl.fsu.edu/mediasite/Viewer/?peid=a451d4b681fb47a4ad41f957d4bcfd7a , February 2009, Florida State University, Tallahassee, FL

2. *Transition Metal Doped Magnesium Crystals Grown by Modified CVT*, May 2008, American Chemical Society: The Florida Annual Meeting and Exposition, Orlando Sun Resort and Convention Center, Kissimmee, FL

3. *New Metal Hydrides and a Hydrogen Sorption Measurement Machine*, October 2007, Preliminary Candidacy Exam, Florida State University, Tallahassee, FL

4. *Optimization of PEM Fuel Cells*, October 2006, Divisional Literature Review, Florida State University, Tallahassee, FL

5. *Synthesis of Mg Based Metal Hydrides*, February 2006, Divisional Initial Research Outlook, Florida State University, Tallahassee, FL

Posters

1. *Controlled Site Mixing of the $CaGa_4$ and $Mg_6Ni_{16}Si_7$ Systems: Design, Construction and Implementation of a Hydrogen Sorption Measurement Apparatus*, May 2007, North American Solid State Chemistry Conference, Texas A&M University, College Station, TX

2. *Exploration of Ca/Mg/X (X=Si, Ge, Sn) Systems Grown from Mg-rich Fluxes*, June 2009, North American Solid State Chemistry Conference, Ohio State University, Columbus, OH

Other Accomplishments/Interests

- Full state college scholarship Spring 2001
- Hoffman graduate award Summer 2005
- MVP captain of varsity HS swimming team 1997-2001
- Life Scout in Boy Scouts of America 1996
- Recreational and competitive fishing
- Home renovation and restoration
- Motorcycling

Funding and Collaborators

Global Outreach Education for Science and Engineering Technology (GEOSET) www.geoset.info

Dr. Brent Greska, et. al.

Dr. Christopher Wiebe, et. al.

Dr. Stan Tozer, et. al.